Erasmus MC
Universitair Medisch Centrum Rotterdam

ICIN

Thoraxcentre

The Tenth European Symposium on Ultrasound Contrast Imaging

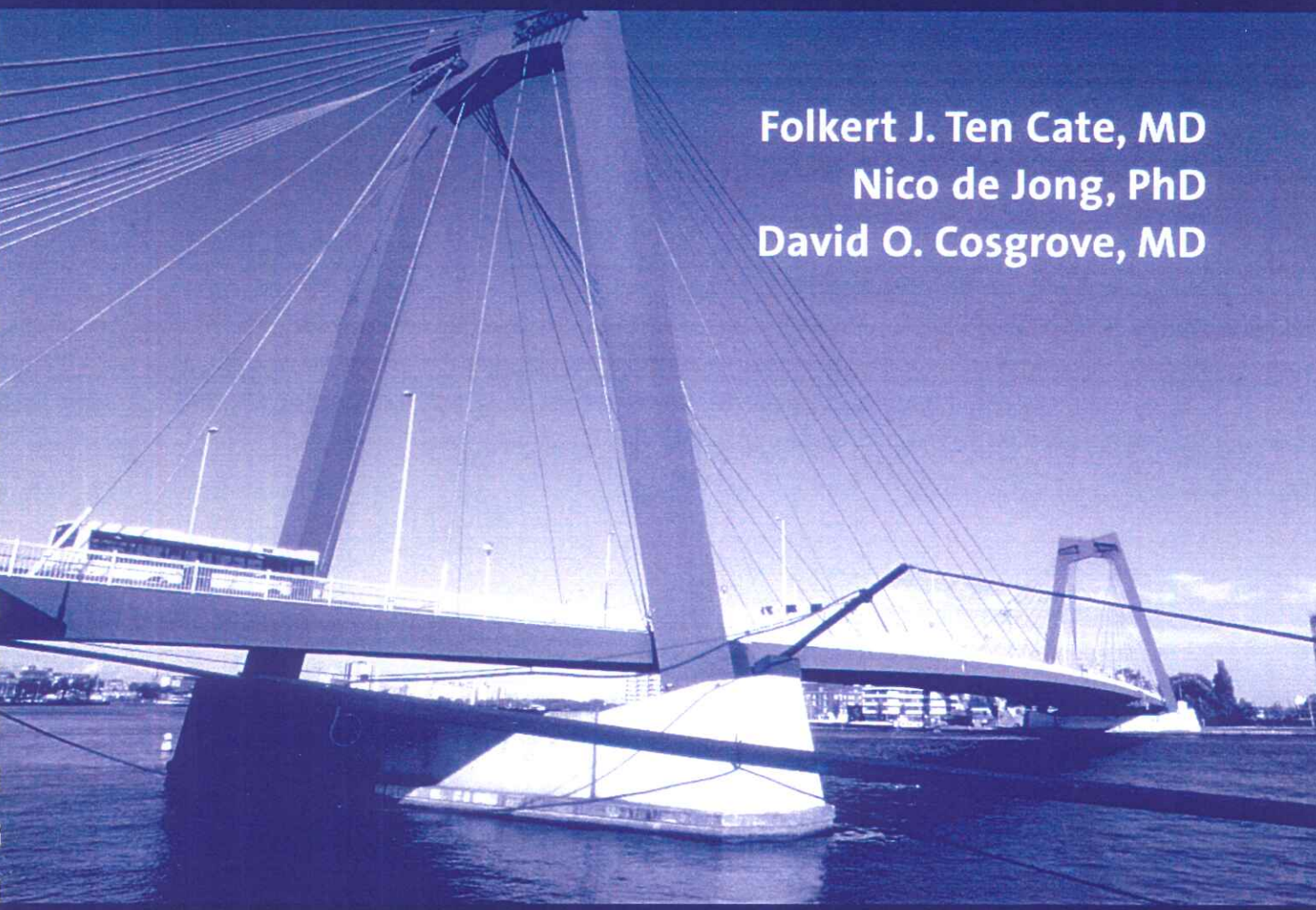

Folkert J. Ten Cate, MD
Nico de Jong, PhD
David O. Cosgrove, MD

Abstract book

January 20-21, 2005, Rotterdam, The Netherlands

10th EUROPEAN SYMPOSIUM ON ULTRASOUND CONTRAST IMAGING
20-21 JANUARY 2005, Rotterdam, The Netherlands

WEDNESDAY, 19 January 2005

18.00 - 20.00 **Registration - Welcome Drinks - Posters** ..... **Hilton Hotel**

THURSDAY, 20 January 2005

08.00 - 09.00 **Registration**

09:00 - 09:05 **Opening address by Mr. Ivo Opstelten, Mayor of Rotterdam**

9.05 - 10.35 **PAST, PRESENT, FUTURE** ..... *Chairpersons: Martin Blomley and Otto Kamp*

Mark Monaghan — What have we learnt from 10 years Rotterdam symposium: Clinical aspects

Peter Burns — What have we learnt from 10 years Rotterdam symposium: Technical aspects

Folkert ten Cate — Contrast Agents: Past, present and future

10.35 - 11.00 **Intermission**

11.00 - 12.30 **TECHNOLOGY I: Sonovue Models** *Chairpersons: Nico de Jong and Michel Versluis*

Michiel Postema — A coalescence model for SonoVue 1

Tom Matula — SonoVue Contrast Agent response using light scattering 8

Nikos Pelekasis — Modelling of SonoVue™ Microbubbles in an Ultrasound Field 15

Philippe Marmottant — A model for large amplitude oscillations of coated bubbles accounting for buckling and rupture 23

12.30 – 14.00 **LUNCH**

Announcement of the winner of the contest sponsored by BRACCO

14.00 - 15.30 **FUNCTIONAL IMAGING 1**.....*Chairpersons: Fuminori Moriyasu and Mike Averkiou*

Wilko Wilkening — Ultrasound angiographic imaging 34

Jean-Michel Correas — Assessment of the renal blood flow in pigs using contrast-enhanced sonography 36

Linda Juffermans — Ultrasound Contrast Agents and the role for reactive oxygen species in sonoporation 37

K. Schlottmann — Detection and characterization of splenic lesions – a prospective study comparing contrast harmonic imaging with computed tomography or magnetic resonance imaging 38

Annemieke van Wamel — Microbubbles Poking and Prodding Living Cells 40

15.30 – 16.00 **Intermission**

16.00 – 17.30 **VASOVASORUM**..... *Chairpersons: David Cosgrove and Folkert ten Cate*

Steven Feinstein — Direct,real-time visualization of the vasavasorum and carotid plaque neo-vascularization in patients: Correlation between the contrast-enhanced images and histology 42

Alexander Klibanov — Gas-filled microbubble contrast agents: shell behavior in the compression and rarefaction pressure field 44

Grigorios Korosoglou — Ultrasound Exposure can Increase the Membrane Permeability of Human Neutrophil Granulocytes Containing Microbubbles without Causing Complete Cell Destruction 46

Rob Krams — Physiology of vasovasorum related to atherosclerosis 48

Barbara Biedermann — Arterial Neovascularization and Inflammation in Patients with Symptomatic Atherosclerosis 51

18.30 - 22.30 **SOCIAL EVENT (Incl. Dinner buffet)** 100

FRIDAY, 21 January 2005

Announcement of the winner of the poster-price sponsored by the Dutch Foundation for Ultrasound Society in Medicine &Biology (SUGB) by Ton van der Steen

A coalescence model for SonoVue™

Michiel Postema*, Sascha Hilgenfeldt†, Charles T. Lancée‡, Philippe Marmottant§, Annemieke van Wamel‡¶

* Institute for Medical Engineering, Ruhr-University Bochum, Bochum, Germany
† Engineering Sciences & Applied Mathematics and Dept. of Mechanical Engineering, Northwestern University, Evanston, IL, USA
‡ Department of Experimental Echocardiography, Thoraxcentre, Erasmus MC, Rotterdam, The Netherlands
§ Laboratoire de Spectrométrie Physique, CNRS – Université Joseph Fourier, Saint Martin d' Hères, France
¶ Interuniversity Cardiology Institute of the Netherlands, Utrecht, The Netherlands

I. Introduction

SonoVue™ is a second generation contrast agent, consisting of SF_6 gas microbubbles encapsulated by an elastic lipid shell. It is the only agent allowed for clinical use in Europe. Predicting the dynamic behavior of ultrasound insonified SonoVue™ microbubbles has been of much clinical interest. To improve detection methods and to develop therapeutic applications, the behavior of individual microbubbles has been observed and analyzed.

Because SonoVue™ has a mean diameter of 2 μm, its resonance frequency is above 3 MHz. Bubbles smaller than resonant size hardly generate an acoustic response, but insonifying at higher frequencies seriously affects the penetration depth of the ultrasound. The coalescence of microbubbles might be used to increase the acoustic response from bulk agent at relatively low acoustic frequencies, without increasing the dosage. Since the strongest acoustic response is generated by bubbles above resonant size, a theoretically simple way to increase scattering from contrast agent would be to induce bubble coalescence until the bubbles reach resonant sizes.

In this paper, a method is presented to model coalescence behavior of SonoVue™ microbubbles. The *in vitro* experiments have been performed on a similar agent.

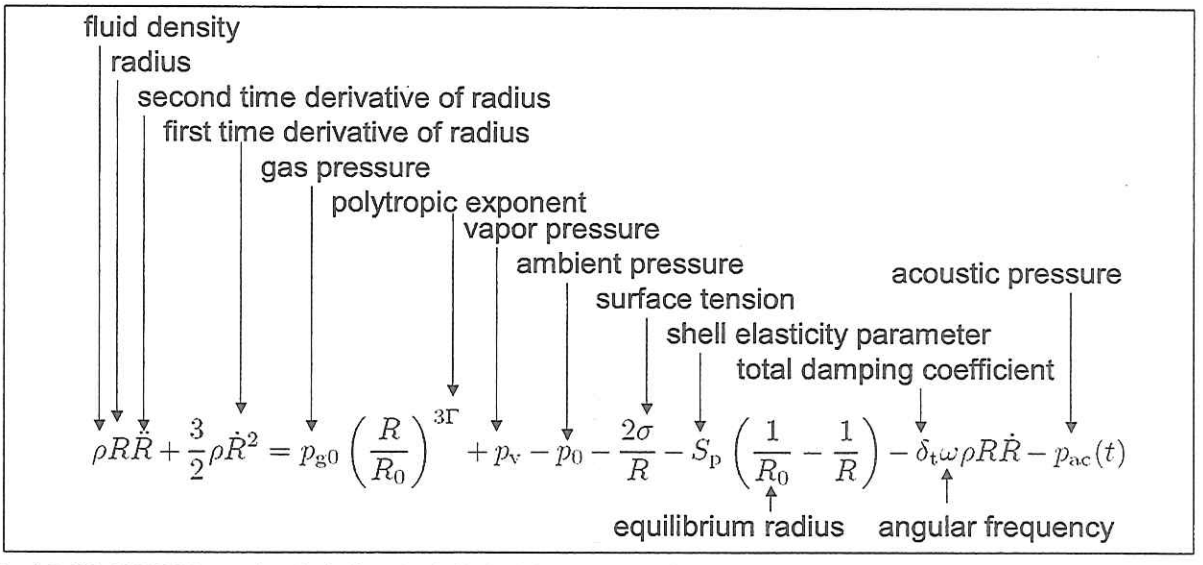

Fig. 1. Modified RPNNP equation, including the shell elasticity parameter S_p.

II. Oscillating lipid-encapsulated bubbles

Most models have been based on those for oscillating free gas bubbles. An overview of oscillating free gas bubble models was published by Vokurka [1]. Although the well-known RPNNP equation properly describes the oscillations of an individual microbubble in an ultrasonic field, it does not account for the presence of an encapsulation. De Jong introduced shell parameters to account for the presence of the shell [2], [3]. The resulting modified RPNNP equation is demonstrated in Figure 1. The effect of the internal

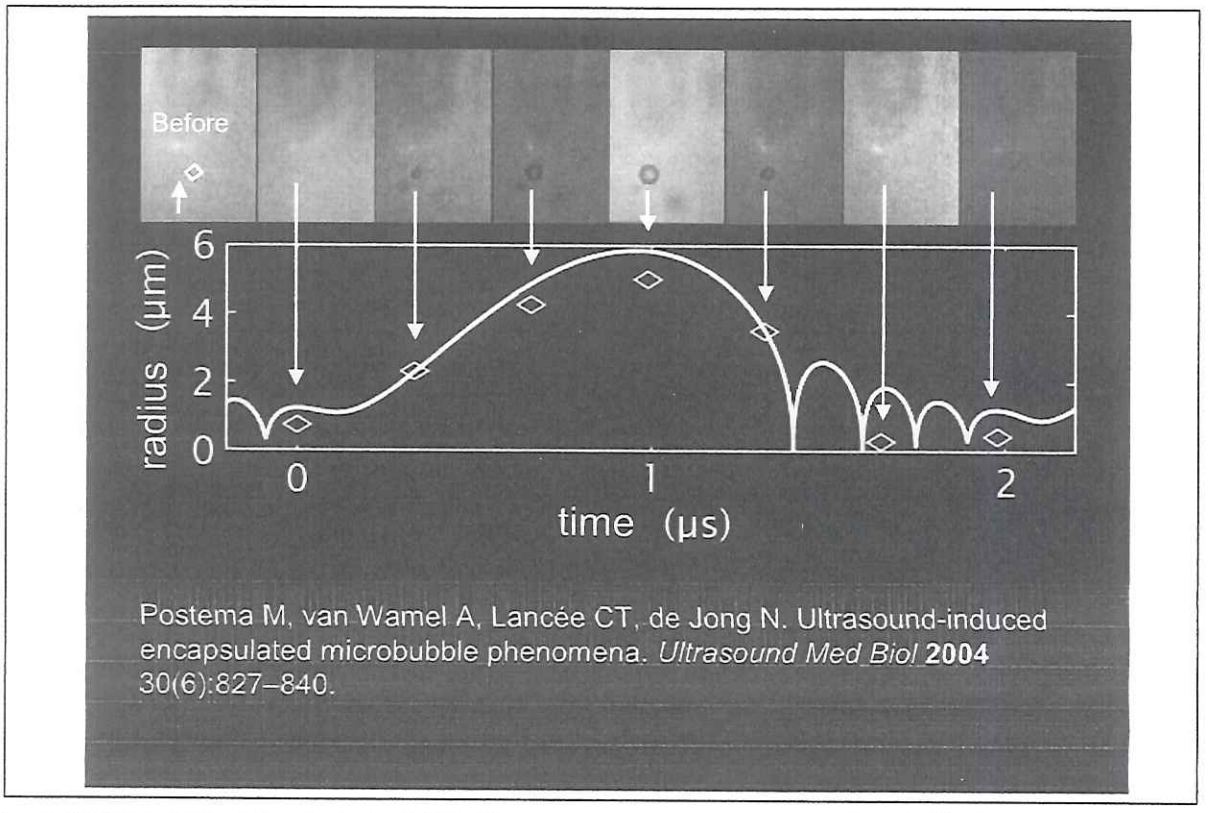

Fig. 2. Oscillating experimental contrast microbubble. The image sequence spans one ultrasonic cycle. The first frame has been captured prior to ultrasound arrival. Inter-frame times for the other frames are 0.33 μs. Each frame corresponds to a $88 \times 58\,\mu\text{m}^2$ area. Above: a $\varnothing$ 1.5 μm bubble strongly oscillates (MI= 0.67). Below: radius–period plot of the event. The solid line represents an oscillating free gas bubble.

friction inside the shell is included in the total damping coefficient [2], [4], [5]:

$$\delta_{\text{t}} = \delta_{\text{rad}} + \delta_{\text{vis}} + \delta_{\text{th}} + \frac{S_{\text{f}}}{m\omega}, \tag{1}$$

where δ_{rad} is the damping coefficient due to reradiation, δ_{vis} is the viscous damping coefficient, δ_{th} is the thermal damping coefficient, S_{f} is the shell friction parameter, and m is the effective mass of the bubble–liquid system. Gorce *et al.* computed the shell elasticity parameter S_{p} and the shell friction parameter S_{f} for SonoVue™, based on acoustic measurements on bulk agent [6]. They found $S_{\text{p}} = 1.1\ \text{N m}^{-1}$ and $S_{\text{f}} = 0.27 \times 10^{-6}\ \text{kg s}^{-1}$, using acoustic pressures in the clinical diagnostic range. Postema *et al.* investigated phospholipid-encapsulated gas bubbles, kindly supplied by Bracco Reasearch SA, Geneva, Switzerland, that are very similar to SonoVue™ [7]. Instead of SF_6, however, the bubbles contain the heavier C_3F_8. Individual contrast agent microbubles were subjected to high-speed photography during insonification, and relative excursions were then compared to computations from De Jong's model and a modified Herring equation published by Morgan *et al.* [8], substituting the shell parameters from Gorce *et al.* It was found that at high acoustic pressures (MI> 0.6), De Jong's model gives conservative estimates for the maximal excursion, whereas Morgan's model predicts maximal excursions that are too high.

At high acoustic pressures, high-speed photographs show that the lipid-encapsulated bubbles may expand to more than ten-fold their initial surface areas during one ultrasonic cycle [9]. The shell consists of a lipid monolayer that, under the conditions of the experiments, is in a solid state. It behaves like an elastic membrane that ruptures under relatively small strain [10]. By the time of maximal expansion, therefore, the shell has ruptured, leaving newly formed clean free interfaces. As such, the elastic properties of the shell will have diminished, resulting in a maximal expansion similar to a free gas bubble. Figure 2 shows an example of an optical sequence of an insonified Bracco agent microbubble, captured during one high-MI ultrasonic cycle. Clearly, the simulated curve ($S_\mathrm{p} = 0\ \mathrm{N\,m^{-1}}$, $S_\mathrm{f} = 0\ \mathrm{kg\,s^{-1}}$) and the measured radii match [11].

For MI< 0.1, Gorce's shell parameters are presumed valid, whereas for MI> 0.6, shell parameters should be neglected. The validity of shell parameters in the regime 0.1 <MI< 0.6 has been under investigation.

III. Lipid-encapsulated bubbles translating towards each other

In order to coalesce, bubbles have to translate towards each other. The mean approach velocity v_a of two approximately identical bubbles is given by [12], [11]:

$$v_\mathrm{a} = -\frac{(2\pi f p_\mathrm{ac}^-)^2}{27\eta}\,\rho\kappa^2\,\frac{R_0^5}{d_0^2}\,, \tag{2}$$

where f is the insonifying frequency, p_ac^- is the peak rarefactional acoustic pressure, η is the viscosity of the liquid, d_0 is the distance between the centers of the two bubbles, and κ is the compressibility of the bubble

$$\kappa = \frac{1}{\rho}\frac{\partial \rho}{\partial p}\,. \tag{3}$$

Figure 3 shows 5 image frames of two $\oslash\ 4\,\mu$m Bracco constrast microbubbles, each captured after

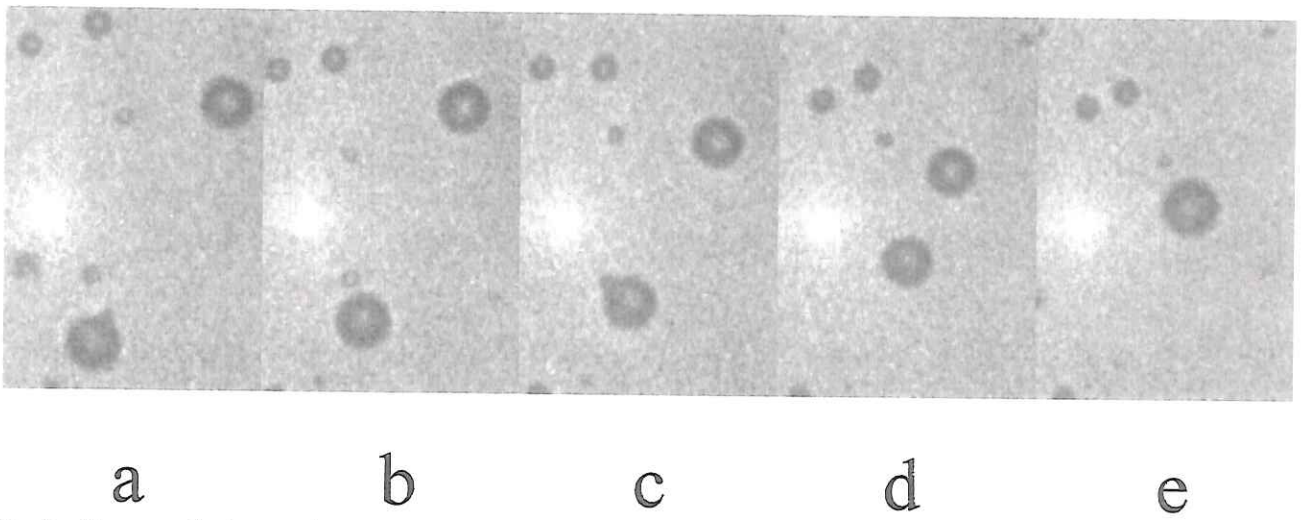

Fig. 3. The approach of two $\oslash\ 4\,\mu$m experimental contrast bubbles induced by a secondary radiation force. Each image frame corresponds to a $30 \times 20\,\mu\mathrm{m}^2$ area. Frames are each captured after insonification by 10 cycles of 0.5 MHz ultrasound (MI= 0.67).

insonification by 10 cycles of 0.5 MHz ultrasound (duration $t_\mathrm{p} = 20\,\mu$s). Each image frame corresponds to a $30\times20\ \mu\mathrm{m}^2$ area. During every ultrasound burst the bubbles draw nearer to each other. For each center-to-center distance d_0 measured the mean approach velocity v_a has been computed from equation (2), taking $\kappa = 5\times10^{-6}\ \mathrm{m^2\,N^{-1}}$ (estimated from [2] and [12]). By combining d_0 with v_a, the theoretical distances $\Delta d_\mathrm{th} = v_\mathrm{a} t_\mathrm{p}$ have been computed. These were compared to the distance Δd_m measured from Figure 3.

TABLE I

TRAVELED DISTANCES AND MEAN VELOCITIES OF APPROACHING BUBBLES.

frame	d_0 (μm)	v_a (cm s^{-1})	Δd_{th} (μm)	Δd_m (μm)
a	21.2	15	3.0	3.2
b	18.0	20	4.0	3.9
c	14.1	33	6.6	6.4
d	7.7	111	> 7.7	7.7
e	0			

The results are summarized in Table I. The measured values Δd are consistent with theory. While the bubbles approach each other, their maximal sizes determine when they come into contact.

IV. FLATTENING OF THE INTERFACES AND LIPID-ENCAPSULATED MICROBUBBLE COALESCENCE

When two lipid-encapsulated gas bubbles are driven into each other, coalescence into a single bubble may result. The following stages of bubble coalescence have been identified (*cf.* Figure 4): flattening of the opposing bubble surfaces prior to contact, drainage of the interposed liquid film toward a critical minimal thickness, rupture of the liquid film, and formation of a single bubble. If the critical thickness is not reached during collision, the bubbles bounce off each other instead. Free gas bubble coalescence

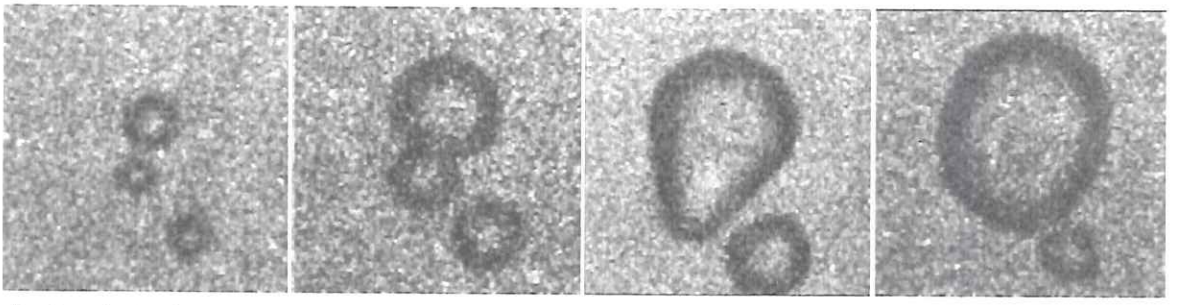

Fig. 4. Coalescing Bracco microbubbles during expansion. Interframe times are 0.33 μs. Each frame corresponds to a $21 \times 21 \mu m^2$ area.

after collision has been studied extensively [13], [14], [15], [16], [17], [18]. With ultrasound contrast agents, microbubble coalescence has been observed during ultrasound insonification, when expanding microbubbles come into contact with each other [19], [9], [20]. With the aid of high-speed photography, the coalescence times of insonified Bracco microbubbles were investigated. Observed coalescence times were compared to calculated film drainage times, based on the Reynolds equation [21] for no-slip interfaces and on the drainage equation for free interfaces. It was concluded that the bubbles behaved as if they had free interfaces like free gas bubbles [9]. However, to support this conclusion, the drainage equations were also validated for expanding free gas microbubbles. Rigid-shelled contrast agent microbubbles were exposed to high-intensity ultrasound, in order to release gas, and measure the coalescence times of these free gas bubbles [22].

The Weber number for a fluid containing two bubbles with radii R_1 and R_2, respectively, is given by the inertial force relative to the surface tension force:

$$\mathrm{We} = \rho u^2 \Big/ \frac{\sigma}{R_m} \ , \tag{4}$$

where u is the relative approach velocity, ρ is the fluid density, σ is the surface tension, and R_m is the mean bubble radius for which holds:

$$\frac{2}{R_m} = \frac{1}{R_1} + \frac{1}{R_2}. \tag{5}$$

We propose to extend this criterium to approaching walls of expanding bubbles. Because the radius and with it the approach velocity of oscillating bubbles change during a cycle, so does the Weber number. The approach velocity for expanding bubbles with a constant center-to-center distance is

$$u = \dot{R}_1 + \dot{R}_2 . \tag{6}$$

If the Weber number is low ($We \lessapprox 0.5$), bubble coalescence will always occur, without flattening of the adjacent surfaces prior to contact [17]. In the high Weber number regimen ($We \gtrapprox 1$), coalescence is determined by a second step, after flattening: drainage of the interposed liquid film. When the expansion time is less than the time needed for film drainage, the bubbles will bounce off each other [23].

The radial velocity of the liquid in the film is a combination of a plug flow driven by the motion of the interfaces, and a laminar velocity profile (analogous to Poiseuille flow) driven by the radial pressure gradient [24], [25]. If the bubble surfaces consist of a high concentration of surfactant, on our working scales the interfaces are to be considered immobile (no-slip) [26]. In the case of no-slip interfaces, the interfacial tangential velocity is zero, so the plug flow contribution is zero [24]. In the case of free interfaces, the Poiseuille contribution to the drainage flow becomes negligible [26], [24]. The film drainage time for free radial surfaces is approximated by the equation [27], [28]:

$$\tau_d \approx R_f \sqrt{\frac{\rho}{8p}} \log\left(\frac{h_i}{h_c}\right), \tag{7}$$

where R_f is the film radius, h_i is the initial thickness, h_c is the critical film thickness, at which the film ruptures, and p is the pressure difference between film and surrounding fluid which is taken

$$p = \sigma\left(\frac{1}{R_1} + \frac{1}{R_2}\right). \tag{8}$$

In our computations, we take

$$\begin{aligned} \rho &= 998\ \mathrm{kg\ m^{-3}}, \\ \sigma &= 0.072\ \mathrm{N\ m^{-1}},\ \text{and} \\ h_c &= 10\ \mathrm{nm}. \end{aligned} \tag{9}$$

Flattening takes place when:

$$\dot{R}_1 + \dot{R}_2 \gg \frac{\mathrm{d}h}{\mathrm{d}t}, \tag{10}$$

whereas the flat film drainage happens in the next stage, when

$$\dot{R}_1 \approx \dot{R}_2 \approx 0. \tag{11}$$

Thus, during drainage, on our timescales, we may consider p and R_f constant over time [9].

Calculated drainage times from an inertial drainage model assuming clean, stress-free interfaces are consistent with the observations: For large (fully expanded) bubbles the drainage times are too large (larger than a bubble oscillation cycle) to allow for film drainage and coalescence (*cf.* Figure 5). Smaller microbubble fragments, however, easily coalesce on very short timescales [9], [22].

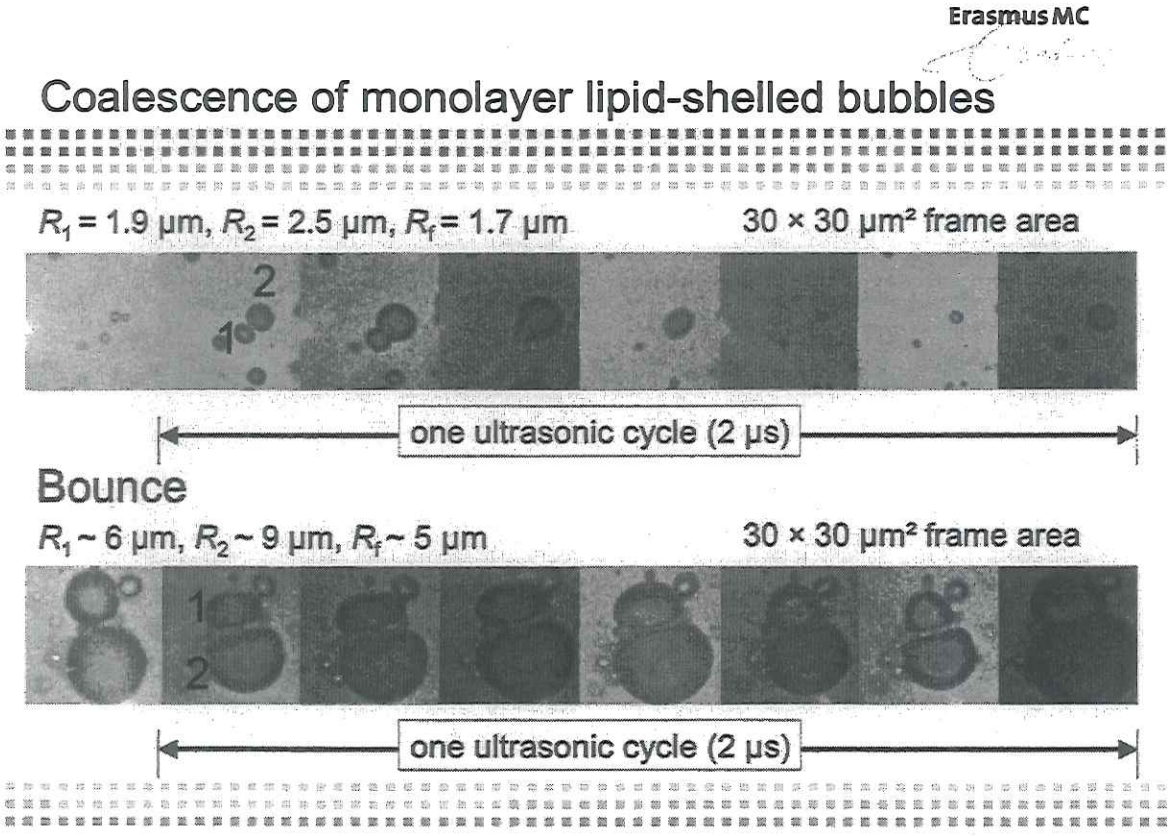

Fig. 5. Coalescing and bouncing Bracco microbubbles during expansion. Interframe times are 0.33 μs. Each frame corresponds to a $30 \times 30 \mu m^2$ area.

V. Conclusions

It takes tens of ultrasonic cycles to drive bubbles into each other, but it takes only one cycle to have them coalesce, if they are small enough. Despite the high approach velocity for large bubbles, drainage times are so high, that coalescence cannot occur. The total time of coalescence is approximated by the approach time added to the drainage time. If the Weber number is lower than 0.5, the drainage time itself is zero.

Ultrasound-induced coalescence of lipid-encapsulated Bracco contrast agent microbubbles is feasible. The coalescence of microbubbles might be used to increase the acoustic response from bulk agent at relatively low acoustic frequencies, without increasing the dosage. A theoretically simple way to increase scattering from contrast agent would be to induce bubble coalescence until the bubbles reach resonant sizes.

References

[1] K. Vokurka, "Comparison of Rayleigh's, Herring's, and Gilmore's models of gas bubbles," *Acustica*, vol. 59, pp. 214–219, 1986.
[2] N. de Jong, *Acoustic properties of ultrasound contrast agents*. Rotterdam: N de Jong, 1993.
[3] N. de Jong, R. Cornet, and C. T. Lancée, "Higher harmonics of vibrating gas-filled microspheres. Part one: simulations," *Ultrasonics*, vol. 32, no. 6, pp. 447–453, 1994.
[4] L. Hoff, "Acoustic properties of ultrasonic contrast agents," *Ultrasonics*, vol. 34, pp. 591–593, 1996.
[5] P. J. A. Frinking, *Ultrasound Contrast Agents: acoustic characterization and diagnostic imaging*. Rotterdam: PJA Frinking, 1999.
[6] J. M. Gorce, M. Arditi, and M. Schneider, "Influence of bubble size distribution on the echogenicity of ultrasound contrast agents: A study of SonoVue™," *Invest. Radiol.*, vol. 35, no. 11, pp. 661–671, 2000.
[7] M. Postema, A. Bouakaz, C. T. Chin, and N. de Jong, "Simulations and measurements of optical images of insonified ultrasound contrast microbubbles," *IEEE Trans. Ultrason., Ferroelect., Freq. Contr.*, vol. 50, no. 5, pp. 523–536, 2003.

[8] K. E. Morgan, J. S. Allen, P. A. Dayton, J. E. Chomas, A. L. Klibanov, and K. W. Ferrara, "Experimental and theoretical evaluation of microbubble behavior: Effect of transmitted phase and bubble size," *IEEE Trans. Ultrason., Ferroelect., Freq. Contr.*, vol. 47, no. 6, pp. 1494–1509, 2000.

[9] M. Postema, P. Marmottant, C. T. Lancée, S. Hilgenfeldt, and N. de Jong, "Ultrasound-induced microbubble coalescence," *Ultrasound Med. Biol.*, vol. in press, 2004.

[10] Z. Zhou and B. Joós, "Mechanisms of membrane rupture: from cracks to pores," *Phys. Rev. B*, vol. 56, no. 6, pp. 2997–3009, 1997.

[11] M. Postema, A. van Wamel, C. T. Lancée, and N. de Jong, "Ultrasound-induced encapsulated microbubble phenomena," *Ultrasound Med. Biol.*, vol. 30, no. 6, pp. 827–840, 2004.

[12] P. A. Dayton, K. E. Morgan, A. L. Klibanov, G. Brandenburger, K. R. Nightingale, and K. W. Ferrara, "A preliminary evaluation of the effects of primary and secondary radiation forces on acoustic contrast agents," *IEEE Trans. Ultrason., Ferroelect., Freq. Contr.*, vol. 44, no. 6, pp. 1264–1277, 1997.

[13] G. Marrucci, "A theory of coalescence," *Chem. Eng. Sci.*, vol. 24, pp. 975–985, 1969.

[14] D. S. Dimitrov and I. B. Ivanov, "Hydrodynamics of thin liquid films. On the rate of thinning of microscopic films with deformable interfaces," *J. Colloid. Interf. Sci.*, vol. 64, no. 1, pp. 97–106, 1978.

[15] I. B. Ivanov, D. S. Dimitrov, and B. P. Radoyev, "Generalized equations of thin films hydrodynamics and their application to the calculations of the thinning rate of films with non-deformed surfaces," *Kolloid. Zh.*, vol. 41, no. 1, pp. 36–42, 1979.

[16] C. Y. Lin and J. C. Slattery, "Thinning of a liquid film as a small drop or bubble approaches a fluid-fluid interface," *AIChE J.*, vol. 28, no. 5, pp. 786–792, 1982.

[17] A. K. Chesters and G. Hofman, "Bubble coalescence in pure liquids," *Appl. Sci. Res.*, vol. 38, pp. 353–361, 1982.

[18] P. C. Duineveld, *Bouncing and coalescence of two bubbles in water*. Enschede: PC Duineveld, 1994.

[19] M. Postema, A. Bouakaz, C. T. Chin, and N. de Jong, "Optically observed microbubble coalescence and collapse," *Proc. IEEE Ultrason. Symp.*, pp. 1900–1903, 2002.

[20] M. A. B. Postema, *Medical Bubbles*. Bergschenhoek: Michiel Postema, 2004.

[21] O. Reynolds, "On the theory of lubrication and its application to Mr. Beauchamp Tower's experiments, including an experimental determination of the viscosity of olive oil," *Philos. Trans. Roy. Soc. A*, vol. 177, pp. 157–234, 1886.

[22] M. Postema, P. Marmottant, C. T. Lancée, M. Versluis, S. Hilgenfeldt, and N. de Jong, "Ultrasound-induced coalescence of free gas microbubbles," *Proc. IEEE Ultrason. Symp.*, vol. in press, 2004.

[23] R. V. Chaudhari and H. Hofmann, "Coalescence of gas bubbles in liquids," *Rev. Chem. Eng.*, vol. 10, no. 2, pp. 131–190, 1994.

[24] E. Klaseboer, J. P. Chevaillier, C. Gourdon, and O. Masbernat, "Film drainage between colliding drops at constant approach velocity: experiments and modeling," *J. Colloid. Interf. Sci.*, vol. 229, pp. 274–285, 2000.

[25] D. F. Young, B. R. Munson, and T. H. Okiishi, *A Brief Introduction to Fluid Mechanics*, 2nd ed. New York: John Wiley & Sons, 2000.

[26] L. van Wijngaarden, "The mean rise velocity of pairwise-interacting bubbles in liquid," *J. Fluid Mech.*, vol. 251, pp. 55–78, 1993.

[27] R. D. Kirkpatrick and M. J. Lockett, "The influence of approach velocity on bubble coalescence," *Chem. Eng. Sci.*, vol. 29, pp. 2363–2373, 1974.

[28] L. Hagesæther, *Coalescence and break-up of drops and bubbles*. Trondheim: Norwegian University of Science and Technology, 2002.

SonoVue® Contrast Agent response using light scattering

Jingfeng Guan and Thomas J. Matula

Applied Physics Lab, University of Washington
1013 NE 40th Street, Seattle, WA 98115 USA
email: jfguan@apl.washington.edu; matula@apl.washington.edu

ABSTRACT

Light scattering is used to measure the dynamic oscillation of individual SonoVue® microbubbles. Highly diluted SonoVue® microbubbles were injected into either a water tank or a diluted gel made of xanthan gum and water. Individual SonoVue® microbubbles' responses to driven pulses were measured. SonoVue® microbubbles generate strong nonlinear responses. **There will be two major conclusions to this work; first, we tested several bubble dynamics models, and they all seem to give similar results. Thus, it is important to find a parameter space in which one can distinguish between the models. Second, the models do not predict the response of Sonovue® bubbles very well.**

INTRODUCTION

It is still a challenge to describe the physical interaction of ultrasonic pulses with ultrasound contrast agents (UCAs). The interaction is usually studied by traditional methods, such as acoustic scattering, attenuation, noise emission, and even optical microscopy. We have developed a light scattering technique that not only gives real-time information about the dynamical response of UCAs, but also can be used to monitor the pulse-to-pulse evolution of microbubbles. In this paper, we apply the technique to SonoVue® bubbles.

LIGHT SCATTERING: Light scattering has been used to monitor air bubbles[1, 2] and unshelled bubble oscillations in real time[3-5]. Recently, we proposed using light scattering method to measure the oscillation of individual and multiple UCA bubbles (Optison® and Sonazoid®)[6]. Compared with other measuring methods, light scattering signals can be collected for long times with high resolution in real time, allowing us to monitor the development of UCAs with successive acoustic pulses. Based on Mie scattering theory, the modifications of Mie scattering for a coated sphere (such as contrast agents) were developed by Aden and Kerker[8] and applied to coated bubbles by Marston[9, 10]. Our implementation of the model for a coated sphere is based on the equations in the book by Bohren and Huffman[7]. Fig. 1a illustrates the scattering light intensity as a function of scattering angle for gas bubbles (solid line) and coated UCA bubbles (dashed line) with 15nm thickness of coating (refractive index is 1.5).

In our experimental setup, we use 80° scattering angle with a collecting lens, covering approximately 70° to 90°. Fig. 1b shows the relative integrated intensity over this range of angles. Notice that there is little deviation from the uncoated bubble for a coating thickness of less than about 30 nm. Therefore, for thin-coated bubbles, we can neglect the

coating and simplify the calculations. We thus don't have to worry about aspects such as shell thinning because these effects won't be observed. Also, notice that there is a monotonic relationship between bubble size and scattered light intensity. Because of this relationship, we can invert the scattered light intensity into a radius for modeling and analysis.

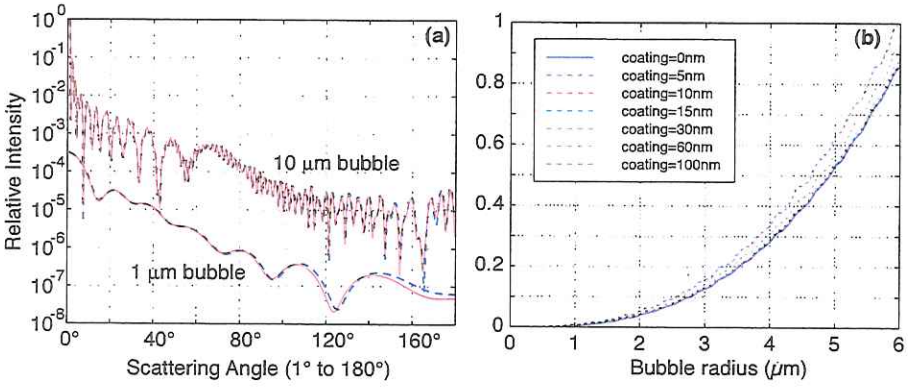

Figure 1: *(a) Light scattered intensities for a gas bubble and a coated gas bubble (15 nm thickness) show similar properties as a function of scattering angle. (b) Scattering intensity maintains monotonic function of bubble size, and there is little difference between a gas bubble and coated gas bubble when the coating thickness is less than about 30 nm.*

BUBBLE DYNAMICS MODELING: Because of the shell, modeling the response of UCAs to pulsed ultrasound is non-trivial. **There are several bubble dynamics models that describe UCA oscillations; however, we have found that all seem to give about the same results.** Figure 2 illustrates the response of a 3 μm diameter bubble subject to a 1-MHz pulse with a peak negative pressure of 0.4 MPa. The models used include the Morgan model, the Hoff model, and the Church model. The parameters used are given in Table I.

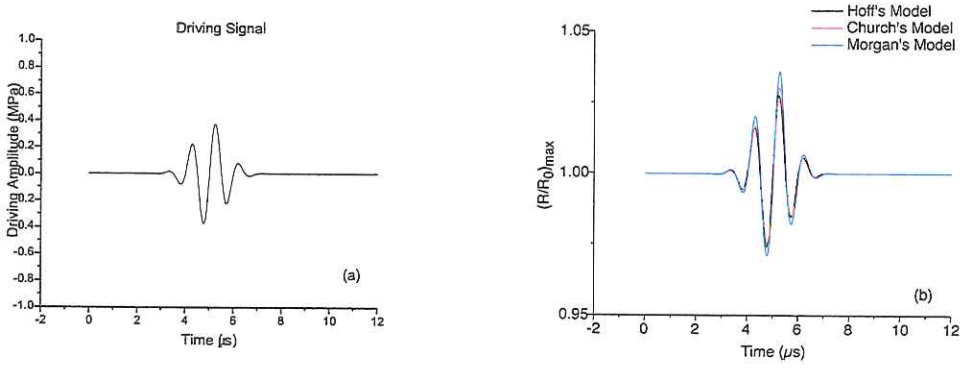

Figure 2. *(a) A modified Gaussian pulse is used to stimulate the driving signal:* $P_{div} = P_0 \sin[2\pi f(t-t_c)]\exp[-\pi^2 h^2 f^2 (t-t_c)^2]$, *where* t_c*= 5 μs and h=1/3. (b) Typical bubble response using three different bubble dynamics formulations.*

Table I. *The values of physical parameters required for the simulation of a UCA bubble:*

$\rho_L = 10^3$ *kg/m, is the density of the liquid.*
$P_0 = 101300$ *Pa, is the ambient pressure.*
$P_v = 2330$ *Pa, is the vapor pressure.*
$\sigma = 0.07275$ *N/m, is the surface tension.*
$\rho_g = 1.161$ *kg/m^3, is the gas density.*
$C_p = 240.67$, *is the heat capacity at constant pressure, (from CRC handbook).*
$K_g = 0.00626$, *is the thermal conductivity, (from CRC handbook, for air at 300K and 1 atm).*
$c = 1500$ *m/s, is the acoustic velocity.*
$\gamma = 1$, *is the gas adiabatic constant, (the value of* γ *doesn't make a big difference, so we used* $\gamma = 1$ *for all the calculations).*
$\eta_L = 0.001$ *Pa·s, is the liquid shear viscosity.*
$\rho_s = 1100$ *Kg/m^3 is the shell density.*
$\sigma_1 = 0.04$ *N/m, is the surface tension of the gas-shell interface*[13].
$\sigma_2 = 0.005$ *N/m, is the surface tension of the shell-liquid interface*[13].
$Gs = 114$ *MPa, is the shell shear modulus*[15].
$d_{se} = 15$ *nm, is the shell thickness*[15].
$\eta_s = 2.1$ *Pa·s, is the shell shear viscosity*[15].
$\chi = 40$ *N/m, is the elasticity modulus of lipid shell*[14].

SonoVue® contrast agents are lipid-shelled bubbles with core gas SF_6. Lipid shell is a mono layer membrane, which is very thin if compared with the albumin coating of Optison® UCAs. Because of this thin coating and it's lack of significance with respect to light scattering, we prefer a 'thin shell' model to incorporate the thickness with other parameter(s) and treat the thickness of coating infinitesimal; we thus choose to follow the implementation of Sarkar, *et al.* [16]

$$\rho R\ddot{R} + \frac{3}{2}\rho\dot{R}^2 = \left(P_0 + \frac{2\sigma}{R}\right)\left(\frac{R_0}{R}\right)^{3\gamma} - \frac{4\mu\dot{R}}{R} - \frac{2\sigma}{R} - \frac{4\kappa_s\dot{R}}{R^2} - \left(P_0 + P_{drive}(t)\right) \qquad (1)$$

where R is radius of the bubble, R_0 is initial radius of the bubble, P_0=1.01x10^5 Pa is the ambient pressure, $P_{drive}(t)$ is the acoustic driving pulse (which is measured by the hydrophone), ρ=1000 kg/m^3 is the liquid (water) density, $\gamma \approx 1$ is the ratio of specific heats[17], σ=0.051 N/m^2 is surface tension coefficient (gas-shell and shell-water interfaces), μ=0.001 Pa·s is fluid shear viscosity, and κ_s is the UCA shell dilatational viscosity (in units of Pa·m·s). Because the bubble's dynamics is not very sensitive to surface tension coefficient σ during our simulation, compared with dilatational viscosity κ_s, we choose the value of surface tension coefficient 0.051 N/m^2 based on our previous experience.

In general, there are two unknown parameters: the initial radius R_0 and dilatational viscosity κ_s (ultrasonic driving pulse is known from measurements). These two parameters will be fitted to the light scattering data to obtain a best fit for the model. We emphasize that the model itself is not the important issue; several models have been

tested and they all give similar results. Therefore we are unable to say with certainty that one model is 'better' than another model. The major point will be that although the different models work well with agents such as Optison® and Sonozoid®, we will show that they do not work well with SonoVue® bubbles. **A major conclusion to this work is that a better model needs to be developed in order to satisfactorily account for a SonoVue® response.**

EXPERIMENTAL SETUP

We injected highly diluted SonoVue® agents into the region of interest (a small volume where the ultrasound and laser beams intersect with microbubbles) with a syringe pump at a rate of 10ml/hr with a 0.5 mm inner-diameter tube. The driving source was an ultrasonic pulse from a probe of a diagnostic ultrasound instrument (Ultramark 4Plus from ATL) operated in M-mode at about 1 kHz pulse-repetition-frequency (PRF). An NTR calibrated needle hydrophone monitored the acoustic pressure. We used a 30 mW HeNe laser as a light source. The laser beam waist was focused to less than 100 μm at the region of interest by a lens. The light scattered off the bubble in the region of interest was then collected by another lens and focused onto a photo-multiplier tube (PMT) detector (Hamamatsu, model 2027). The outputs of the PMT and the hydrophone were recorded directly by a high-speed digital oscilloscope, and then transferred to a computer for post-processing. Data collection was conducted in sequence mode, where high-resolution data files can be collected each and every pulse.

RESULTS AND DISCUSSION

The response of an individual SonoVue® UCA bubble is illustrated in Fig. 3a and the corresponding spectral analysis is illustrated in Fig 3b. We were able to obtain a relatively good fit using R_0= 1.4 μm (radius). The negative peak pressure is about 0.16 MPa. In Fig. 3a, the solid line is experimental data while the dashed line is the modeling curve based on the bubble dynamics equation. The coating parameter of the bubble, κ_s dilatational viscosity, is 7.0 nm·s·Pa. In Fig. 3b, the corresponding power spectrum also shows that even though the fundamental harmonic signal (at f_1) is strongest, second harmonic signal (at f_2) is also very significant, only about 10 dB below that of fundamental signal. The sub-harmonic signal (at $f_{1/2}$) is even more significant, about 7 dB below that of fundamental signal. The fundamental is due to the driving waveform, because the bubble is not oscillating freely.

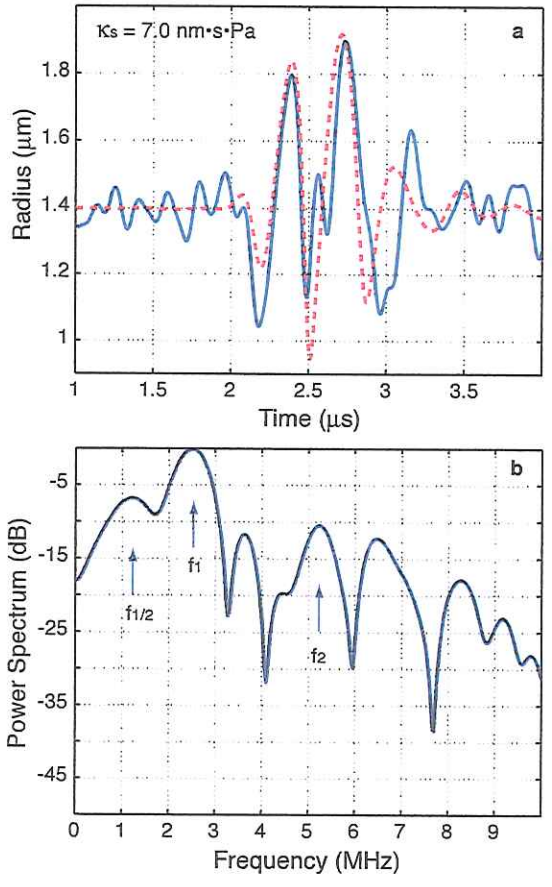

Figure 3: *(a) A SonoVue® UCA bubble oscillates with a driving pulse. The solid line is experimental data and the dashed line is the modeling result. This bubble is modeled with 1.4 μm radius and 7.0 nm·s·Pa dilatational viscosity of UCA shell; (b) the power spectrum of the bubble response reveals the fundamental harmonic signal at f_1, second harmonic signal at f_2 and sub-harmonic signal at $f_{1/2}$.*

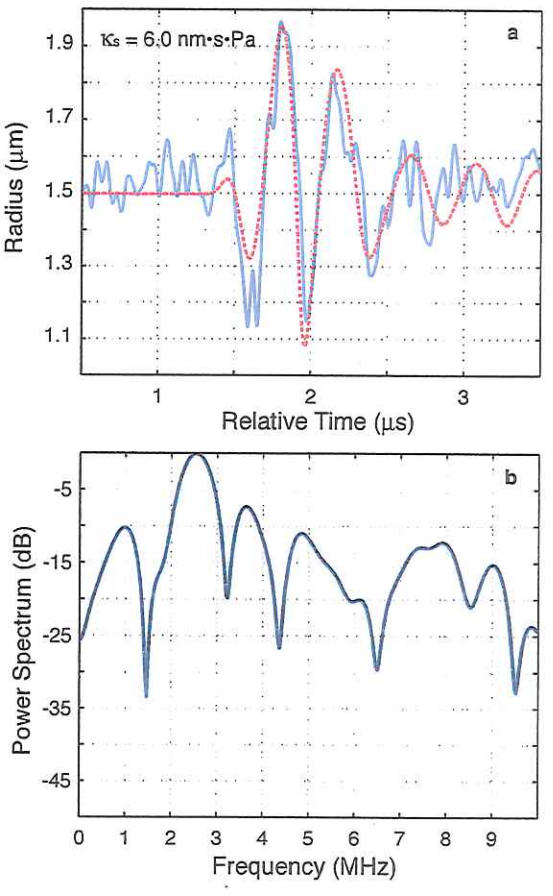

Figure 4: *A corresponding Sonazoid® bubble with a driving pressure of about 0.13 MPa. (a) The solid line is experimental data and the dashed line is the modeling result. This bubble is modeled with 1.47 μm radius and 6.0 nm·s·Pa dilatational viscosity of UCA shell; (b) the corresponding power spectrum of the bubble response is illustrated.*

We show in Fig. 4 a corresponding Sonazoid® response, with a driving pressure amplitude of about 0.13 MPa. Sonazoid® UCA bubbles have lipid coating as well. These two types of UCAs would be expected to have similar responses. In Fig. 4, the bubble can be fit with 6 nm·s·Pa dilatational viscosity, which is close to the SonoVue® UCA bubble fit. However, SonoVue® and Sonazoid® UCA bubbles' responses to the identical driving pulse are different. The SonoVue® UCA bubbles shows a stronger nonlinear response than that of the Sonazoid® UCA bubble. This fact could be observed in both time-series data and power spectrum analysis in Fig. 3 and Fig. 4. In addition, the Sonazoid bubble shows a better fit to the bubble dynamics model, especially towards the

end of the pulse. **We have been unable to obtain good fits to the SonoVue® bubble at the later stages of an acoustic pulse.** This suggests that the SonoVue® bubble has a different, and as yet unexplained, response than it's cousin Sonazoid®. We suspect that the shell changes during a pulse.

CONCLUSION

We have conducted a study with SonoVue® UCA bubbles with light scattering and modeling of these bubbles with a standard bubble dynamics equation. The findings suggest that (1) several bubble dynamics models can be be used, because they all seem to give similar results; (2) SonoVue® UCA bubbles can be described by bubble dynamics equations, but that their response changes during a short pulse, suggesting that the shell may change during this time. We also find that SonoVue® UCA bubbles generate strong nonlinear responses with both harmonic and sub-harmonic signals.

ACKNOWLEDGEMENT

We would like to thank Bracco for providing samples of SonoVue® UCA bubbles. Portions of this work are supported by 3DAMD17-02-2-0014 and NIH 8RO1EB00350-2.

REFERENCE

[1] D. L. Kingsbury and P. L. Marston, "Mie scattering near the critical angle of bubbles in water," J. Opt. Soc. Am. **71**, 358-361 (1981).

[2] G. M. Hansen, "Mie scattering as a technique for the sizing of air bubbles," Appl. Opt. **24**, 3214-3220 (1985).

[3] R. G. Holt and L. A. Crum, "Mie scattering used to determine spherical bubble oscillations," Appl. Opt. **29**, 4182-4191 (1990).

[4] B. P. Barber and S. J. Putterman, "Light scattering measurements of the repetitive supersonic implosion of a sonoluminescing bubble," Phys. Rev. Lett. A. **69**, 3839-3842 (1992).

[5] T. J. Matula, "Inertial cavitation and single bubble sonoluminescence," Phil. Trans. R. Soc. Lond. A **357**, 225-249 (1999).

[6] Jingfeng Guan and Thomas J. Matula, "Using light-scattering to measure the response of individual ultrasound contrast microbubbles subjected to pulsed ultrasound in vitro," JASA, Volume 116, Issue 5, pp. 2832-2842 (2004).

[7] C. F. Bohren and D. R. Huffman, *Absorption and scattering of light by small particles.* (J. Wiley and Sons, New York, 1998).

[8] A. L. Aden and M. Kerker, " Scattering of electromagnetic waves from two concentric spheres," J. Appl. Phys. **22**, 1242-1246 (1951).

[9] P. L. Marston, S. C. Billette and C. E. Dean, "Scattering of light by a coated bubble in water near the critical and Brewster scattering angles," Ocean Optics IX, **925**, 308-316 (1988).

[10] P. L. Marston, "Colors observed when sunlight is scattered by bubble clouds in sea water," Appl. Opt. **30**, 3479-3484+3549 (1991).

[11] N. de Jong, L. Hoff, T. Skotland and N. Bom, "Absorption and scatter of encapsulated gas filled microspheres: theoretical considerations and some measurements," Ultrasonics **30**, 95-103 (1992).

[12] N. de Jong and L. Hoff, "Ultrasound scattering properties of Albunex microspheres," Ultrasonics **31**, 175-181 (1993).
[13] C. C. Church, "The effects of an elastic solid surface layer on the radial pulsations of gas bubbles," J. Acoust. Soc. Am. **97**, 1510-1521 (1995).
[14] K. E. Morgan, J. S. Allen, P. A. Dayton, J. E. Chomas, A. L. Klibanov and K. W. Ferrara, "Experimental and theoretical evaluation of microbubble behavior: Effect of transmitted phase and bubble size," IEEE Trans. Ultrason., Ferroelect., Freq. Contr. **47**, 1494-1508 (2000).
[15] L. Hoff, P. C. Sontum and J. M. Hovem, "Oscillations of polymeric microbubbles: Effect of the encapsulating shell," J. Acoust. Soc. Am. **107**, 2272-2280 (2000).
[16] Dhiman Chatterjee And Kausik Sarkar, "A Newtonian Rheological Model For The Interface Of Microbubble Contrast Agents," Ultrasound in Med. & Biol., Vol. 29, No. 12, pp. 1749–1757, 2003
[17] C. L. Yaws, *Matheson Gas Data Book*, Seventh ed. (McGraw-Hill, 2001).

Modelling of SonoVue™ Microbubbles in an Ultrasound Field

K. Tsiglifis[1], N. A. Pelekasis[1,*] & V. Sboros[2]
[1]Dept. of Mechanical & Industrial Engineering, University of Thessaly, Volos, Greece
[2]Dept. of Medical Physics & Medical Engineering, University of Edinburgh, Edinburgh UK
[1,*]Author to whom correspondence should be addressed; Email: pel@uth.gr

ABSTRACT

The echo produced by encapsulated microbubbles that are injected in the bloodstream, in response to an ultrasound beam, can be used to assess vascularity and perfusion, among many other clinical applications. In this context, the backscatter signal due to spherosymmetric oscillations of a contrast agent microbubble, is predicted theoretically and numerically for a range of ultrasound frequencies and amplitudes. The effects of shell thickness, elasticity and viscosity as well as those of liquid viscosity and compressibility are accounted for. It is shown that nonlinearity can affect the dynamics of the microbubble by invoking higher harmonics thus modifying contrast agent efficacy. When shape oscillations are allowed interesting dynamic phenomena are revealed, as a result of initial bubble elongation, disturbance in the far field pressure or bubble-bubble interaction. Introduction of shell elasticity results in buckling and break-up of the shell during the compression phase of the oscillating micro-bubble, in response to pressure variations caused by the ultrasound beam. Prediction of the size of the emerging fragments requires evaluation of the effect of shell bending resistance in the model.

I. INTRODUCTION

Contrast agents are micron size bubbles that are encapsulated in a lipid polymer or albumin shell [1]. Today these bubbles are clinically established markers of vascularity and are used for quantitative blood flow and volume measurements [1]. Ongoing research has revealed their potential for quantification of microvasculature and perfusion [2-3]. Their advantage over conventional bubbles lies in the fact that the former remain in tact in the blood stream without dissolving or breaking up while at the same time emit a strong backscatter signal in the frequency range of diagnostic ultrasound (1-7 MHz). The efficacy of ultrasound contrast agents as a function of their physical characteristics and the properties of the ultrasound beam, i.e. amplitude and frequency, is a complex issue that warrants special analysis. SonoVue contrast agent microbubbles consist of an SF_6 bubble that is surrounded by a lipid polymer [4]. The viscoelastic properties of their shell are known from correlations between experimental measurements and theoretical predictions [4], for small amplitude acoustic disturbances. The model used in the aforementioned study is the one proposed by De Jong et al. [5], can be obtained from Church's model [6], considers finite shell thickness and employs the Kelvin-Voigt constitutive equation for the stress strain relationship in the shell and allows for nonlinear bubble oscillations. De Jong's model is recovered from Church's linearized model by allowing for negligible shell thickness. Nevertheless, both of the above studies do not rigorously account for liquid viscosity and compressibility. This is done in a more recent study by Khismatullin & Nadim [7] where the elasticity of the surrounding fluid is also introduced. In this fashion they obtain resonant frequencies and damping coefficients for linear oscillations. The effect of nonlinearity is addressed in [5] and it is shown that contribution from higher harmonics in the scattering cross section is suppressed when contrast agents are considered as opposed to free gas bubbles. In addition, owing to the larger stiffness exhibited by contrast agents they resonate at larger radii for given driving frequency, in comparison with free bubbles, and, consequently, emit a stronger backscatter signal. The combined effect of nonlinearity, shell viscoelastic properties and liquid viscosity and

compressibility on the above characteristics, are investigated in the present study for spherosymmetric oscillations.

Another important aspect of contrast agent dynamics refers to their shape deformation as they oscillate, in particular when they interact with neighbouring microbubbles or nearby obstacles. Drugs or genes can be carried in or on microbubbles, and the application of ultrasound fields appears to enhance focal release by disturbing or disrupting these microbubbles [8]. The destruction of microbubbles also offers the potential to assess myocardial blood flow via a destruction and replenishment technique [9]. Bubble fragments are significantly smaller than the original bubble and the received echo from them differs in amplitude and frequency from the one received from the original bubble. After fragmentation the gas content often escapes from the contrast agent forming a free bubble, which undergoes shape oscillations that alter the frequency spectrum. This phenomenon might explain reported differences in the backscatter cross-section, as this is measured experimentally and as it is predicted from models considering an encapsulated bubble [10]. An extensive account of numerical results obtained for bubble-bubble interaction [11,12], single bubble dynamics [13] and dynamics of contrast agents where shape oscillations are allowed, are provided in the following sections and, whenever available, a comparison is made against experimental measurements. Finally, conclusions are drawn and directions for future research are put forward.

II. SPHEROSYMMETRIC OSCILLATIONS OF SONOVUE™ MICROBUBBLES

We want to model spherosymmetric oscillations of a SonoVue™ microbubble in response to a disturbance in the far field pressure:

$$P_\infty = P_{St}\left(1+\varepsilon \sin \omega_f t\right). \tag{1}$$

The frequency of the disturbance, ω_f, lies in the ultrasound range of MHz while the amplitude, ε, may vary by several orders of magnitude. It is of interest to predict the scattering cross section for this type of bubbles, which corresponds to the quotient between the incident and the scattered acoustic intensity multiplied by the surface of the scatterer:

$$\sigma_{sc} = 4\pi r^2 \frac{\int_0^{t_r} P_{Sc}^2 dt}{\int_0^{t_r} P_{Ac}^2 dt}, \quad P_{Ac} = \varepsilon P_{St} \sin\left(\omega_f t\right), \quad P_{Sc}\left(r,t\right) = P\left(r,t\right) - P_{St}\left(t\right) - P_{Ac}\left(t\right). \tag{2}$$

In the same fashion the scattering cross-section of the n'th harmonic component of the scattered pressure, $P_{Sc,n}$,

$$\sigma_{sc,n} = 4\pi r^2 \frac{\int_0^{t_r} P_{Sc,n}^2 dt}{\int_0^{t_r} P_{Ac}^2 dt}, \tag{3}$$

can be defined. The above quantities are used as measures of the acoustic efficacy of the different contrast agents that are employed in a specific measurement.

As shown elsewhere [4] SonoVue™ microbubbles are better modeled as ideal gas bubbles surrounded by a constant thickness thin shell, Fig 1. In this fashion we adopt the Kelvin-Voigt model [6] for the encapsulating shell and the ideal gas model for the gas inside the bubble. Integrating the differential force balance across the shell thickness and applying continuity gives rise to the following relationship for the pressure on the shell-liquid interface measured on the liquid side:

$$P(r=R,t)=P_B(t)-\frac{2\gamma_1}{\alpha}-\frac{2\gamma_2}{R}+\chi^1_{rr}(r=R)-4\mu_s\left(\frac{\dot{\alpha}}{\alpha}-\frac{\dot{R}}{R}\right)-4G_s\left(\frac{\alpha-\alpha_e}{\alpha}-\frac{R-R_e}{R}\right), \quad (4)$$

where α, α_e and R, R_e correspond to the internal and external instantaneous and equilibrium radii of the shell, respectively, μ_s and G_s the viscosity and elasticity of the shell material, $P_B(t)$ the instantaneous bubble pressure and $\chi^1_{rr}(r=R)$ the deviatoric stress tensor defined in the surrounding liquid, which is taken to be Newtonian. In the limit of a shell with infinitesimally small but constant thickness, δ, the viscoelastic terms in eq. (4) read:

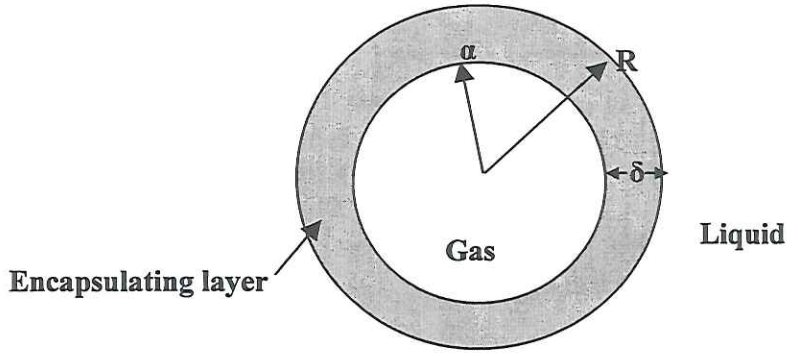

Fig. 1: Schematic diagram of a contrast agent

$$4G_s\left(\frac{\alpha-\alpha_e}{\alpha}-\frac{R-R_e}{R}\right)=2\left(2G_sR_0\frac{\delta}{R}\right)\left(\frac{1}{R_0}-\frac{1}{R}\right), \quad 4\mu_s\left(\frac{\dot{\alpha}}{\alpha}-\frac{\dot{R}}{R}\right)=2\left(2\mu_sR\frac{\delta}{R}\right)\frac{\dot{R}R}{R^3}, \quad (5)$$

$$\delta(t)=R(t)-\alpha(t), \quad R(t=0)=R_0=R_e$$

and eq. (4) collapses to the de Jong et al. model, [5], with R as the only unknown radius, or equivalently α, if only terms up to $O(\delta)$ are retained. In the following it is assumed that initially the microbubble is unstressed and that the bubble pressure varies adiabatically. Terms involving the shell elasticity and viscosity can be lumped as

$$S_p=2G_sR_0\frac{\delta}{R}, \quad \frac{S_F}{4\pi}=4\mu_sR\frac{\delta}{R}\rightarrow S_F=16\pi\mu_sR\frac{\delta}{R}, \quad (6)$$

in which case the model presented in [5] is recovered, with the understanding that thermal losses are not accounted for as they become negligibly small in the ultrasound frequency range [20]. The liquid surrounding the contrast agent is modeled as a Newtonian viscous and incompressible fluid in the vicinity of the interface whereas compressibility effects are accounted for in the far field [14, 15]. Consequently, the evolution of the microbubble's interface R with time is described via the following equation:

$$\left(1-\frac{\dot{R}}{c}\right)R\ddot{R}+\left(\frac{3}{2}-\frac{\dot{R}}{2c}\right)\dot{R}^2=\frac{1}{\rho}\left(1+\frac{\dot{R}}{c}\right)\left[P(r=R,t)-P_{St}-\varepsilon P_{St}\sin\omega_f t\right]+ \quad (7)$$

$$\frac{R}{\rho c}\frac{d}{dt}\left[P(r=R,t)-\varepsilon P_{St}\sin\omega_f t\right]$$

with c denoting the speed of sound in the surrounding liquid. Before the acoustic disturbance is applied the pressure everywhere in the liquid is set to P_{St}, the bubble radius is $R=R_0$ and the bubble pressure is determined by the compound surface tension between the gas and the liquid:

$$P_B(t=0) - P_{St} = 2\frac{\sigma_1 + \sigma_2}{R_0}. \quad (8)$$

Substituting eq. (4) in eq (7) we obtain a second order ODE that is solved numerically to provide the instantaneous bubble radius and pressure [16]. The latter is evaluated on the bubble's interface to produce the scattered pressure, which is then Fourier analyzed and introduced in eq's (2) and (3) in order to obtain the scattering cross section as a function of the physical parameters of the problem.

Introducing dimensionless variables by utilizing the initial radius R_0 and the inverse forcing frequency $1/\omega_F$ as characteristic space and time scales, we recover the problem formulation involving the following dimensionless quantities:

$$E = \frac{G_s}{\rho\omega_f^2 R_0^2},\ M = \frac{R_0\omega_f}{c},\ \frac{1}{We} = \frac{\gamma_1 + \gamma_2}{\rho R_0^3 \omega_f^2},\ Re = \frac{\rho\omega_f R_0^2}{\mu},\ Re_s = \frac{\rho\omega_f R_0^2}{\mu_s},\ \varepsilon, \quad (9)$$

signifying the dimensionless elasticity and the Mach, Weber the liquid and shell Reynolds numbers and the disturbance amplitude, respectively. In this fashion, the scattering cross section of the microbubble is calculated as a function of the forcing frequency and acoustic pressure amplitude, Fig 2, and is compared against the findings of linear theory. It is shown that as ε tends to zero the findings of linear theory are recovered. The discrepancy between linear and nonlinear theory in Fig. 2a is attributed to the finite step that was taken in ω_f for the identification of resonance. For large amplitudes higher harmonics, $n\omega_f$ n=1,2,3..., or subharmonics, ω_f/n n=1,2,3..., start appearing. This is an effect that warrants special attention in clinical ultrasound measurements.

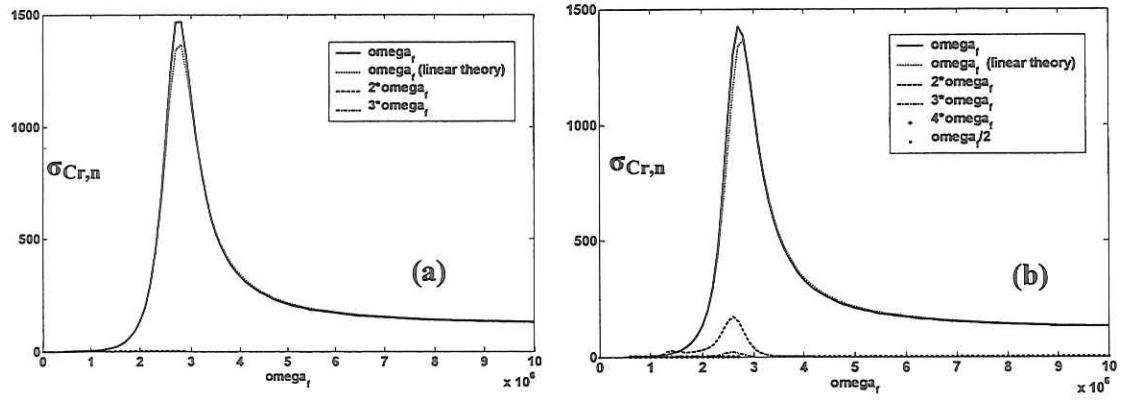

Fig 2: Scattering cross section $\sigma_{Sc,n}$ of a SonoVue™ microbubble as a function of forcing frequency ω_f when (a) ε=0.1 and (b) ε=1, corresponding to an amplitude of acoustic pressure of 10kPa and 100 kPa, respectively; the harmonics of ω_f that appear in the spectrum of the scattered pressure field are shown.

III. AXISYMMETRIC OSCILLATIONS OF MICROBUBBLES

When the break-up process of microbubbles needs to be captured shape oscillations have to be accounted for, thus relaxing the assumption of spherosymmetry. As a first step only shell elasticity and, for more generality, surface tension need be considered regarding the mechanical behavior of the interface which is taken to be of infinitesimal thickness. On the liquid side compressibility in the far field may be neglected when the amplitude of the oscillations is not very large, whereas liquid viscosity can be restricted in a thin boundary layer adjacent to the interface. The gas filling the bubble is treated as ideal while the force balance is satisfied at the interface,

$$\Delta\vec{f} = \left[\underline{\underline{\sigma}}^{i} - \underline{\underline{\sigma}}^{o}\right]\cdot\vec{n} = \left[-P_B\underline{\underline{I}} + P\underline{\underline{I}} - \underline{\underline{\chi}}\right]\cdot\vec{n} = \vec{q}, \tag{10}$$

where $\underline{\underline{\sigma}}$ represents the stress tensor, $\vec{n}$ the normal vector pointing inwards with respect to the liquid and

$$\vec{q} = \left(2\gamma k_m + k_s\tau_{ss} + k_s\tau_{ss}\right)\vec{n} - \left[\frac{\partial\tau_{ss}}{\partial s} + \frac{1}{r\sin\theta}\frac{\partial(r\sin\theta)}{\partial s}\left(\tau_{ss} - \tau_{\phi\phi}\right)\right]\vec{t}_s \tag{11}$$

the elastic force developed on an axisymmetric infinitesimally thin membrane as a result of deformation and surface tension γ; $k_m = \frac{k_s + k_\phi}{2} = \vec{\nabla}_s\cdot\vec{n}$ is the mean membrane curvature, $\vec{t}_s$ is the tangential vector along a meridian curve of the axisymmetric membrane and τ_{ss}, $\tau_{\phi\phi}$, the principal elastic tensions on the membrane [17]. The latter two quantities vanish in the absence of elasticity and the model for a free bubble is recovered. The principal elastic tensions are related to the 2D deformation tensor $\underline{\underline{e}}$ by means of the strain energy function per unit of initial membrane area $w(I_1,I_2)$,

$$\underline{\underline{\tau}} = \frac{2}{J_s}\left\{\frac{\partial w}{\partial I_1}\underline{\underline{A}}\cdot\underline{\underline{A}}^{T} + \frac{\partial w}{\partial I_2}J_s^2\left(\underline{\underline{I}} - \vec{n}\vec{n}\right)\right\},\quad \underline{\underline{A}} = \left(\underline{\underline{I}} - \vec{n}\vec{n}\right)\cdot\frac{\partial\vec{x}}{\partial\vec{X}}\cdot\left(\underline{\underline{I}} - \vec{N}\vec{N}\right),\quad \underline{\underline{e}} = \frac{1}{2}\left[\underline{\underline{A}}\cdot\underline{\underline{A}}^{T} - \left(\underline{\underline{I}} - \vec{N}\vec{N}\right)\right] \tag{12}$$

In the above $\vec{X}, \vec{x}$, and $\vec{N}, \vec{n}$, represent the position and normal vectors on the membrane surface at a reference and at the current configuration and $\underline{\underline{I}}$, $\underline{\underline{A}}$ the identity and displacement gradient tensors. The tensor $\underline{\underline{A}}\cdot\underline{\underline{A}}^{T}$ has two non zero eigenvalues λ_1^2, λ_2^2, associated with the principal extension ratios, $\lambda_i = \frac{ds_i}{dS_i}$ (no summation on i) with dS_i and ds_i denoting line elements in the reference and deformed states [18]. In addition, $J_s = \lambda_1\lambda_2$, $I_1 = \lambda_1^2 + \lambda_1^2 - 2$, $I_2 = \lambda_1^2\lambda_2^2 - 1$, and the principal non-zero strain components are

$$e_i = \frac{1}{2}\left(\lambda_i^2 - 1\right)\quad i = 1,2. \tag{13}$$

The extension of Hook's law, that accounts for large deformations, for a two dimensional surface is referred to as the neo-Hookean law with,

$$w = \frac{G_s}{2}\left(I_1 + 2 + \frac{1}{I_2 + 1}\right)\xrightarrow{\text{eq.(12)}}\underline{\underline{\tau}} = \frac{G_M}{\lambda_1\lambda_2}\left(\lambda_1^2 - \frac{1}{\left(\lambda_1\lambda_2\right)^2}\right) \tag{!4}$$

If the effect of membrane viscosity [19] is included we obtain

$$\underline{\underline{\tau}} = \frac{G_M}{\lambda_1\lambda_2}\left(\lambda_1^2 - \frac{1}{\left(\lambda_1\lambda_2\right)^2}\right) + 2\mu_s\frac{1}{\lambda_s}\frac{\partial\lambda_s}{\partial t},\qquad \lambda_s = \frac{\partial s/\partial\xi}{\partial S/\partial\xi},\quad \lambda_\phi = \frac{r\sin\theta\big|_t}{r\sin\theta\big|_{t=0}} \tag{15}$$

which van be viewed as the extension of the Kelvin-Voigt model for a two dimensional surface that undergoes large deformations; ξ is a Lagrangian variable identifying different particles.

The above formulation is complemented by the kinematic condition equating the fluid velocity at the interface to the velocity of particles that are lying on it

$$\vec{u} = \frac{d\vec{x}}{dt}, \tag{16}$$

the Bernoulli's law, when the flow in the liquid surrounding the bubble is considered to be potential, relating the pressure to the time variation of the velocity potential at the interface,

$$\frac{d\Phi}{dt}=\frac{1}{2}|u|^2+2P_\infty-2P,\quad \bar{u}=\bar{\nabla}\Phi \tag{17}$$

and the integral form of Laplace's equation that associates the potential to its normal derivative at the interface

$$-\Phi(\hat{r},\hat{\theta},t)+\int_0^1\left[\Phi(r,\theta,t)-\Phi(\hat{r},\hat{\theta},t)\right]\frac{\partial G}{\partial n}(\hat{r},\hat{\theta},r,\theta)\,r\sin\theta\left(r_\xi^2+r^2\theta_\xi^2\right)^{1/2}d\xi=$$
$$\int_0^1\frac{\partial\Phi}{\partial n}(r,\theta,t)\,G(\hat{r},\hat{\theta},r,\theta)\,r\sin\theta\left(r_\xi^2+r^2\theta_\xi^2\right)^{1/2}d\xi \tag{18}$$

with $\bar{n}$ pointing towards the fluid and G the free space kernel of the Laplacian [11,12,13]. This essentially reduces the dimensionality of the problem by one affording discretization of only a line rather than the entire meridian plane. The same formulation can be applied for the case of bubble-bubble interaction, provided the integrals in eq. (18) are extended to cover both interfaces taken to be axisymmetric [11]. Viscous effects can also be accounted for by properly integrating across the $O(Re^{-1/2})$ thin boundary layer surrounding the bubble [13]. The effect of surface tension and/or elasticity is incorporated in eq. (17) by substituting for the pressure P as this is calculated via the stress balance, eq. (10).

The numerical solution of the above set of equations is obtained via a hybrid finite boundary element method where only the meridian line has to be discretized [11,12,13]. When the far field pressure is perturbed the velocity potential at the interface is first updated via eq. (17). Next the normal derivative of the velocity potential is evaluated by solving the boundary integral eq. (18), thus providing the complete velocity vector at the interface, which is used to update the position of the interface in eq. (16) and provide the membrane deformation. Then the elastic stresses are calculated via eq. (11), with the help of the constitutive law and the obtained deformations, eq. (15), and the entire process is repeated for the next time step. The Runge-Kutta integrator is used for time integration, due to its improved accuracy characteristics.

In this manner the deformation and break-up of an elongated bubble is calculated when only isotropic tension i.e. surface tension is included [13]. It is shown that when the initial elongation exceeds a certain level the bubble eventually, Fig 3, collapses giving rise to a smaller bubble occupying the region around its center of mass and a larger torroidal one. This happens via the formation and coalescence of two countercurrent jets that travel along the axis of symmetry and meet at the equatorial plane. When viscous effects are included there is a lower threshold of Re below which the bubble does not break-up. Rather it oscillates and eventually returns to its equilibrium spherosymmetric configuration. When the case of bubble-bubble interaction is considered [11,12] it is seen the bubbles either attract or repel each other, depending on whether they oscillate in or out of phase, as predicted by the Bjerknes theory regarding secondary Bjerknes forces. In this process they accelerate and deform over the entire interface or on the side facing away from the direction of acceleration, depending on the acceleration level, Fig 4. In this case the bubble on the left is larger, moves slower and is deformed throughout its interface, whereas the bubble on the right moves faster and is thus deformed on the side facing away from the direction of acceleration.

When elasticity is included in the interfacial force balance then, in the presence of an oscillatory pressure disturbance and irrespective of the disturbance level, a bubble with an infinitesimally thin shell will eventually develop negative in plane tensions during the contraction phase of its oscillation and buckle, unless bending resistance is accounted for. In this process the bubble shape undergoes shape oscillations that modify the frequency spectrum. These effects cannot be captured when spherosymmetric oscillations are considered and are very important for predicting the coherence of contrast agents in an ultrasound environment. Consequently, further research is required in this direction in order

to determine the tolerance in the amplitude of pressure disturbances for contrast agents to remain in tact or, depending on the application, for controlled fragmentation of contrast agents to be achieved.

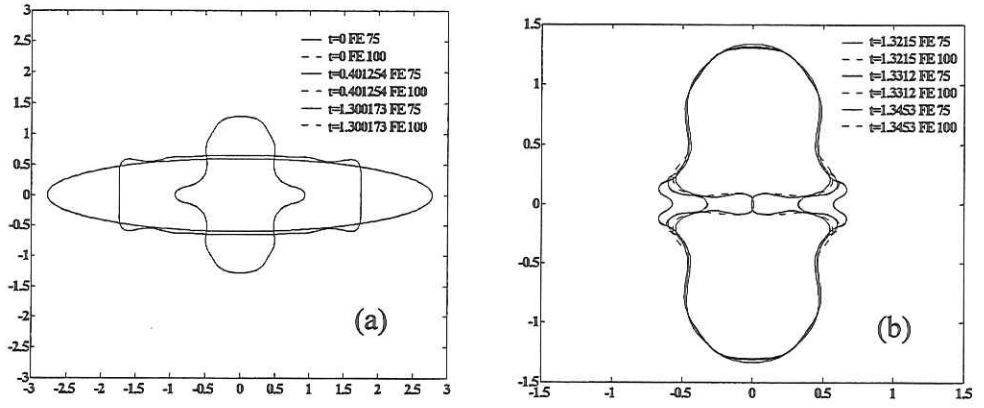

Fig. 3: Inviscid deformation of an initially elongated bubble with R=0.6 (ratio between the large semi-axis and the equilibrium radius R_0~5μm), (a) initially and (b) at break-up; results obtained with 75 and 100 elements in the region $0 \leq \theta \leq \pi/2$, are shown.

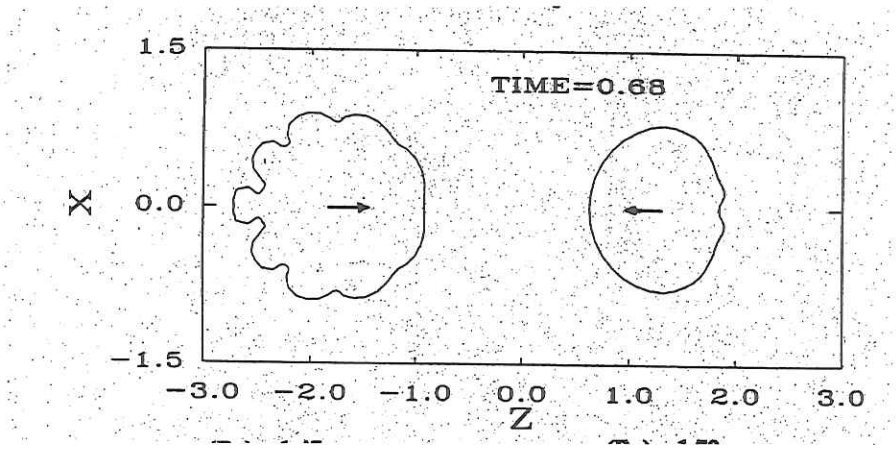

Fig. 4: Bubble shapes when the ratio between their equilibrium radii is R=0.8 and their dimensionless distance D=4, at atmospheric pressure; the equilibrium radius of the larger one is R_0~1mm.

Acknowledgement
This work was partly supported by the Government Scholarship Institution (IKY) of Greece.

References

1. Burns PN, Becher H. Handbook of Contrast Echocardiography. 2000 Springer, Berlin, Germany.
2. Wei K, Jayaweera AR, Firoozan S, Linka A, Skyba DM, Kaul S. Quantification of Myocardial blood flow with ultrasound-induced destruction of microbubbles administered as a constant venous infusion. Circulation 1998; 97: 473-483.
3. Burns PN. Harmonic imaging with ultrasound contrast agents. Clin Radiol 1996; 51: 50-55.
4. Gorce, J.M., Arditi M. & Schneider M. Influence of Bubble size distribution on the echogenicity of ultrasound contrast agents, Investigative Radiology, [35]11 661-671, 2000.
5. De Jong N., Cornet R. & Lancee C.T., Higher harmonics of vibrating gas-filled microspheres. Part one: simulations, Ultrasonics [32], 447-453, 1994.
6. Church C.C., The effects of an elastic solid surface layer on the radial pulsations of gas bubbles. J. Acoust. Soc. Am. [97] 1510-1521, 1995.
7. Khismatullin D. B. & Nadim A., Radial oscillations of encapsulated microbubbles in viscoelastic liquids. Phy. Fluids 14(10) 3534-3557, 2002.
8. Unger EC, Hersh E, Vannan M, Matsunaga TO & McCreery T. Local drug and gene delivery through microbubbles. Prog Cardiovasc. Dis. 44(1), 45-54, 2001.
9. Wei K., Jayaweera A. R., Firoozan S., Linka A., Skyba D. M. & Kaul S., Basis for detection of stenosis using venous administration of microbubbles during myocardial contrast echocardiography: Bolus or continuous infusion. Circulation 97(5) 473-483, 1998.
10. Sboros V, MacDonald CA, Pye SD, Moran CM, Gomatam J, McDicken WN. The Dependence Of Ultrasound Contrast Agents Backscatter On Acoustic Pressure: Theory Versus Experiment. Ultrasonics 2002; 40: 579-583.
11. Pelekasis N. A. & Tsamopoulos J. A., "Bjerknes forces between two bubbles. Part I: Response to a step change in pressure.", J. Fluid Mech. 254, 467-499 (1993).
12. Pelekasis N. A. & Tsamopoulos J. A., "Bjerknes forces between two bubbles. Part II: Response to an oscillatory pressure field.", J. Fluid Mech. 254, 501-527 (1993).
13. Tsiglifis K. & Pelekasis N., 'Weak viscous oscillation and collapse of elongated bubbles under small initial overpressure', submitted to the *Physics of Fluids, 2004.*
14. Keller J. B. & Miksis M, "Bubble oscillations of large amplitude", J. Acoust Soc. Am. 68(2) 628-633 (1980).
15. Prosperetti A. & Lezzi A., "Bubble dynamics in a compressible fluid. Part 1. First-order theory" J. Fluid Mech. 168, 457-478 (1986).
16. Tsiglifis K., Pelekasis N. A. & V. Sboros, "Large amplitude spherosymmetric oscillations of microbubbles" to be submitted to the J. Acoust Soc. Am.
17. Pozrikidis C. "Boundary integral and singularity methods for linearized viscous flow", Cambridge University Press, 1992.
18. Barthes-Biesel D., Diaz A. & Dhenin E. Effect of constitutive law for two dimensional membranes on flow-induced capsule deformation. J. Fluid mech. 460, 211-222 (2002).
19. Diaz A., N. A. Pelekasis & Barthes-Biesel D. Effect of membrane viscosity on the dynamic response of an axisymmetric capsule, Phys Fluids, 13(12) 3835-3838 (2001).
20. Prosperetti A. Thermal effects and damping mechanisms in the forced radial oscillations of gas bubbles in liquids. J. Acoust Soc. Am. 61(1) 17-27, 1977.

A model for large amplitude oscillations of coated bubbles accounting for buckling and rupture

Philippe Marmottant[1*], Sander van der Meer[1], Michel Versluis[1],
Nico de Jong[1,2], Sascha Hilgenfeldt[1†], and Detlef Lohse[1]
[1]*Department of Science and Technology, University of Twente,*
P.O.Box 217, 7500AE Enschede, The Netherlands and
[2]*Department of Experimental Echocardiography,*
Thoraxcentre, Erasmus MC, Rotterdam, The Netherlands

ABSTRACT

We present a model applicable to SonoVue® contrast agent bubbles that takes into account the physical properties of a lipid monolayer coating on a gas microbubble. Two parameters describe the properties of the shell: a buckling radius and the compressibility of the shell. The model presents an original non-linear behaviour at large amplitude oscillations, termed compression-only, induced by the buckling of the lipid monolayer. This prediction is validated by experimental recordings. The effect of aging or the resultant of repeated acoustic pressure pulses on bubbles is predicted. It corrects a flaw in the shell elasticity term previously used in the dynamical equation for coated bubbles. The break-up is modeled by a critical shell tension above which gas is directly exposed to water.

INTRODUCTION

Contrast agent SonoVue® microbubbles contain SF_6, a gas whose solubility in water is low, and are coated with a monolayer of surfactants molecules adsorbed at the interface. The coating stabilize the bubbles and prevents coalescence. Pulmonary alveoli in the lungs have a lipid coating for the same reason [1]. The coating modifies the effective surface tension. Since surface tension plays a crucial role in the dynamics of small bubbles, when the capillary pressure term is of the order of the initial pressure, the coating is expected to play a large role in the dynamics.

The current models developed to describe coated bubble oscillations all implicitly assume small deformations of the bubble surface: however, in practice, insonifying contrast agent bubbles produces oscillations leading to large variations in the surface area.

We will present in this manuscript a model designed to incorporate the effect of a coating on the microbubble response to ultrasound, and to specifically capture the high-amplitude dynamics.

* *Present address:* Laboratoire de Spectrométrie Physique, CNRS-Université Joseph Fourier, BP 87, F-38402 Saint Martin d'Hères, France
† *Present address:* Engineering Sciences & Applied Mathematics and Dept. of Mechanical Engineering, Northwestern University, 2145 Sheridan Road, Evanston, IL 60208, USA

SURFACE TENSION OF PHOSPHOLIPIDIC MONOLAYERS

The monolayer adsorbed on the SonoVue® microbubbles contains phospholipid molecules: distearoylphosphatidylcholine (DSPC) and dipalmytoylphosphatidylglycerol (DPPG) [2]. It also contains a stabilizer, polyethylene glycol 4000 (PEG-4000), whose length is about 90 monomers [3], that acts like a brush anchored in the bubble surface and prevents coalescence [4]. The phospholipid molecules naturally adsorb to the interface [5] and shield the water from the air, reducing the surface tension to a value lower than that of pure water (73 mN/m). Surface tension can be measured in a flat monolayer with the Langmuir-Blodgett balance, or on centimetric bubbles [6], showing its dependence on the surface concentration of molecules.

The compression of the monolayer decreases the area available per molecule. When this area reaches that covered by the lipid heads (typically 0.4 nm^2 for phospholipids), the effective surface tension decreases sharply, see figure 1, with an elastic compression modulus $\chi = A\frac{d\sigma}{dA}$ (of order 0.2 N/m for a slow compression). Further compression leads to an unstable situation where the monolayer buckles out of plane, while the surface tension nearly vanishes. A spectacular demonstration of the buckling is the appearance of wrinkles on coated bubbles when their gas dissolves [4]. Buckling can be reversible [7, 8].

In contrast, a slow expansion separates molecules from each other: surface tension rises. Pure lipid composition will show phase changes from a 2D solid state, to a liquid and eventually gaseous state, where surface tension is close to that of water. A mixture of lipid molecules will not exhibit marked phase changes, and an amorphous 2D solid can rupture, leaving rafts of solid phospholipid molecules separated by clean interfaces [9].

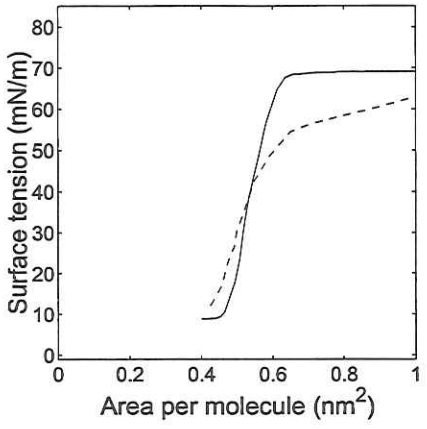

FIG. 1: Effective surface tension versus area per molecule at the interface for two phopholipids (both present in SonoVue®) under *slow compression* (A few % per minute): DSPC, solid line; and DPPG, broken line. Curves taken from [10, 11].

Most previous existing experimental data on phospholipidic monolayers were collected at very slow compression/expansion rates, when molecules at the interface could equilibrate. Only a few experiments revealed the high-frequency and thus out-of equilibrium trends: the buckling surface tension comes closer to zero and the elastic modulus becomes higher (see [1], experiments with pulmonary surfactant compressed within 0.2s). These findings give some hint to the extrapolation of surface properties to the realm of high frequency oscillations, the one we are going to explore

with oscillating contrast agent bubbles.

MODEL FOR THE EFFECTIVE SURFACE TENSION OF A BUBBLE

At high frequencies, we propose to model the effective surface tension σ of the lipidic monolayer of a bubble along three linear regimes, depending on the bubble area $A = 4\pi R^2$, with R the bubble radius (see figure 2). This simplified model is designed to capture the coated bubble dynamics with a minimum of parameters.

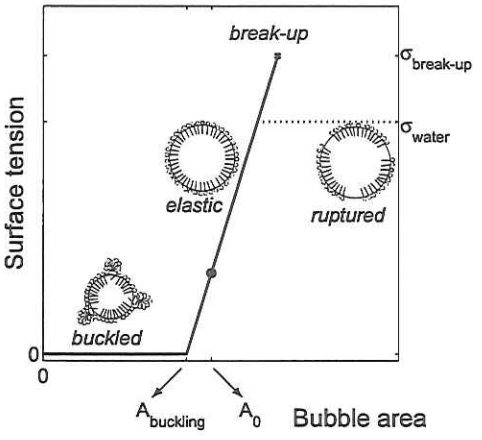

FIG. 2: Model for the dynamic surface tension of a monolayer coated bubble (continuous line). The coating has a fixed number of lipid molecules, which corresponds to a monolayer at equilibrium (when area is A_0). The tension saturates to the water value σ_{water} (broken line) after the break-up tension has been reached ($\sigma_{\text{break-up}} > \sigma_{\text{water}}$, see main text).

The model has two parameters only to describe the surface tension: the buckling area of the bubble A_{buckling} below which the surface buckles, and an elastic modulus χ that gives the slope of the elastic regime. An additional parameter is added to describe the moment of rupture: the elastic regime holds until critical break-up tension called $\sigma_{\text{break-up}}$, and when this limit has been reached the maximum surface tension saturates at σ_{water}.

We motivate here the modeling of the three states:

- Buckled state, $\sigma = 0$.
  Consistent with experimental findings on the fast compression of pulmonary phospholipid monolayers, we assume a near vanishing surface tension in the buckled state [1]. The buckling area of the bubble depends on the number n of lipid molecules at the interface and on the molecular area at buckling a_{buckling}, with $A_{\text{buckling}} = n\, a_{\text{buckling}}$. For phospholipids a_{buckling} is typically of the order of 40 Å^2. Note that a first compression of the bubble might *expel* in bulk some molecules into the bulk [12], decreasing the number n. After this transient expulsion, we expect the number of molecules to remain constant, as phospholipids with large carbon chains (here 16 and 18 carbons) are poorly soluble.

- Elastic state, $\sigma = \chi\left(\frac{A}{A_{\text{buckling}}} - 1\right)$.
  The shell is elastic only in narrow area range. The lower limit is A_{buckling} for the area, or equivalently R_{buckling} for the radius. The upper limit radius is fixed by the maximum

surface tension, which is $\sigma_{\text{break-up}}$ before rupture of the shell giving $R_{\text{break-up}} = R_{\text{buckling}}(1+\sigma_{\text{break-up}}/\chi)^{1/2}$, or σ_{water} after rupture giving $R_{\text{ruptured}} = R_{\text{buckling}}(1+\sigma_{\text{water}}/\chi)^{1/2}$. The elastic regime holds only in a narrow range of radii, since χ is usually large compared to $\sigma_{\text{break-up}}$ or σ_{water}. The value of the elastic modulus also incorporates the presence of any polymer component, such as the polyethyleneglycol (PEG) in SonoVue® . We assign a constant elastic modulus in this state, slightly caricaturing the quasi-static profiles of figure 1, a simplification of the model to facilitate calculation.

Within this regime the surface tension is a linear function of the area, or of the square of the radius, and around a given radius R_0, it can be writen as for small variations:

$$\sigma(R) = \sigma(R_0) + \chi\left(\frac{R^2}{R_0^2} - 1\right) \simeq \sigma(R_0) + 2\chi\left(\frac{R}{R_0} - 1\right) \quad \text{when} \quad |R - R_0| \ll R_0. \tag{1}$$

The lipid monolayer behaves as if composed of a thin solid and elastic material, see the appendix for the derivation of the tension of a thin elastic shell.

- Ruptured state, $\sigma = \sigma_{\text{water}}$.
  A fast expansion, such as the one triggered on a bubble by an ultrasonic pressure pulse, does not allow much time for any phase change and the monolayer is likely to break at critical tension $\sigma_{\text{break-up}}$, exposing bare gas interfaces to the liquid. The bare interface has a tension value of σ_{water}. The break-up tension is higher than σ_{water}, since the PEG polymer component confers more cohesion to the shell, and shifts the break-up to higher tensions. The introduction of a high tension break-up was motivated by the observation of resistant bubbles, as will be exposed further.

  After break-up we assume that surface tension relaxes to σ_{water}. Even if the phospholipid monolayer rafts are likely to display non-isotropic tensions and shear stresses (being solid), the expansion is uniform before rupture, and the stress is likely to remain close to uniformity on average. The tension value is settled by the equilibrium with the water interface that pulls on it, σ_{water}.

DYNAMICS OF THE COATED BUBBLE

During the oscillation the dynamical surface tension, a function of the bubble area and therefore of the bubble radius, will vary. We therefore write the effective surface tension $\sigma(R)$ to emphasize this dependence. In motion, the balance of normal stresses at the interface therefore reads

$$P_g - P_l = \frac{2\sigma(R)}{R} + 4\mu\frac{\dot{R}}{R} + 4\kappa_s\frac{\dot{R}}{R^2}, \tag{2}$$

with P_g the gas pressure in the bubble, P_l the liquid pressure, μ the surrounding liquid viscosity and κ_s the dilatational viscosity from the monolayer. The first term on right-hand side is the capillary pressure term, while the second is the stress arising from the frictions in the liquid and the third from frictions in the shell. Last term was derived for a layer of finite and constant thickness ϵ ($\epsilon \ll R$) by Morgan et al. [13], the dilatational viscosity writing $\kappa_s = \epsilon\mu_{\text{lipid}}$, with μ_{lipid} the bulk lipid viscosity. Here we use only κ_s to describe the shell.

The Laplace capillary pressure term $\frac{2\sigma}{R}$ is *not modified* by an effective surface tension, contrary to a previous statement in an article by Glazman [14], who expressed the capillary pressure by

the erroneous expression $\frac{2\sigma}{R} + \frac{\partial\sigma}{\partial R} = \frac{2}{R}(\sigma + \chi(\frac{R_0}{R})^2)$. We demonstrate here why: the capillary overpressure derives from the mechanical equilibrium of all forces, that is the infinitesimal work δW vanishes for small bubble radius variation. By definition, the work associated with a variation dA of the area is σdA [15], while the pressure work from a variation dV of the volume is $-(P_g - P_l)dV$. In equilibrium, the sum of these works vanishes, and we obtain the static capillary term of equation (2). In the analysis by Glazman the surface work is expressed incorrectly by $\sigma dA + Ad\sigma$ (instead of σdA), from a surface energy $E = \sigma A$, which is in fact valid only when σ is constant.

The popular model of Morgan et al. [13] for coated microbubbles improves the description of viscous frictions, but is based on the analysis of Glazman for the elasticity of the lipid shell, equivalent to the introduction of an effective surface tension $\sigma(R) = \sigma_0 + \chi(\frac{R_0}{R})^2$ that fails to describe a coated bubble. Physically it would mean that surface tension always decreases when the bubble is inflated, in contrast with the behavior of lipid monolayers or elastic solid shells.

The hydrodynamics of the liquid motion around the bubble is modeled by the (modified) Rayleigh-Plesset equation $\rho_l(R\ddot{R} + \frac{3}{2}\dot{R}^2) = P_l - P_0 - P_{ac}(t) - \frac{R}{c}\frac{dP_g}{dt}$, with P_0 the ambient pressure, $P_{ac}(t)$ the acoustic pressure, and c the velocity of sound in the liquid. This equation proved to be accurate and robust even in the extreme conditions of sonoluminescence [16]. We choose an ideal polytropic ideal gas law $P_g \propto R^{-3\kappa}$, with κ the polytropic gas exponent. It is 1 for micrometric small bubbles behaving isothermally, and equal to the ratio of specific heats for large bubbles behaving adiabatically [17] (close to 1.095 for SF_6).

Combining the Rayleigh-Plesset equation and the polytropic gas law with the boundary condition (2) we obtain the model for the bubble dynamics:

$$\rho_l\left(R\ddot{R} + \frac{3}{2}\dot{R}^2\right) = \left(P_0 + \frac{2\sigma(R_0)}{R_0}\right)\left(\frac{R}{R_0}\right)^{-3\kappa}\left(1 - \frac{3\kappa}{c}\dot{R}\right) - P_0 - \frac{2\sigma(R)}{R} - \frac{4\mu\dot{R}}{R} - \frac{4\kappa_s\dot{R}}{R^2} - P_{ac}(t), \tag{3}$$

with R_0 the equilibrium radius of the bubble. This equation is identical to a free gas bubble equation, except from the effective surface tension $\sigma(R)$, expressed in our monolayer model described above, and expressed here in terms of the bubble radius:

$$\sigma(R) = \begin{cases} 0 & \text{if } R \leq R_{\text{buckling}} \\ \chi\left(\frac{R^2}{R_{\text{buckling}}^2} - 1\right) & \text{if } R_{\text{buckling}} \leq R \leq R_{\text{break-up}} \\ \sigma_{\text{water}} & \text{if ruptured and } R \geq R_{\text{ruptured}} \end{cases} \tag{4}$$

The third regime appears after rupture of the shell, when $\sigma_{\text{break-up}}$ has been reached (see broken line of fig. 2).

For small vibration amplitudes within the tensed state, the surface tension can be linearized around a constant value, with $\sigma(R) \simeq \sigma(R_0) + 2\chi\,(R/R_0 - 1)$, from equation (1). Implemented in the dynamical equation its yields the same pressure term $-2\sigma(R)/R = -2\sigma(R_0)/R - 4\chi(1/R_0 - 1/R)$ than in the model proposed by de Jong et al. [18] for thin elastic shells. The shell stiffness coefficient S_p they introduced is simply related to the present shell elasticity by $S_p = 4\chi$. We stress here again that the model by de Jong et al. [18] is limited to small amplitudes of vibration (for effective tensions bounded between 0 and σ_{water}, or for R in between R_{buckling} and R_{collapse}), while the present model extends the oscillation to unbounded, large amplitudes.

IMPLICATIONS OF THE MODEL

Bubble compressibility

The effective tension model changes drastically the compressibility of the bubble. For slow variations of the ambient pressure P, at frequencies small compared to the resonance frequency, we can compute the equilibrium radius response, see figure 3, setting $\dot{R} = 0$ in equations (3) and (4).

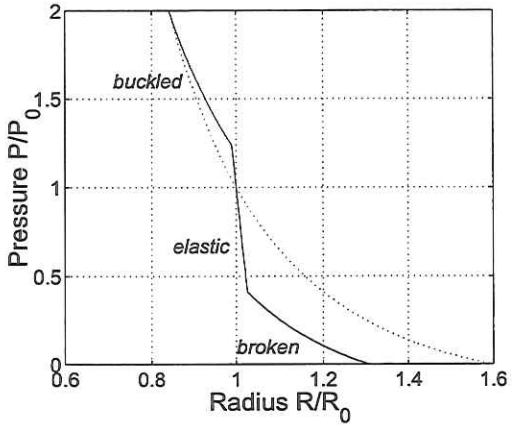

FIG. 3: Ambient pressure versus equilibrium radius for a coated bubble (continuous line) and a free gas bubble (dotted line). At atmospheric pressure, the bubble radius is $R_0 = 2$ μm. The coated bubble is initially in the elastic state ($R_{\text{buckling}} = 1.98$ μm, $\chi = 1$ N/m.)

From the equilibrium, we also derive the compression modulus of the bubble, K_V, with:

$$K_V = -V\left(\frac{dP}{dV}\right) = \begin{cases} \kappa P & \text{for the buckled state} \\ \kappa P + \frac{4}{3}\frac{\chi}{R} & \text{for the elastic state} \\ \kappa P + \frac{3\kappa-1}{3}\frac{2\sigma_{\text{water}}}{R} & \text{for the free bubble/broken shell state} \end{cases} \tag{5}$$

with V the bubble volume, and a polytropic exponent κ close to 1 for slow and isothermal compressions. The compression modulus is much higher when the bubble is in the elastic state, since usually $\chi \gg \sigma_{\text{water}}$. This is reflected in the much smaller slope of the curve of figure 3. When the pressure is increased enough the bubble buckles, and becomes very compressible, even more than an uncoated free gas bubble.

The change in compressibility is reflected on the dynamics of small amplitude oscillations as well. The linearization of the equations, setting $R(t) = R_0(1 + x(t))$, provides a damped oscillator equation $\ddot{x} + 2\gamma\dot{x} + \omega_0^2 x = -P_{ac}(t)/\rho_l R_0^2$, with a a damping coefficient $\gamma = 2\mu/\rho_l R_0^2 + 2\kappa_s/\rho_l R_0^3 + 3\kappa P_g/2c\rho_l R_0$, and an eigenfrequency simply writing:

$$\omega_0^2 = \frac{3}{\rho_l R_0^2} K_V. \tag{6}$$

In the free bubble state, this equation provides the Minnaert frequency as expected. It can be concluded that bubbles in the elastic state have a much higher resonance frequency than free or buckled bubbles, because their compression modulus is higher, and consistently with the derivation of de Jong [18].

Compression-only behavior

At small acoustic amplitudes the model presented above provides a linear radius response to the pressure similar to other Rayleigh-Plesset models with constant surface tension.

With large pressure amplitudes, the bubble will experience an original non-linear response. It will likely buckle in its compression phase, which cancels out any surface tension. On the other hand the surface tension rapidly rises during the expansion phase, and this asymmetry in surface tension provides an asymmetry in capillary pressure, especially strong for small bubbles. The radius response curve displays this asymmetry by a 'compression-only' behaviour.

Recent experiments, realised with the high-speed camera Brandaris 128 [19], reveal the existence of such asymmetric oscillations (see figure 4a). The experiment was conducted as follows: SonoVue® contrast bubbles, supplied by Bracco Research SA, Geneva, Switzerland, were prepared in the vial about 24 hours prior to the recording of their dynamics. The contrast bubbles were led through a capillary fiber inside a small water-filled container. A broadband single element transducer was mounted at 75 mm from the capillary. An Olympus microscope with a 60x high resolution water immersed objective and a 2x magnifier produced an image of the contrast bubbles. The image was then relayed to the high speed framing camera Brandaris 128. A Tektronix AWG 520 arbitrary waveform generator provided a signal amplified by an ENI A-500 amplifier. The bubble response was investigated with sequential ultrasound bursts of 8 cycles at frequencies ranging from 1.5 MHz to 5 MHz. The camera was operated at a framing rate of 15 million frames per second, resolving the insonified microbubble dynamics. From the images the radius versus time curves for each individual bubble were extracted.

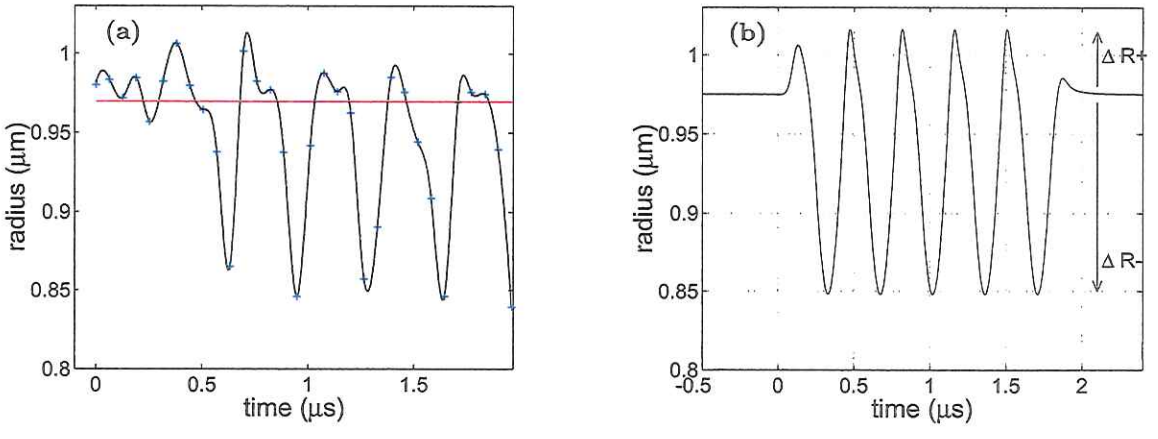

FIG. 4: (a) Experimental recording of the radius of a SonoVue® bubble versus time, with the fast framing camera Brandaris (2.9 MHz pulse with an acoustic pressure of 130 kPa). (b) Simulation. The fitted shell parameters are $R_{\text{buckling}} = R_0 = 0.975$ μm, $\chi = 10$ N/m, $\kappa_s = 5 \times 10^{-9}$ N and $\sigma_{\text{break-up}} > 1$ N/m (resistant shell). The liquid properties are $\rho_l = 10^3$ kg/m^3, $\mu = 0.001$ Pa.s, $c = 1480$ m/s and the polytropic gas exponent is $\kappa = 1.095$.

This phenomenon is very well modeled with our effective surface tension model, see figure 4b, assuming the bubble to be initially in a tension-less state ($R_{\text{buckling}} = R_0$), and allowing the shell to support elevated tensions. Note that the fitted elastic modulus of this shell is higher than the average shell modulus measured on bubble populations by Gorce et al. [20], who deduced an average shell elasticity $\chi = S_p/4 = 0.28$ N/m.

Aging of micro-bubbles: effect on the oscillation response

The initial effective tension of the monolayer depends on the history of the bubble. During their formation in the vial, lipid molecules are adsorbed at the interface, which reduces the effective surface tension in proportion to the concentration n/A of adsorbed lipid molecules. The bubble is initiated in the tensed elastic state, its area being above the buckling area, determined by $A_{\text{buckling}} = n * a_{\text{buckling}}$.

Dissolution of the gas in the liquid will 'deflate' the bubble and reduce its area towards a tension-less state (like the deflation of a rubber balloon), below which the bubble will buckle. In the tension-less state dissolution is much slower, since the capillary overpressure vanishes: bubbles therefore spontaneously tend to their buckling radius, and then shrink much more slowly, by diffusion only. The reduction of surface tension is the main mechanism to account for increased longevity, since the permeability of 16 and 18-carbons phospholipids coatings is high [4].

Experiments show that asymmetric oscillations responses become more pronounced in the course of dissolution, see figure 5. Our interpretation is that the bubble reaches the tension-less state, where buckling occurs. According to present model, the asymmetry is the signature of a contrast in surface tension during each cycle, and this contrast is the highest near buckling.

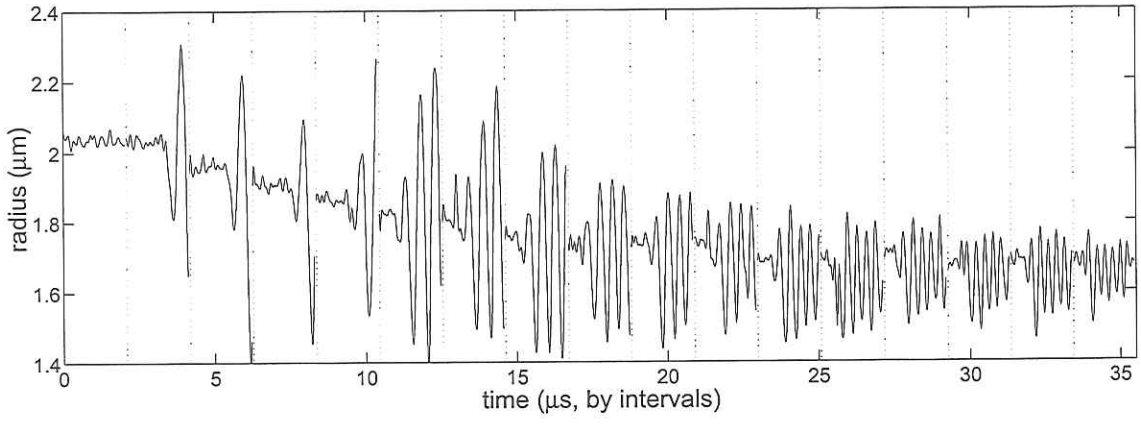

FIG. 5: Experimental recordings of repeated acoustic pulses of 100 kPa on a single bubble, separated by 50 ms (juxtaposed graphs). The oscillation asymmetry increases pulse after pulse. (Frequency is increasing from 1.5 to 4 MHz, inducing amplitude changes).

The asymmetry can be monitored by the ratio $\Delta R^+/\Delta R^-$ of the positive and negative radius excursions (defined by $\Delta R^+ = \max(R) - R_0$ and $\Delta R^- = R_0 - \min(R)$, materialized on figure 4b). Simulations show indeed that the compression-only asymmetry ($\Delta R^+/\Delta R^- < 1$), is the more pronounced when $R_0/R_{\text{buckling}} \sim 1$ (see figure 6a), the tension asymmetry during the oscillation being maximal. This behavior is to be contrasted with the oscillation of bubbles at large amplitudes with a constant surface tension, that tends to produce higher positive excursions, as seen on the same figure when the bubble radius is well above R_{buckling} (free bubble state, $\sigma = \sigma_{\text{water}}$) or well below R_{buckling} (tension-less state, $\sigma = 0$).

Repeated pulses on a bubble accelerate the gas dissolution, as evidenced on figure 5 by the sudden decrease after the first pulse and the subsequent pulses. Two mechanisms could account for this effect. First, the initial pulses may expel some lipid molecules and reduce the buckling

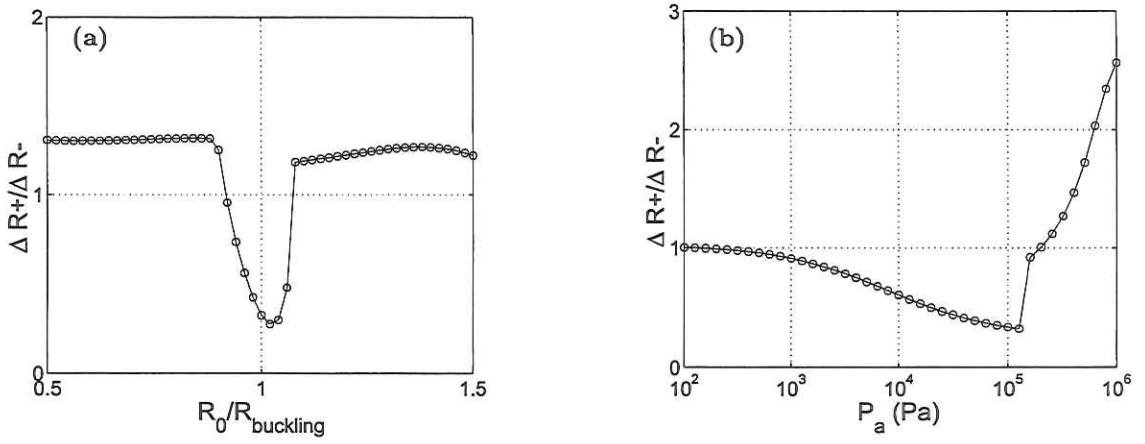

FIG. 6: (a) Simulated asymmetry of the oscillation for varying starting radii. Acoustic pulse and shell properties: same as figure 4. (b) Simulation with an increasing acoustic pressure ($R_{\text{buckling}} = R_0 = 1$ μm). Rupture at $\sigma_{\text{break-up}} = 1$ N/m.

radius, to which the bubble will relax. Another explanation would be an 'inverse' rectified-diffusion generated by compression-only behaviors. The gas pressure increases during the compression phase, while it remains close to the rest pressure at expansion (a symmetric oscillation would alternately compress and expand the gas). The concentration of gas in the liquid near the interface being proportional to gas pressure (Henry's law), the asymmetry, even small, tends to force more gas out of the bubble. This 'inversed' rectified-diffusion would be the opposite of the usual rectified-diffusion effect that counteracts dissolution for free gas bubbles [21].

Rupture of the shell

The shell can withstand finite tensions in its shell. Above a critical tension, $\sigma_{\text{break-up}}$, the shell ruptures and part of the bubble surface is uncovered. Once this threshold has been reached, the surface tension upper bound will be the surface tension of water, σ_{water}. We can therefore simulate the effect of an increasing acoustic pressure on a bubble (see figure 6b) . The compression-only behavior ($\Delta R^+/\Delta R^- \ll 1$), being a non-linear effect, appears for sufficiently large acoustic amplitudes. This evolution is interrupted by the break-up of the shell, a process called 'sonocracking' in the ultrasound literature. The non-linear behavior then favors positive excursions of the radius, the bubble possessing bare interfaces, as for standard large pressure Rayleigh-Plesset dynamics.

CONCLUSIONS

We presented a simple model for the dynamical properties of coated contrast agents bubbles at acoustic pressure, with two parameters: a buckling surface radius and a shell compressibility. It predicts a highly non-linear response, a compression-only behavior of the bubble, when its radius is close to the buckling radius, a state that naturally occurs with dissolution of gas, or that can be accelerated by repeated pulses. High-frequency image recordings reveal the existence of such asymmetric bubble oscillations, and validate the model. The break-up of the shell is modeled by a third parameter, finite tension of the bubble shell above which bare interfaces are created, with a

corresponding change in bubble dynamics.

Possible applications of the model include: the characterization of coated microbubbles, the description of acoustic echoes and their use in non-linear or pulse-inversion imaging, and the prediction of the effect of repeated pulses or of long-term experiments.

ACKNOWLEDGMENT

We would like to thank Joris Timmermans for his help in computations. We appreciated fruitful discussions with François Graner.

APPENDIX: COMPARISON WITH THE ELASTICITY OF A SOLID SHELL LAYER

The elasticity of a thin shell is characterized by a two-dimensional compression modulus $\chi = A\frac{d\sigma}{dA}$, where σ is the isotropic in-plane tension (shear of the surface does not occur, and bending is neglected assuming an initial curvature close to the spontaneous curvature). The shell has two interfaces, with a surface tension σ_1 for the inner interface and σ_2 for the outer interface. The mechanical equilibrium balance for any small change in bubble area around the tensionless shell area A_0 reads $\delta W = \chi(A/A_0 - 1)dA + \sigma_1 dA + \sigma_2 dA - (P_g - P_l)dV = 0$, from which we obtain the pressure jump at the liquid-gas interface $P_g - P_l = 2(\sigma_1 + \sigma_2 + \chi(A/A_0 - 1))/R$. The effective surface tension of the shell reads:

$$\sigma = \sigma_1 + \sigma_2 + \chi\left(\frac{R^2}{R_0^2} - 1\right), \tag{7}$$

it is a linear function of the bubble area, like in the lipid coated bubble model (Eq. 1 for the elastic state, with $\sigma(R_0) = \sigma_1 + \sigma_2$).

The model for a thick elastic shell by Church [22] provides the same effective surface tension when the shell thickness ϵ tends to be small in front of the radius. In this model the shell has a bulk shear modulus G_s and is incompressible. The two-dimensional elasticity of a thin incompressible elastic shell is $\chi = 3G_s\epsilon$. Replacing this expression for χ in the overpressure term in the Church model we find again equation (7).

[1] J. M. Crane and S. B. Hall, Biophys. J. **80**, 1863 (2001).
[2] M. Schneider, M. Arditi, M.-B. Barrau, J. Brochot, A. Broillet, R. Ventrone, and G. Yan, Invest. Radiol. **30**, 451 (1995).
[3] P. L. Hansen, J. A. Cohen, R. Podgornik, and V. A. Parsegian, Biophys. J. **84**, 350 (2003).
[4] M. A. Borden and M. Longo, Langmuir **18**, 9225 (2002).
[5] S. Lee, D. H. Kim, and D. Needham, Langmuir **17**, 5544 (2001).
[6] J. M. Crane, G. Putz, and S. B. Hall, Biophys. J. **77**, 3134 (1999).
[7] A. Saint-Jalmes, F. Graner, F. Gallet, and B. Houchmandzadeh, Euro. Phys. Lett. **28**, 565 (1994).
[8] A. Saint-Jalmes and F. Gallet, Eur. Phys. J. B. **2**, 489 (1998).
[9] F. Graner, S. Perez-Oyarzun, A. Saint-Jalmes, C. Flament, and F. Gallet, J. Phys. II France **5**, 313 (1995).
[10] F. Pétriat, E. Roux, J.-C. Leroux, and S. Giasson, Langmuir **20**, 1393 (2004).
[11] M. I. Sández, A. Suárez, and A. Gil, J. Colloid Interface Sci. **250**, 128 (2002).

[12] J. Gaines, G. L., *Insoluble Monolayers at Liquid-Gas Interfaces* (Interscience Publishers, New York, 1966).

[13] K. E. Morgan, J. S. Allen, P. A. Dayton, J. E. Chomas, A. L. Klibanov, and K. W. Ferrara, IEEE Transaction on ultrasonics, ferroelectrics, and frequency control **47** (2000).

[14] R. E. Glazman, J. Acoust. Soc. Am. **74**, 980 (1983).

[15] P.-G. de Gennes and F. Brochard-Wyart, *Capillarity and wetting phenomena: drops, bubbles, pearls, waves* (Springer, 2004).

[16] M. P. Brenner, S. Hilgenfeldt, and D. Lohse, Rev. Mod. Phys. **74**, 425 (2002).

[17] A. Prosperetti, Ultrasonics **22**, 69 (1984).

[18] N. de Jong, R. Cornet, and C. Lancée, Ultrasonics **34**, 447 (1994).

[19] C. T. Chin, C. Lancée, J. Borsboom, F. Mastik, M. Frijlink, N. de Jong, M. Versluis, and D. Lohse, Rev. Sci. Instrum. **74**, 5026 (2003).

[20] J. M. Gorce, M. Arditi, and M. Schneider, Invest. Radiol. **35**, 661 (2000).

[21] S. Hilgenfeldt, D. Lohse, and M. P. Brenner, Phys. Fluids **8**, 2808 (1996).

[22] C. C. Church, J. Acoust. Soc. Am. **97**, 1510 (1995).

ULTRASOUND ANGIOGRAPHIC IMAGING

Wilko Wilkening[1], Thilo Hölscher[2]

[1]Center of Excellence for Medical Engineering (Kompetenzzentrum Medizintechnik Ruhr, KMR), c/o Institute of High Frequency Engineering, Ruhr-University Bochum, Bochum, Germany, www.kmr-bochum.de

[2]University of California, San Diego, Department of Radiology, San Diego, CA, USA

INTRODUCTION

Advances in ultrasound imaging systems and in ultrasound contrast agents have quickly moved the focus of ultrasound contrast imaging research from Doppler signal enhancement and left ventricular opacification to perfusion and molecular imaging. Despite these advances, the field of vascular imaging with contrast agents has not been fully explored, yet. And there are applications, where neither Doppler techniques nor crossover techniques like B-Flow or SieFlow provide sufficient resolution or sensitivity. Examples for new directions were presented at this conference in 2003 by Jeff Powers and in 2004 by Naohisa Kamiyama. While the aforementioned work is related to microvascular imaging, our goal is angiographic imaging of the major brain arteries and of aneurysms.

METHODS

We performed transcranial imaging on patients who were scheduled for cerebral X-ray angiography using either a Siemens Sonoline® Elegra with a 2.5PL20 probe or a Siemens Sonoline® Antares with a PX4-1 probe. The ultrasound systems were set up to image in phase inversion mode, which is useful for imaging the nonlinear response and the destruction of microbubbles. A frame rate of more than 5 Hz was chosen to image intensity variations that are related to the heart rate without aliasing. Depending on the individual temporal bone window, the transmit power was adjusted so that the destruction of microbubbles prevented a strong signal enhancement in the perfused tissue but still allowed a significant enhancement in the major arteries. Images were recorded over about 15 s, where imaging started shortly before the contrast agent (Imagent®, IMCOR, a division of Photogen Technologies, Inc., San Diego, CA) entered the imaging plane.

Fig. 1 shows a typical time-intensity curve. The curve is characterized by the peak intensity and by a cyclic intensity variation that results from the heart cycle. This ripple is relatively weak in the major arteries, where the concentration of microbubbles is high (saturation) and where destroyed microbubbles are rapidly replaced. Consequently, in arteries with lower flow rate, the amplitude of the ripple is higher. The phase of the ripple as a function of position or distance can also be used to extract flow information. There are not too many cases, however, where the flow velocities and the vessel topology would allow such calculations.

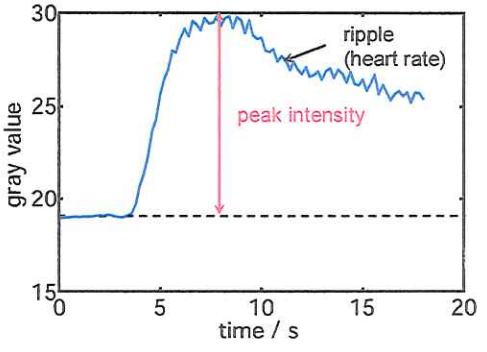

Fig. 1: Time-intensity curve showing the intensity enhancement and a cyclic intensity variation (ripple) that represents the heart rate.

RESULTS

As an example, images of a patient with an aneurysm are shown in the following. In the peak intensity image, the aneurysm appears in darker shades of gray than the major brain arteries (Fig. 2). The amplitude of the intensity variation ("ripple amplitude"), however, is higher in the aneurysm than in the arteries (Fig. 3). The ripple amplitude was determined by a spectral analysis so that it is a clear marker of pulsatility, i.e. of arterial flow. Note that the absence of such a ripple can either indicate very high flow rates, where the peak intensity image should be quite bright, or very slow flow, where it takes more than a heart cycle for the blood to pass the resolution cell. Inside the aneurysm, the phase wraps around twice indicating that the vortex inside the aneurysm rotates at approximately half the heart rate. Further studies, theoretical and practical, are necessary to determine useful settings of contrast agent concentration, frame rate, and transmit power for different applications.

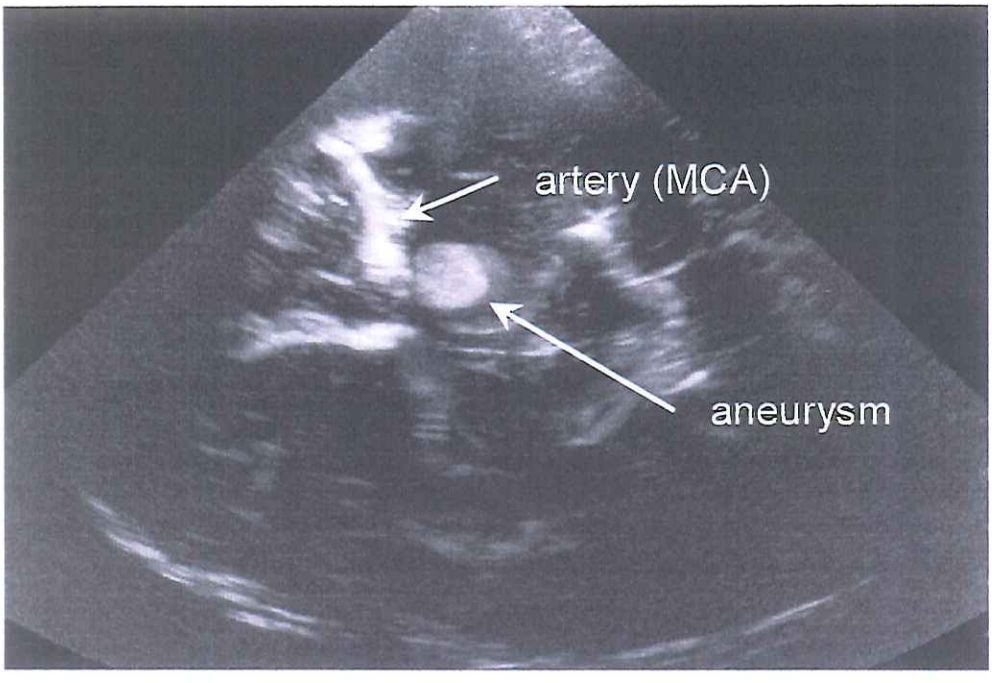

Fig. 2: Peak intensity image of a human brain in angiographic mode, 1 – 14 cm imaging depth.

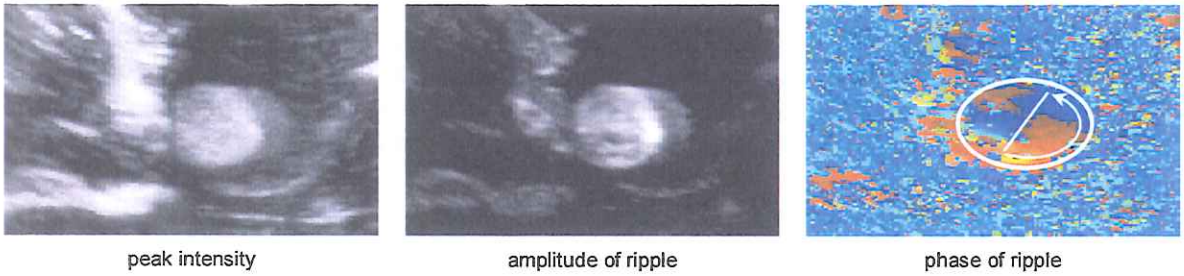

Fig. 3: Closeup view of the aneurysm. The arteries appear brighter than the aneurysm in the peak intensity image indicating that the flow rate is higher in the artery. The "amplitude of the ripple" image shows that the flow in the aneurysm is pulsatile (arterial). The phase image reveals that the vortex inside the aneurysm needs approximately two heart cycles for one rotation (dividing line inside the ellipse, blue and red correspond to $-\pi$ and π, respectively). The arrow indicates the rotation direction.

ASSESSMENT OF THE RENAL BLOOD FLOW IN PIGS USING CONTRAST-ENHANCED SONOGRAPHY

JM Correas[1] , T Messager[2], L Catel[3], A Broillet[2], O Hélénon[1], M Claudon[2]

1: Necker University Hospital, Paris, France 2 : Bracco Research SA, Genève, Suisse
3: CHU Brabois, Nancy, France

Purpose: To evaluate the renal blood flow using real time contrast-enhanced sonography (CEUS)before and after administration of Angiotensin II.

Methods: In 6 pigs, the left kidney was studied using the curvilinear transducer (C5-2) with low mechanical index pulse inversion imaging with the HDI5000 system (Philips US, Bothell, WA, USA). SonoVue® (Bracco, Milano, Italy) was infused in the femoral vein at 0.1 ml/kg/min during 7 minutes, before and after continuous injection of a vasoconstrictor agent, the Angiotensin II, at increasing dosage (0.016 – 0.033 – 0.05 ml/kg/min). The reperfusion kinetics was calculated using 4 Regions of Interest (ROIs) located in the anterior and posterior cortex, in the medulla and covering the whole kidney. The signal intensity (SI) was calculated in linear units using the HDILab sofware (Philips US, USA) by two independent observers and fitted to the following model: SI=A*(1-Exp(-Bt)). The relationship between the US parameter A*B was correlated to the true changes in the cortical and medullary blood flow evaluated using fluorosent microspheres administered into the aorta.

Results: The administration of Angiotensin resulted in a decrease in the true cortical blood flow (382 ml/min at baseline, and respectively 239 – 222 – 218 ml/min for the 3 dosages of Angiotensin, reduction of 33 to 42%), except for one animal who exhibited a paradoxical response. No significant change in the blood flow was found for the three Angiotensin dosages. The cortical blood flow calculated with CEUS was correlated to the reference measurements, for all ROIs (R2 from 0.89 to 0.92). The correlation between the two independent observers was high (R2= 0.98). However, CEUS overestimated the changes of the renal blood flow in an animal per animal analysis, attributed to the increased microbubble destruction in case of blood flow reduction.

Conclusion: CEUS might become a useful technique to evaluate the changes in the renal blood flow non invasively. New mathematical models are required to take into account the increase in microbubble destruction when the blood flow reduces.

ULTRASOUND CONTRAST AGENTS AND THE ROLE OF REACTIVE OXYGEN SPECIES IN SONOPORATION

L.J.M. Juffermans, P.A. Dijkmans, C. Visser, R.J.P. Musters, O. Kamp.

Department of Physiology and Cardiology, VU University Medical Center, Amsterdam, the Netherlands;Interuniversity Cardiology Institute of the Netherlands, Utrecht, the Netherlands.

Local gene and drug delivery through ultrasound contrast agents is a promising technique, and it is assumed that diagnostic ultrasound does not pose any danger to the patient. However, recent experimental studies show that there are indications for bioeffects induced by ultrasound in the absence and presence of contrast agents. These bioeffects may not always be as obvious as capillary rupture or cell necrosis, but rather may represent more subtle cellular and subcellular alterations caused by, e.g., a local rise in temperature (P.A. Dijkmans *et al.*, 2004). The generation of oxidative stress by diagnostic ultrasound, which already occurs in the absence of microbubbles – as has recently been shown by Basta *et al.* (2003) – is an example of such an important bioeffect. Free radical formation by ultrasound is due to inertial cavitation and depends strongly on its threshold acoustic frequencies. At physiological levels reactive oxygen species (ROS) are crucial second messengers in redox-related cell signaling and normal cell function. NO is an important regulator of endothelium-dependent vasodilatation, $O_2^{\cdot}$ and H_2O_2 mediate growth and differentiation of vascular smooth muscle cells. The generation of ROS may also play a role in the transient permeabilization of cell membranes by sonoporation. The exact mechanism(s) underlying sonoporation are still unknown. Deng *et al.* (2004) showed increased cell membrane permeability after ultrasound and microbubbles by the influx of calcium ions through transient 'holes' in the membrane, and not via calcium channels. Using a custom-made ultrasound application system on a real-time, so called multidimensional fluorescence microscope, we detected an elevation in intracellular ROS accumulation as well as an increase in intracellular calcium. We hypothesize that the ROS formed by cavitation enters the cell, oxidizes the phospholipid cell membrane and thereby permeabilizes the membrane allowing, e.g., the influx of calcium, as well as the uptake of macromolecules or genes for local drug and gene delivery.

DETECTION AND CHARACTERIZATION OF SPLENIC LESIONS – A PROSPECTIVE STUDY COMPARING CONTRAST HARMONIC IMAGING WITH COMPUTED TOMOGRAPHY OR MAGNETIC RESONANCE IMAGING

K. Schlottmann[1], U. Dorenbeck[2], J. Seitz[2], S. Feuerbach[2], A. Harsch[1], J. Schölmerich[1], G. Lock[3], F. Klebl[1]

[1]Department of Internal Medicine I, Interdisciplinary Department of Ultrasound, [2]Department of Radiology, University Hospital Regensburg and [3]Department of Internal Medicine, Albertinen Hospital Hamburg, Germany

Background:

Splenic lesions can be detected by B-mode sonography both, as incidentalomas or upon tumor staging. However, no reliable sonographic criteria discerning benign from malignant lesions are available. Preliminary data suggest that ultrasound contrast agents (UCA) allow for the detection and characterization of hepatic lesions with a sensitivity and specificity comparable to CT and MRI. In our study we evaluated whether UCA also help to detect and characterize splenic lesions.

Patients and Methods:

We included 46 patients (pts.) with splenic lesions which were detected at our hospital by any of the following three imaging modalities: sonography (US), contrast enhanced spiral computed tomography (CT) or magnetic resonance imaging (MRI) (November 2000 – May 2003). We used the Siemens Elegra ultrasound machine (Siemens, Isaquah, USA) at conventional B-mode, tissue harmonic imaging (THI) and contrast harmonic imaging (CHI). All patients were investigated with SHU508A (Schering, Germany), and from November 2001 with SHU508A and BR-1 (Bracco, Milan, Italy). CHI was compared either with CT or MRI. All US investigations were recorded on S-VHS and analyzed by KS and AH. Radiological images were analyzed by two experienced radiologists.

Results:

Lesion	US	CT	MRI
Hemangioma	6	3	0
Cyst	5	1	1
Infarction	4	2	1
Abscess	2	1	0
Echinococcus	0	1	0
Metastasis	7	6	1
Lymphoma	14	14	2
Undetermined	8	11	3
Total	**48**	**37**	**8**

The table represents lesions defined by US, CT and MRI. The diagnoses differed between the respective imaging techniques.

Concerning whether lesions were of benign or malignant nature, in 21 cases the diagnosis with CHI was concordant with the CT/MRI data. In 16 pts. diagnoses were not conclusive from all imaging techniques and in 11 pts. discordant diagnoses were made. Five out of 8 pts. from whom splenic histology was obtained

proved to be correct with CHI while 2 diagnoses were wrong and one was inconclusive. CT gave the right diagnoses in 3 cases while 5 diagnoses were wrong. SHU508A and BR-1 were comparable when malignant lesions were diagnosed. In benign lesions significant differences in contrast agent behavior between SHU508A and BR-1 were observed. CHI criteria for benign and malignant lesions could be defined. In terms of lesion detection, sensitivity for CT/MRT and CHI were comparable.

Conclusion: This is the first prospective study on CHI in the spleen. CHI is the only sonographic technique by which malignant splenic lesions can be distinguished from benign lesions in terms of UCA perfusion and uptake. Standard imaging techniques such as CT and MRI do not seem to be superior to B-mode US plus CHI in terms of detection and characterization of splenic lesions.

MICROBUBBLES POKING AND PRODDING LIVING CELLS

Annemieke van Wamel[1-2], Michel Versluis[3] and Nico de Jong[1-2-3]

1-Thoraxcentre, Erasmus MC, Rotterdam, The Netherlands
2-ICIN, Utrecht, The Netherlands
3- Dept. of Applied Physics, Physics of Fluids, University of Twente, Enschede, The Netherlands

Purpose: Ultrasound in combination with contrast microbubbles has been shown to alter the permeability of cell membranes. This permeabilization feature is used to design new drug delivery systems using ultrasound and contrast agents. Although the exact underlying mechanisms are still unknown, one hypothesis is that oscillating microbubbles cause cell deformation resulting in enhanced cell membrane permeability. In this paper we show the different actions of oscillating microbubbles on cultured cells under a microscope recorded with a fast framing camera at 10 million frames per second.

Method: Optical observations of microbubbles and cultured cells is possible through the use of a microscope mounted in front of the fast framing camera Brandaris128. The Brandaris128 is capable of recording a sequence of 128 images with a frame rate up to 25 million frames per second. Pig aorta endothelial cells were grown on the inside of an Opticell™ container. A diluted suspension of experimental lipid agents was added. Ultrasound exposure consisted of one to six bursts of 6 cycles at a frequency of 1 MHz and a negative pressure of 0.1 - 0.5 MPa. During ultrasound transmission, the interactions between BR14 microbubbles and cultured cells were recorded using a frame rate of 10 million frames per second.

Results: Cell deformation and partial-detachment as a result of vibrating microbubbles is studied. Cell deformation is quantified through measuring the displacement of the cells. Cell detachment is quantified by the retraction of the cell membrane after deformation. Microbubble vibration is quantified by measuring its initial, maximal, and minimal radii. We observed that, upon ultrasound arrival and microbubble oscillations, the cell membrane deforms up to a few micrometers in length as a result of the oscillation of the microbubble. The membrane deformation rate changes with the oscillation strength of the microbubble. During the insonification, changes in the cross-sectional distance of the cultured cells were observed due to microbubble vibrations.

Depending on the maximal vibrations of the microbubble and the distance between the microbubble and the cell, the displacement of the cells varied form 0 to 20% of the cell size. Multiple bursts can cause partial-detachment of cells depending on the amplitude and number of bursts.

Conclusion: This study reveals different actions of oscillating microbubbles on adherent cells. It is believed that next to partial detachment, perturbation of the oscillating microbubbles results in profound alterations in the cellular content. This study is the beginning of revealing the functional relationships that lie beyond the remote manipulation of cells and ultrasound microbubble induced permeabilization of the cell membrane.

DIRECT, REAL-TIME VISUALIZATION OF THE VASA VASORUM AND CAROTID PLAQUE NEOVASCULARIZATION IN PATIENTS: CORRELATION BETWEEN THE CONTRAST-ENHANCED IMAGES AND HISTOLOGY.

Steven Feinstein, Michael Davidson, Peter Meyer, Matt Feinstein, Rachel Neems, Marshall Goldin, John Dainauskas, and Paul Espinoza

Rush University Medical Center and Radiant Research, Chicago, Illinois

Background: The vasa vasorum network consists of a rich plexus of microvascular vessels found within the adventitial/media/intima tissues of arteries. Previous surgical-pathological reports and pre-clinical experimental studies noted the presence of these angiogenic vessels in association with clinical and experimental atherosclerosis. In addition, there is a increased prevalence of adventitial neovascularization compared to luminal neovascularization identified in patients with occlusive vascular diseases.

Using new applications of contrast-enhanced ultrasound exams, neovascularization found within the adventitial/media/intima regions of the carotid arteries can be directly visualized in real-time. These new data support the concept that the increased vascularity of the vulnerable plaque may be directly imaged using ultrasound and contrast-enhanced carotid imaging.

Objectives: The ongoing surgical validation study tests the hypothesis that contrast-enhanced, ultrasound imaging of the carotid artery plaque will correlate to the presence and degree of adventitial and plaque neovascularization in tissue specimens from patients with carotid atherosclerosis who underwent a carotid endartectomy.

It is anticipated that contrast-enhanced, ultrasound imaging could be used to asses the vulnerablilty of carotid plaques and consequently, provide a basis to monitor the therapeutic effectiveness based upon the regression/progression of neovascularization.

Our research involves a multi-disciplinary approach designed to assess the presence and degree of neovascularization observed in our patients at the time of carotid imaging. The neovascularization observed in the contrast-enhanced carotid artery images will be correlated to histo-pathology findings. Additional analyses include special vascular cellular staining and ex-vivo physiologic experiments designed to assess the presence of adventitial arteriogenesis.

Methods: Patients scheduled for an ultrasound carotid examination were asked to participate in an ongoing research study using an intravenous ultrasound contrast agent to: (1) enhance the

carotid artery lumen surfaces, (2) identify the anterior carotid IMT, (3) detect adventitial vasa vasorum. All patients were imaged using a contrast equipped vascular ultrasound probe and an they received an intravenous contrast agent. The initial pathologic studies included twenty-one (21) patient carotid examinations. All patients included in the study had a >50% stenosis. In addition, 5 patients have undergone a surgical carotid endarectomy. Subsequently, tissue plaque specimens were analyzed for neovascularization by histology/pathology using Hematoxylin and Eosin staining.

Neovascularization	patients	Statin	No Statin	Unknown
Limited	11	5	3	3
Moderate	5	2	0	3
Extensive	4	1	2	1
None	1	--	0	0
Total	21	8	5	7

Results: The vast majority (95%) of patients with a >50% carotid artery stenosis revealed the visual presence of vasa vasroum and plaque neovascularization in the carotid artery. Using a qualitative visual grading system (3=extensive, 2=moderate, 1=minimal) extensive neovasculature was observed in 4 patients, moderate neovasculature was observed in 5 patients, and minimal, was observed in the plaque of 11 patients. The four patients with extensive neovascularization revealed that 2 patients were not on statins; whereas, in the limited neovascularization group, 5 of 8 with known treatment profiles were on statins.

The histologic specimens of the 5 patients undergoing carotid endarterectomy revealed degrees of plaque neovascularization commensurate with the graded, non-invasive carotid ultrasound images.

Conclusion: Real-time, contrast-enhanced ultrasound visualization of the carotid artery adventitial vasa vasorum and plaque neovascularization is feasible. These initial contrast-enhanced ultrasound examinations of the human atherosclerotic carotid artery plaque appear to correlate with the histo-pathology findings. Therefore, a non-invasive technique used to quantitate carotid artery neovascularization may identify plaque vulnerability and ultimately, provide a method to assess therapy for the treatment of atherosclerosis.

GAS-FILLED MICROBUBBLE CONTRAST AGENTS: SHELL BEHAVIOR IN THE COMPRESSION AND RAREFACTION PRESSURE FIELD.

A.L. Klibanov, J.J. Rychak, M.S. Hughes, G.L. Cantrell, J.H. Wible, Jr.

Cardiovascular Division, Cardiovascular Imaging Center, Cardiovascular Research Center, Department of Biomedical Engineering, University of Virginia, Charlottesville VA, and Mallinckrodt Inc., St. Louis, MO.

Ultrasound scattering by gas-filled microbubbles is strongly dependent on the properties of the microbubble shell coating. Shell behavior in a pressure field has not been previously reported. The microbubble coating has been usually assumed to deform elastically. This study was undertaken to observe the behavior of the shell of the microbubbles subjected to hydrostatic compression or partial rarefaction.

Microbubbles were prepared by self-assembly of a lipid monolayer on at the gas-aqueous phase interface, as gas was dispersed in the aqueous saline micellar mixture by probe-type sonicator. Poorly soluble decafluorobutane gas was used as the bubble core. The lipid shell consisted of distearoyl phosphatidylcholine and grafted PEG stearate with a small amount of a hydrophobic fluorescent probe (DiO or DiI) or biotin-PEG-lipid added when necessary. Such microbubbles possess good ultrasound scattering characteristics as well as extended stability on storage (many months, up to several years) and reasonable lifespan in the bloodstream (up to tens of minutes). Alternatively, commercially available Optison® microbubbles that have human albumin protein shell were tested. Albumin microbubbles were labeled by covalent attachment of FITC to the amino groups of albumin.

Deformation of microbubbles and the behavior of the lipid monolayer shell or denatured protein shell in the pressure field were studied by fluorescence microscopy. Microbubbles were placed in a sealed transparent chamber filled with degassed saline, outfitted with a Luer port connected to a syringe and a manometer; alternatively, a thin rectangular glass capillary tubing sealed on one side was used. A chamber was installed on the stage of the epi-illumination fluorescence microscope. During compression, excess microbubble lipid shell formed folds (likely, bilayer structures) that extended into the surrounding aqueous medium. At high pressure,

when gas was lost from the bubbles completely, flat lipid layers frequently collapsed into cochlear cylinders. Albumin shells after compression also formed wrinkled projections; however, formation of cochlear structures was not observed.

On application of reduced pressure bubble expansion and lipid shell cracking resulted. Areas of lipid coating separated by the areas of uncoated gas-water interface lacking fluorescent label were observed. During exposure to MHz ultrasound, generated by a medical imaging system transducer array, lateral microstreaming convection of the microbubble shell fragments was noted. The lateral movement of the fluorescent streptavidin-coated nanoparticles attached to the microbubble shell also occurred. This lateral motion is similar to bulk microstreaming effects reported for the bulk aqueous phase in the vicinity of the insonated bubbles.

Overall, microbubble shell in the pressure field demonstrates behavior that is far from the classical elastic description.

ULTRASOUND EXPOSURE CAN INCREASE THE MEMBRANE PERMEABILITY OF HUMAN NEUTROPHIL GRANULOCYTES CONTAINING MICROBUBBLES WITHOUT CAUSING COMPLETE CELL DESTRUCTION

Grigorios Korosoglou[1], Stefan E. Hardt[1], Raffi Bekeredjian[1], Juergen Jenne[2], Matthias Kontantin[1], Ioana Balden[1], Marco Hagenmueller[1], Juergen Debus[2], Hugo A. Katus[1], Helmut F. Kuecherer[1]

[1] Department of Cardiology, University of Heidelberg, Heidelberg, Germany
[2] German Cancer Research Center (DKFZ), Heidelberg, Germany

Objective: Activated polymorphonuclear neutrophil granulocytes (PMN) can bind and subsequently phagocytose albumin- and lipid-microbubbles used as ultrasound contrast agents. The purpose of the present study was to assess insonation effects on cell membrane integrity and metabolic activity of activated PMN. Furthermore, we investigated whether there is an acoustic threshold at which insonation of PMN results in increase of membrane permeability without resulting in complete cell destruction.

Methods: PMN isolated from healthy volunteers were activated with phorbol-myristate-acetate (PMA) for 15 min to allow phagocytosis of albumin- and lipid-microbubbles and were subsequently exposed to ultrasound with a mechanical index between 0.1 and 1.6. Apoptosis, loss of membrane integrity and formation of cell fragments were evaluated by double staining with annexin V and propidium iodide, using flow cytometry. Neutrophil superoxide anion generation was measured photometrical.

Results: Insonation of activated PMN in the presence of both albumin- and lipid-microbubbles amplified apoptosis and induced loss of membrane integrity and complete cell destruction with increasing acoustic pressures. The bioeffects observed by insonation with high mechanical indexes (0.8 to 1.6) and particularly the formation of cell fragments, were significantly more pronounced in the presence of albumin-microbubbles. Insonation in the presence of lipid-microbubbles induced loss of cell membrane integrity but caused significantly less complete cell destruction, leaving the metabolic activity of activated PMN uninfluenced.

Conclusions: Both albumin- and lipid-microbubbles induce apoptosis and membrane injury during insonation of activated PMN. However, insonation in the presence of lipid-microbubbles seems to influence cell viability to a smaller extent, so that more cells survive the ultrasound treatment. This could be an advantage in the setting of ultrasound-guided local drug delivery, where increased membrane permeability may allow bioactive substances to enter cells, without causing cell destruction.

PHYSIOLOGY OF VASA VASORUM RELATED TO ATHEROSCLEROSIS

R.Krams[1], D.E. Goertz[1,2], F.J. ten Cate[1], N. De Jong[1,2,3], H. Duckers[1], C.J. Slager[1] and A.F.W. van der Steen[1,2]

1- Erasmus MC, Rotterdam the Netherlands, 2- Interuniversity Cardiology Institute of the Netherlands, 3- Physics of Fluids, Twente University

Physiology of vasa vasorum: The vasa vasorum has been the subject of considerable interest for decades. Early pathological studies determined the morphology of the vasa vasorum and tested variation of this morphology under several conditions. From these studies two classification schemes have been derived. Schoenberger and Muller described in the seventies a morphological description based upon the origin of vasa vasorum: external vasa vasorum (originating from a side branch), internal vasa vasorum (originating from the lumen) and venous vasa vasorum. Another study divided the vasa vasorum in first order, running in parallel to the vessel, and in second order running circumferentially. As the Schoenberger and Muller classification offers more possibilities we will adopt this scheme during this presentation. A recent series of experiments performed with μCT indicated that the vasa vasorum in young animals consisted of a tree like network of end-arteries, similar to the microcirculation of the heart. All three vasa vasorum networks exhibited this tree like network. A detailed morphological and biophysical analysis indicated that the tree was not optimised in terms of intraluminal energy transfer. Non-optimised conditions leads to larger pressure drops at physiological flows, making these vascular trees more susceptible to variations in tissue pressure, i.e. to pressure outside the vasa vasorum vessels. Indeed increments of tissue pressure reduce vasa vasorum flow to the vessel wall, a mechanism of importance for hypertension (see below).

The presence of vasa vasorum is likely to be related to nutritional needs. A comparison between species indicates that vasa vasorum of the aorta exists in vessels with wall thickness larger than 0.5 mm or larger than 29 lamellae. More recent studies showed that for coronaries the wall thickness was smaller (0.35 mm) indicating that wall thickness is not the only determinant of vasa vasorum. Functional studies of this network showed that the vessels responded with vasodilatation after adenosine and vasoconstriction after stimulation of the nervous system or known vasoconstrictors. Regulation of vascular tone adds to the possibility to deliver nutrients to

the vessel wall. Other studies indicate that diffusion from the vasa vasorum is also necessary for nourishment of the medial layer of the aorta and the outer half of coronary arteries. Diffusion of solutes is determined by the properties of the solute, the flow through the bed and the surface area offered by the bed. The latter is a function of the capillaries, while flow is regulated by arterioles. A recent study in young animals using indicator dyes and μCT images indicates a distribution of the dye within 10 seconds after injection over the vessel wall with early peaks located at the inner half of the vessel wall and at the outer half of the vessel wall. Measurement of the flux of solutes over a period of 30 seconds post-injection indicated movement of solutes from the vessel lumen to adventitial layer, probably due to drainage of the solutes by the venous vasa vasorum. If these regulation mechanism are exhausted remodelling and growth of vasa vasorum is induced. Indeed, during normal body growth radius of vasa vasorum vessels increases in concert with their vessel area in different species and in different vessels. In summary, the functional and anatomical studies indicate that i) the vasa vasorum behaves as a normal vascular bed, with a dichotomous vascular tree and physiological diameter control, ii) the size of the vascular tree is determined by the wall thickness and probably hypoxic conditions in the medial layer, iii) the tree is not perfectly optimised in terms of energy dissipation making it more susceptible to environmental factors, and iv) supply and drainage of solutes and particles (see below) are determined by different networks.

Pathophysiology of vasa vasorum: Atherosclerosis has been considered a response to injury disease, whereby the endothelial layer plays a pivotal role. From the above it is clear that nourishment of blood vessels occurs both through the lumen-vessel wall endothelial layer and through the adventitial vasa vasorum endothelial layer. It is therefore of interest to note that after short periods of hypercholesteremia (4 weeks) vasa vasorum density and vascular area increases in the absence of real plaques. This increase in density precedes lumen-vessel wall endothelial dysfunction. This study indicates a uncoupling between vasa vasorum growth and hypoxia, as found in normal conditions. Long-term experiments with hypercholestermia indicate that vasa vasorum area increases further, but now in concert with plaque thickness. In addition to the increase in morphology, flow increases 5 fold and permeability approximately doubles. A density value based upon morphology and flow remained constant despite increments in wall thickness. These experimental studies may be interpreted that increments in plaque thickness stimulate vasa vasorum growth, or that increments in vasa vasorum aggravate atherosclerosis. Evidence for the former resides in the constancy of vasa vasorum despite large variations in plaque thickness. Evidence for the latter stems from a series of experiments where modulation of vasa vasorum

density, by either knockout studies or drug treatments, affects plaque growth independent of cholesterol levels. Hypertension, another risk factor of atherosclerosis independently affects the vasa vasorum. The combination of risk factors has a tendency for a reduction in vasa vasorum. Whether this implies that a reduction of inflammatory stimuli occurs or a decreased outward flux occurs with a reduction in vasa vasorum flow is presently unknown.

Atherosclerosis is nowadays considered an inflammatory disease and accumulation of macrophages have been coupled to plaque vulnerability. Recent pathological studies in patient blood vessels indicate a correlation between inflammation and neo-vascularization. Strong correlation between macrophage accumulation and neo vascularization has been measured. Although these studies are rather descriptive in nature, the experimental studies cited above indicate that neo-vascularization aggravates inflammation and may be an additional risk factor for (vulnerable) plaque development. To note is that statins affect vasa vasorum independent of cholesterol levels providing a therapy for this novel risk factor.

In summary, hypercholesteremia and hypertension both affect vasa vasorum growth and plaque progression. The question whether vasa vasorum follows plaque progression or that vasa vasorum growth induces plaque growth cannot be answered at this moment. Evidence exists for both theories, but recent evidence is more in favour the latter theory. Because of this and the fact that neo-vascularization has been associated with large and vulnerable plaques it may be considered a risk factor and therefore imaging strategies for determination of vasa vasorum function is of importance.

A reference list is available on request.

ARTERIAL NEOVASCULARIZATION AND INFLAMMATION IN PATIENTS WITH SYMPTOMATIC ATHEROSCLEROSIS

Barbara C. Biedermann

Department of Medicine, University Hospital Bruderholz, 4101 Bruderholz, Switzerland. E-mail: barbara.biedermann@unibas.ch

Background: Atherosclerosis is complicated by cardiovascular events such as myocardial infarction, stroke or peripheral arterial occlusive disease. Inflammation and pathologic neovascularization are accused to precipitate plaque rupture or erosion, both causes of arterial thrombosis and cardiovascular events. We tested the hypothesis that arterial inflammation and angiogenic events are increased throughout the arterial tree in vulnerable patients, i.e. in patients who suffered from cardiovascular events compared with patients who never suffered from complications of atherosclerosis.

Methods and Results: In a *postmortem* study, we quantified the inflammatory infiltrate and the microvascular network in the arterial wall of the iliac, the carotid and the renal artery. Tissue microarray technology was adapted to investigate full-thickness arterial sectors. Twenty-two patients with symptomatic atherosclerosis were compared with twenty-seven patients who never had suffered from any cardiovascular event during their lifetime. The absolute intimal macrophage content was 2 to 4-fold higher in vulnerable patients at all three arterial sites analyzed ($P<0.05$). Patients with symptomatic atherosclerosis had a denser network of vasa vasorum than patients with asymptomatic disease (33±2 vs 25±2 adventitial microvessels per mm^2, $P=0.008$). Hyperplasia of vasa vasorum was an early and macrophage infiltration a late sign of symptomatic atherosclerosis.

Conclusions: High intimal macrophage content and a hyperplastic network of vasa vasorum characterize vulnerable patients suffering from symptomatic atherosclerosis. These changes are uniformly present in different arterial beds and support the concept of symptomatic atherosclerosis as a pan-arterial disease.

MYOCARDIAL BLOOD FLOW AS ESTIMATED WITH REAL-TIME MYOCARDIAL CONTRAST ECHOCARDIOGRAPHY IN HEALTHY VOLUNTEERS CORRELATES WITH POSITRON EMISSION TOMOGRAPHY

P.A.Dijkmans[1], P.Knaapen[1], E. Aiazian[1], C.A. Visser[1], A.A. Lammertsma[2], F.C. Visser[1], O.Kamp[1]

Department of Cardiology[1] and Nuclear Medicine and PET Research[2], VU University Medical Center, Amsterdam, the Netherlands

Purpose Intravenous myocardial contrast echocardiography (ivMCE) is becoming an increasingly valuable technique that creates the opportunity of measuring myocardial perfusion. Purpose of this study was to assess the ability of real-time ivMCE to quantify myocardial blood flow (MBF) and to compare ivMCE with MBF as measured with positron emission tomography (PET).

Methods Sixteen healthy volunteers underwent ivMCE using the ATL 5000 with power pulse inversion and continuous infusion of Sonovue® microbubbles at rest and during adenosine stress. Microbubble destruction was achieved with a burst of high energy ultrasound, followed by imaging of contrast replenisment with low energy ultrasound. Using the HDI lab, regions of interest were drawn and time intensity curves were calculated and fitted to a mono-exponential function. MBF was estimated with ivMCE as the product of the slope β and the maximal intensity A of the replenishment curve and was determined for the vascular territory of the left anterior descending coronary artery (LAD), the right coronary artery (RCA) and the circumflex artery (CX). MBF (mL/min/mL) was measured with PET using oxygen labeled water ($H_2{}^{15}O$) at rest and during adenosine stress.

Results Significant overall correlations were found between MBF as measured by PET and $A*\beta$ as measured by ivMCE in the LAD ($r=0.86$, $p<0.01$) (Fig), the RCA ($r=0.66$, $p<0.01$) and the CX ($r=0.72$, $p<0.01$) territories.

Conclusion MBF as estimated by ivMCE in healthy volunteers correlates overall with PET within vascular territories.

DEVELOPMENT OF A NEW STABLE ULTRASOUND CONTRAST AGENT

Erol.Kurtisovski[1,4], Emilia Pisani[2], Nicolas Tsapis[2], Elias Fattal[2] Belfor Galaz[3], Jean Jacques Ammann[3], Jean Yves Le Huerou[4] and Wladimir Urbach[1,4].

1) Laboratoire de Physique Statistique de l'ENS, CNRS UMR 8550, F-75005 Paris, France
2) Laboratoire de Pharmacie Galénique, UMR CNRS 8612, F-92296 Châtenay-Malabry
3) Depto. Física, Universidad de Santiago de Chile, Santiago, Chile
4) Laboratoire d'Imagerie Paramétrique, CNRS UMR 7623, F-75006 Paris, France

Commercial ultrasound contrast agents (USCA) are polydisperse and usually suffer from a poor stability with time in solution. The production of a more stable and monodisperse USCA would lead to a more widespread and systematic clinical use, and take full benefits of harmonic imaging, which enhance considerably the signal to noise ratio.

We have developed a product candidate for ultrasound contrast agent based on PLGA polymer. These particles are obtained by freeze-drying double-emulsion techniques. This process allows to remove water from the internal cavity of the particle, replacing it by air. Particles' size can be adjusted between 1 and 5 microns and confocal microscopy shows the presence of air bubbles entrapped within the polymer matrix of the particles.

In vitro measurements performed in pulse-echo mode demonstrate that encapsulated air bubbles produce a significant backscattering of an ultrasounds burst. Moreover, RF signals, obtained on samples from the same batch after a few hours, do not exhibit significant alteration.

The RF measurements were confirmed by in vitro echographic imaging on a synthetic tube filled with a USCA and immersed in a water tank. The presence of USCA particles in the tube produces a clear echographic signal delimited by the tube wall.

A NEW HIGH INTENSITY FOCUSED ULTRASOUND (HIFU) SYSTEM FOR TUMOR TREATMENT AND REAL-TIME CONTROL BY DOPPLER SONOGRAPHY. EX VIVO AND IN VIVO INVESTIGATIONS

V. Rouffiac, JS. Duret, P. Opolon, P. Péronneau, A. Roche

N. Lassau -Institut Gustave Roussy-Villejuif-France.

Purposes: First objective was to define optimal settings (emitted power, treatment time, spatial displacement of HIFU shots) of a new HIFU system to generate necrosis of a 1 cm^3 liver sample. Second objective was to apply these settings on five melanomas grafted onto mice and control tumor destruction by ultrasound perfusion software after contrast agent injection and by necrosis estimated in histology.

Materials and methods: The HIFU prototype system is composed of a 9 MHz linear probe (Toshiba®) placed at the center of a 2.25 MHz mono-element transducer (Imasonic®) focusing at 6.5 cm. Position of the focal point inside the targeted organ can be monitored, in B-mode, thanks to the 9 MHz probe connected to an Aplio sonograph. A sinusoïdal signal is generated by a function generator (B&K Precision®) and amplified (EMV®) before being transmitted to the 2.25 MHz transducer. At fixed treatment time (60 s), the emitted power was increased from an arbitrary value until generating a lesion of 1.5 cm of maximal diameter on liver samples. At this maximal power, treatment time was decreased from 60 s until generating a lesion of less than 1 cm of maximal diameter. For fixed maximal power and minimal treatment time, ten lesions were created to test reproducibility of the system. Several shooting strategies were tested to necrose of a 1cm^3 volume. Optimal settings were then applied on five melanomas grafted onto mice. Tumor vascularization and perfusion were quantified before and immediately after HIFU treatment by contrast uptake using the Vascular Recognition Imaging (VRI) software (Aplio, Toshiba®) after Sonovue (Bracco®) injection. Tumor were reviewed in histology for necrosis quantification.

Results: Optimal settings were found for 150 Volts peak to peak of emitted power applied during 20 s (50 lesions at all). Ten ex vivo lesions were created at these settings and mean dimensions of lesions were 9.78 (±0.66) * 2.11 (±0.33) mm^2. A squaring of nine shooting points separated by 4

mm was necessary to necrose a 1 cm^2 surface. Two minutes of resting were applied between each dot line to avoid coalescence phenomena between successive lesions. For the five in vivo melanomas, reduction fo contrast uptake quantified in VRI after HIFU treatment was significantly correlated with histological percent of necrosis ($p=0.01$).

Conclusion: We have demonstrated the therapeutic potential of a new HIFU system with real time follow-up and immediate control of treatment by ultrasound perfusion software using contrast agent. Series of larger number of in vivo investigations are now conducted based on raw data recording using CHI-Q quantification software in order to optimize HIFU strategy and to validate the treatment by a temporal follow-up after HIFU before first human investigations.

THROMBUS-TARGETING ULTRASOUND CONTRAST AGENT

Hong-mei Xia, Yun-hua Gao, Ai-na Bian, Ping Liu, Kai-bin Tan, Zheng Liu

Department of Ultrasonic Diagnosis, Xinqiao Hospital, the Third Military Medical University, Chongqing, China

This study was designed to prepare thrombus-targeting ultrasound contrast agent and to investigate the targeting ability to fresh blood clot in vitro and in vivo.

Methods: Fluorescence labeling thrombus-specific peptides, directed to the activated GPIIBIIIA receptor of platelets was attached to the surface of albumin-coated perfluorocarbon microbubbles. In vitro study, the targeting microbubbles were added to fresh human blood clots and the conjugation ability was observed under light and fluorescence microscope after 30 minutes. In vivo study, non-blocked fresh thrombi were made by $FeCl_3$ in abdominal aorta of rabbit and then the targeting ability was assessed by second harmonic imaging and intravenous injection of the targeting microbubbles. The plain albumin microbubbles were used as the controls.

Results: Targeted microbubbles with the binding of thrombus-specific peptides were positive and gave out shining bright yellow-green fluorescence in immunofluorescent assay. While in the control group, the lack of fluorescence demonstrated a poor bubbles specific binding. In vitro study, massive targeted microbubbles flocked around and within the fresh blood clots under microscope, while in the control groups, few microbubbles were found. In vivo study, the targeting microbubbles injection significantly enhanced the thrombus ultrasound imaging than that of the control bubbles. The clots were generally difficult or impossible to detect at baseline, yielding a vivid post contrast imaging.

A NOVEL INTEGRATED SYSTEM FOR REAL-TIME ACOUSTICAL INVESTIGATIONS ON MICROBUBBLES

Francesco Guidi, Fabio Nicchi, Rik Vos and Piero Tortoli

University of Florence, via Santa Marta 3, 50139 Firenze, Italy

Background - The investigation of microbubble behavior in acoustic fields is important for an increasing number of diagnostic and therapeutic medical applications. Phenomena like linear or non linear oscillations, translation, coalescence, rupture, sonic cracking and jetting can be involved. The observation and analysis of these phenomena are usually based on the use of a cumbersome bank of general purpose instruments, such as waveform generators, power amplifiers, oscilloscopes and/or high-speed cameras.

Method - This paper presents the development and application of a new highly integrated system dedicated to the study of interactions between ultrasound and microbubbles. The system, consisting of a single electronic board connected to a PC through a standard USB interface, can be used in association with single-element transducers working over a wide range of possible frequencies. The design specifications have been addressed to obtain a flexible and accurate control of all acoustic parameters that may influence the bubble behavior. The parameters of the transmitted signal (amplitude, shape, frequency, phase, length and PRF) can be arbitrarily fixed. Special pulse sequences, where any of the above parameters are cyclically changed, may be generated to check the response of each bubble to different insonation conditions. The system includes facilities for allowing the storage of raw echoes received from the microbubbles.

Experiments - The system has been used in experimental tests addressed to investigate the behavior of single bubbles in full populations of thermoplastic microballoons and BR14®, diluted in water at low concentrations. The behavior of individual scatterers was observed in real-time on the PC monitor through both a multigate Doppler display and a standard M-mode display. In the latter, each microbubble generated a distinct trace, whose slope and brightness depended on transmission parameters as well as on the bubble size and composition. Each trace was also markedly influenced by the local acoustic pressure. In particular, rapid accelerations were observed in the focal region, where radiation force is highest. By transmitting a sequence of short

pulses whose frequency was changed between 2 MHz and 4 MHz in steps of 125 kHz, a corresponding change in the scattering cross-section and velocity of each bubble was recorded. Some "abnormal" traces appearing at relatively high acoustic pressures have also been observed. They showed either an abrupt stop or, more occasionally, sudden slope and intensity changes (see the following figure). In all cases such phenomena coincided with the appearance of wideband noise in the Doppler spectrum estimated from the corresponding echoes. Such trace changes seemed to be produced by the microbubble destruction or other alterations of their physical structure due to insonation.

Conclusion - A novel PC-based system is proposed as a flexible research tool for microbubble experimental tests. Its preliminary application in a simple experimental set-up allows interesting phenomena like bubble translation and rupture to be thoroughly investigated. Comparison of experimental data to an appropriate simulation model of bubble translation could be used to estimate the initial diameter of each bubble.

Acknowledgments - This work has been supported by the European Union (UMEDS Project - grant # QLG1-CT-2002-01518), and by the Italian Ministry of Education, University and Research (COFIN 2002).

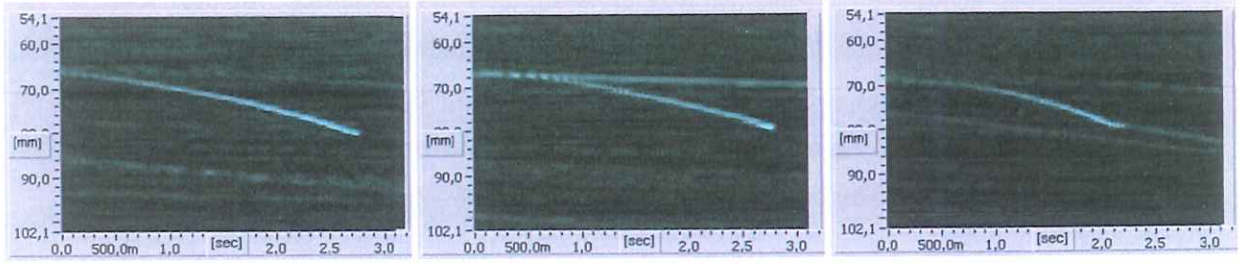

M-mode display of echo-signals received from thermoplastic microbubbles insonified at 3 MHz with four-cycle ultrasound bursts produced by a single element transducer focused at 80 mm. The peak pressure in the focal region was about 1 MPa. The three examples shown from left to right seem to correspond to three different rupture mechanisms.

CONTRAST PULSE SEQUENCE IMAGING FOR THE CHARACTERIZATION OF RENAL TUMOURS

Margot H. Wink, Jean J.M.C.H. de la Rosette, M. Pilar Laguna, Brunolf W. Lagerveld, Hessel Wijkstra

Academic Medical Center,Department of Urology (G4-105.1), Meibergdreef 9, 1105 AZ AMSTERDAM ZO, The Netherlands

Introduction: Contrast Pulse Sequencing (CPS) is a technique that improves agent-to-tissue specificity in contrast enhanced ultrasound. It recognizes the nonlinear fundamental responses and the higher order harmonics reflected by the contrast agent, by means of transmitting a sequence of pulses with different amplitude and/or phase. The reflections of the pulses are summed in such a way that tissue components are cancelled out, whereas nonlinear contrast signals add to form a stronger signal. This technology thus enables real time simultaneous viewing of tissue-only as well as contrast-only images using a low mechanical index.
Renal tumours are characterized based on imaging only, and are often detected coincidentally on abdominal ultrasound. The gold standard in the detection of malignant renal masses is contrast enhanced CT, based on which a patient will or will not undergo surgery.
Purpose of this pilot study was to investigate whether contrast enhanced ultrasound using CPS technique is able to substitute CT scan in selected cases in the diagnostic process.

Materials and Methods: In this pilot study, 18 patients, known with 20 renal masses diagnosed either on CT or ultrasound, were investigated using contrast enhanced ultrasound by one urologist and researcher. A Siemens Sequoia ultrasound machine with Cadence CPS technology and different abdominal probes was used. After localizing the renal mass using greyscale ultrasound (US), patients received a maximum of 2 boluses of 2,4 ml Sonovue (Bracco) intravenously. Clips were stored digitally for off line evaluation by two independent urologists.

Results: CPS images were subjectively of high quality and the ability to see greyscale and contrast-only images simultaneously was of vast clinical value. All but one lesion, as seen on CT, could be identified. Contrast arrived in the kidney after approximately 15 seconds and evaluation was possible for several minutes.
Two independent urologists retrospectively evaluated the clips and diagnosed the lesions based on CPS and greyscale images. The first identified all visible malignant lesions (14/14) and all

definite benign lesions (2 simple cysts, 1 angiomyolipoma). The second urologist correctly diagnosed 2/3 benign and 6/14 malignant masses.

The diagnosis of one mass was unclear on CT as well as contrast enhanced ultrasound, with a differential diagnosis of an abscess or a renal cell cancer. Pathology showed a necrotic transitional cell carcinoma in this kidney. The last patient had a complex cyst diagnosed on US, which proved to be a haemorrhage inside the cyst on CT. Because there was no contrast enhancement inside the cyst using CPS, this diagnosis could be made using contrast enhanced US without difficulty (figure 1).

Figure 1
CPS Imaging of a hemorrhagic renal cyst. On the right side the tissue- only, on the left the contrast-only image.

Conclusions: Contrast enhanced ultrasound using CPS imaging is a promising diagnostic tool in the characterization of renal masses and the ability to view contrast-only and greyscale images at the same time is of clinical importance. This pilot indicates that at least a significant proportion of renal masses can be diagnosed using CPS CE-US. It has the potential to substitute routine use of CT in the diagnosis of a renal mass, reserving this CT investigation for selected cases. An extended clinical study is necessary to determine the exact place of CE-US in the diagnostic process.

Acknowledgement: This research was supported by Siemens Medical and Altana Pharma

THE ENHANCEMENT PATTERN OF ATYPICAL LIVER HAEMANGIOMA WITH CONTRAST-ENHANCED ULTRASOUND

Ying Dai, Min-Hua Chen, Kun Yan, Wei Wu, Zhi-Hui Fan, Wei Yang, Shan-Shan Yin

Department of Ultrasound, School of Oncology, Peking University, China

Purpose: To investigate the enhancement pattern of atypical liver haemangioma under complex liver background with contrast-enhanced ultrasound (CEUS).

Methods: From March to Sept. 2004, 352 cases with unconfirmed focal liver lesions underwent CEUS. Of them, thirty-nine cases with forty-nine liver haemangiomas were retrospectively reviewed. Twenty-seven of these cases (69.2%) accompanied with fatty liver or cirrhosis or extrahepatic malignant tumors and the other 12 cases presented an atypical pattern on conventional ultrasound. The final diagnosis was obtained by contrast-enhanced CT, MRI, nuclear medicine or biopsy pathology. Contrast agent SonoVue and Contrast Tuned Imaging (CnTI) technique were used in this study.

Results: The 49 liver haemangiomas presented four enhancement patterns after CEUS. Patten I: twenty-six lesions enhanced in a pattern of thin ring with peripheral nodular and centripetal fill-in. Pattern II: fifteen lesions in a pattern of thick ring and centripetal fill-in. Pattern III: six lesions enhanced slightly and slowly or presented no obvious enhancement. Pattern IV: two lesions enhanced homogeneously. Six lesions of Pattern II and two lesions of Pattern IV washed out at the late phase. Before CEUS, only 2 lesions (4.0%) were diagnosed as liver haemangiomas. After CEUS, 35 lesions (71.4%) of Pattern I and II were diagnosed as liver haemangiomas, 6 lesions of Pattern III and 4 of Pattern II as possible benign tumors. Two lesions of Pattern IV were still unknown after CEUS and the other 2 lesions of Pattern II were misdiagnosed as malignancies due to the early wash out. Of the 14 lesions which were not diagnosed accurately by CEUS, 11 (78.6%) were less than 3 cm in size. The possible reason contributing to the atypical enhancement patterns was the small vascular size in small haemangimas.

Conclusion: Identification of the different enhancement patterns of liver haemangiomas could improve the diagnostic ability of CEUS. But when the lesions is small or presented atypical enhancement patterns, it is difficult to be diagnosed and still required enhanced CT or biopsy especially for lesions washed out at the late phase.

Key words: contrast agent, ultrasound, liver haemangioma, enhancement pattern

THE ROLE OF CONTRAST-ENHANCED ULTRASOUND IN PERCUTANEOUS LIVER BIOPSY OF FOCAL LIVER LESIONS TO INCREASE DIAGNOSIS RATE

Wei Wu, Min-Hua Chen, Shan-Shan Yin, Kun Yan, Ying Dai, Zhi-Hui Fan, Ling Huo, Ji-You Li

Department of Ultrasound, School of Oncology, Peking University, China

Purpose: To evaluate the clinical utility of contrast-enhanced ultrasound in percutaneous liver biopsy.

Methods: One hundred and eighty-six patients with unconfirmed focal liver lesions were randomly separated into two groups, CEUS group and US group. In CEUS group, 79 patients with 129 lesions underwent biopsy directed by real time gray contrast□enhanced ultrasound (CEUS) using contrast agent SonoVue ® (Bracco, Italy). In US group, 107 patients with 143 lesions underwent biopsy guided by conventional ultrasound (US). There was no statistically significant difference in the size range between CEUS group and US group (mean size 3.1cm in CEUS and 3.2cm in US). There were 68 (25.0%, 61 cases) minute malignant lesions with the sizes of ≤2.0cm in our study, 12.9% in CEUS group and 12.1% in US group. The biopsies were performed by 21 gauge or 18 gauge needles. Adequate specimens obtained for pathologic diagnoses meant successful biopsy. The definite diagnosis was made by combined the pathologic diagnosis of biopsy with the results of contrast-enhanced CT, MRI, Angiography, serum alpha-fetoprotein (AFP) or over 6 months clinical follow-up. The biopsy results of two groups were analyzed.

Results: There was no statistically significant difference in biopsy times between CEUS group and US group, but only one time biopsy in CEUS group was much higher than US group (p=0.0341). The biopsy successful rate and accurate diagnosis rate in CEUS group (n=129) were 98.4%□n=127□and 95.3%□n=123□respectively, and were 92.3%□n=132□and 87.4%□n=125□respectively in US group (n=143)(p=0.0411 and p=0.0400 respectively). The accurate diagnosis rate of malignant lesions with the sizes of ≤2.0cm in CEUS group was higher than those in US group (p=0.0479).There were statistically significant differences in the biopsy successful rate and accurate diagnosis rate between CEUS group and US group. In addition, 14 of

15 false negative lesions (13.9%) of malignant lesions in US group were obtained repeated biopsy directed by CEUS. Fourteen lesions of 15 lesions got definite diagnoses finally. Among them there were 12 lesions ≤2.0cm .No major complications occurred in our study except one case of pneumothorax occurred in US group.

Conclusion: Biopsy directed by CEUS is more accurate in location and diagnosis of malignant lesions and minute tumors, which will increase significantly biopsy's successful rate and accurate diagnosis rate and decrease the false negative rate. The clinical application of CEUS should be appreciated.

Key Words: Ultrasonography, Percutaneous, Biopsy, Contrast-enhanced Ultrasound, Liver tumors

AUTOMATIC IMAGE REGISTRATION SYSTEM FOR ULTRASOUND CONTRAST AGENT QUANTIFICATION.

Edward A. Gardner[1], Thilaka S. Sumanaweera[1], Michael N. Woelmer[1], Robert W. Steins[1], Edward Leen[2]

Ultrasound Division, Siemens Medical Solutions, Mountain View, California, U.S.A[1], Glasgow Royal Infirmary, Glasgow U.K[2]

Abstract: An automatic image registration system has been developed for an ultrasound system (Siemens Sequoia ™) to compensate for motion due to patient breathing and inadvertent probe movements in radiology and cardiology applications of contrast agent imaging. Automatic motion compensation is critical for contrast quantification because the time required for manual alignment restricts the clinical adoption of this technique. Two registration methods have been developed: rigid body and warping. Rigid body registration ignores deformation of the tissue from one frame to another and provides a robust alignment method. Warping deforms the images to match the master image in all points in the image and can more precisely compensate for motion.

Analysis of the effectiveness of the warping method was made using image sequences from fourteen patients with focal hepatic liver tumors. A destruction-wash-in technique was used to acquire the contrast enhanced images and the time-intensity curves produced were fit to an exponential wash-in model. Quantification using automatic image registration was compared to quantification without any image registration and quantification with manual registration.

Repeated analysis was made of individual clips in order to generate statistics on the improvement produced by automatic registration over using no registration. Manual registration was used as the standard for comparison. Quantification parameters (baseline intensity, amplitude of enhancement and rate constant) were closer to the manual alignment values when automatic registration was used than when no registration was used. The goodness-of-fit (correlation coefficient) of the exponential fit to the time-intensity curve was significantly improved when automatic alignment was used compared to using no alignment.

Analysis was also made of a single ROI in clips from each of the fourteen patients in the study. The goodness-of-fit never was lower when automatic registration was used relative to no

alignment and substantial improvement was seen in many cases. The amount of improvement was highly dependent on the amount of movement in the clip and the ROI placement. As is shown in the following figure, the improvement with both automatic and manual alignment was greatest for clips where the initial goodness-of-fit was in the range of 0.65-0.85. Clips showing lower initial correlations were not greatly improved while clips where the no-alignment goodness-of-fit was > 0.85 had so little motion that motion compensation did not have a large impact.

Automatic image registration using warping significantly improved quantification compared to no registration in a small fraction of the time required for manual alignment. Automatic alignment should reduce the number of images that need to be corrected manually and therefore accelerate contrast quantification workflow.

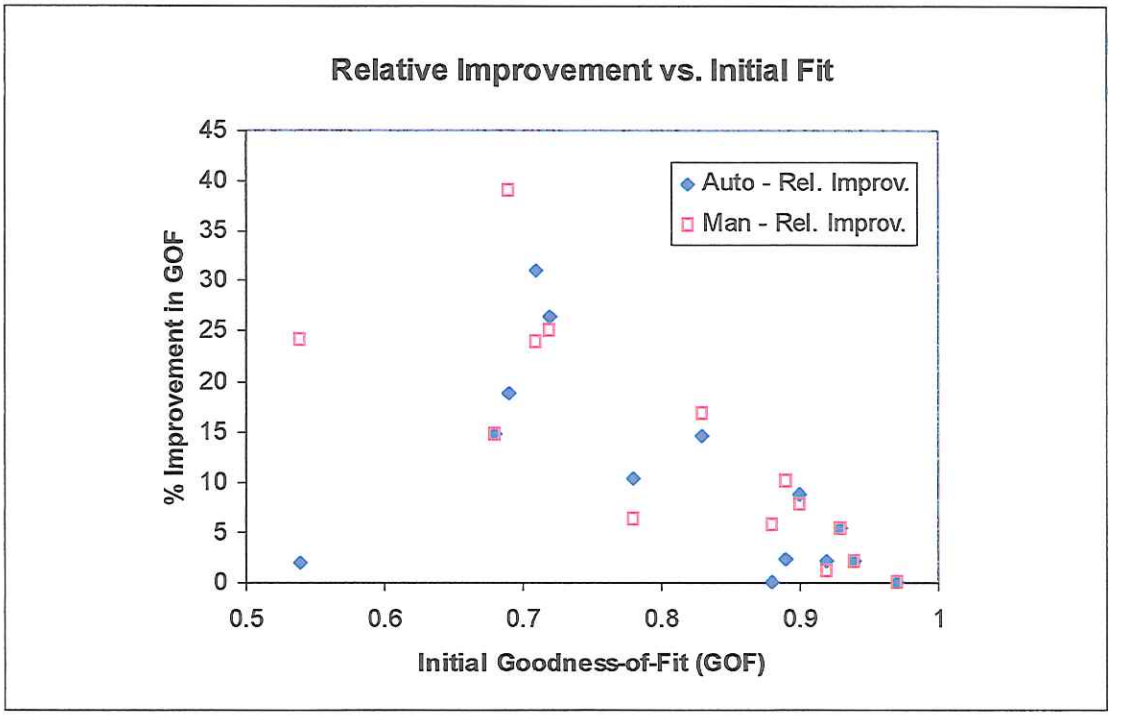

Quadratic B-mode (QB-Mode) Ultrasonic Imaging with Coded Transmit Waveforms

Daniele Cecchini, Hui Yao, Pornchai Phukpattaranont and Emad S. Ebbini
Department of Electrical and Computer Engineering
University of Minnesota, Minneapolis, MN 55455

Abstract

QB-mode imaging employs second order Volterra filters to separate quadratic components from beamformed RF data resulting in images with improved contrast and increased dynamic range. QB-mode imaging does not require pulse sequences to separate linear from nonlinear echo signal components thus preserving the frame rate of the imaging system. Furthermore, quadratic Volterra kernels can be obtained from imaging data and have been shown to detect any quadratic interaction ($f_1 + f_2 = f$) throughout the bandwidth of the transducer. This means that, unlike harmonic imaging, wideband transmit pulses can be used thus preserving the resolution of the imaging system. In this paper, we present the first demonstration of the use of QB-mode imaging with coded waveforms. Image data were collected from a flow phantom using linear and quadratic chirp waveforms of 6.5 μs duration. BR14 UCA microbubbles (dilution 1:100000) were circulated in one channel while cellulose microspheres (linear scatterers) were circulated in a parallel channel. Chirp waveforms with very low MI ($\tilde{0}$.02 - 0.1) covering the frequency band of 1.5 - 3.7 MHz on the Technos MPX (Esaote, S.p.A., Genoa, Italy) CA421 abdominal probe were used. Sensitivity to UCA at the given dilution was established with and without compression. Conventional matched filter compression achieved a slight, but measurable increase in specificity. QB-mode images were formed after conventional pulse compression and have shown significant increase in specificity. This was quantified by evaluating the contrast-to-tissue ratio (CTR) for the UCA channel. For example, with linear chirp waveform, the average CTR from 18 frames was 3.2, 5.4, and 14.3 for the uncompressed, compressed, and quadratically filtered compressed data. On the other hand, the average linear-scatterer to tissue ratio (LSTR) was -1.2, -2.8, and -4.7 for the uncompressed, compressed, and quadratically filtered compressed data. Resolution measurements from a CIRS Model 40 quality assurance phantom give a 6-dB axial resolution of 2.06, 0.75, and 0.79 mm for the uncompressed, compressed, and the quadratically filtered compressed data. These results show that quadratic filtering of coded excitation data provide significant improvement in CTR without compromising the spatial resolution of the imaging system.

I. Introduction

Coded excitation has been proposed and successfully used in improving the signal-to-noise (and therefore the penetration depth) of conventional ultrasonic systems in both linear and nonlinear form [1]. It is recognized that the advantages of coded excitation can be extended to contrast-assisted ultrasonic imaging with proper compression of the harmonics [2]. In fact, coded waveforms (e.g. chirps) can produce significant increase in nonlinear bubble activity compared to conventional short duration pulses. This can be attributed to the duration of interaction between the transmitted pulse at or near the resonance frequency of the microbubble population. This was nicely demonstrated in [2], but it was also shown that pulse compression of the nonlinear component can produce range sidelobes and put limits on the bandwidth of the transmitted chirp.

We have recently validated the use of a second-order Volterra (SOVF) model for separating the linear and quadratic components of the beamformed radio frequency (RF) data in pulse-echo ultrasonic imaging. The model separates the signal into its linear and quadratic components. The quadratic component captures the second order nonlinearities in the echo data. Grayscale images from the quadratic component, referred to as quadratic B-mode (QB-mode) images, typically have higher contrast and increased dynamic range than the standard B-mode images (without loss in spatial resolution). An algorithm for finding the coefficients of the SVF based on a linear plus quadratic prediction model of the RF data was developed and validated in a variety of imaging situations, including *in vivo*. The quadratic kernels used for filtering the RF data for producing QB-mode images can be derived to minimize the prediction error (in a least-squares sense) and/or to maximize the contrast of a perceived contrast target. The latter criterion is particularly useful for imaging with ultrasound contrast agents

This work is funded in part by a grant from Esaote, S.p.A., Genoa, Italy and by Grant DAMD 17-01-1-330 from the US Army Medical Research and Materiel Command.

(UCAs). In this paper, we present experimental verification of the synergistic effect of using coded waveforms with quadratic filtering after conventional pulse compression.

II. Theory

Quadratic images are obtained from quadratic components of the SOVF model. The coefficients of the SVF are derived from the beamformed RF data taken from a representative region on a standard B-mode image. A minimum-norm least squares (MNLS) criterion is used to solve for the unknown filter coefficients of a linear plus quadratic prediction model. A brief description of the algorithm is given below, but full details can be found in [3].

MNLS Estimation of SOVF Coefficients The response of a quadratically nonlinear system with memory, $\hat{u}(n+1)$, can be predicted by a (discrete) second-order Volterra model operating on the m past samples:

$$\hat{u}(n+1) = \sum_{i=0}^{m-1} u(n-i)h_L(i) + \sum_{j=0}^{m-1}\sum_{k=j}^{m-1} u(n-j)u(n-k)h_Q(j,k), \tag{1}$$

where $h_L(i)$ is linear filter coefficients, $h_Q(j,k)$ represents quadratic filter coefficients. Note that while $\hat{u}(n+1)$ is nonlinear with respect to the beamformed data, it is linear with respect to the coefficients of the linear and quadratic kernels of the SOVF. Recognizing this fact, one can rewrite Equation 1 in vector form:

$$\hat{u}(n+1) = \mathbf{u}^T(n)\mathbf{h}, \tag{2}$$

where the data vector, $\mathbf{u}(n)$, is defined at sample n as

$$\mathbf{u}(n) = [u(n),\, u(n-1),\, u(n-2),\ldots,\, u(n-m+1), u^2(n),\, u(n)u(n-1),\ldots,\, u^2(n-m+1)]^T,$$

and the filter coefficient vector, $\mathbf{h}$, can be expressed as

$$\mathbf{h} = [h_L(0),\, h_L(1),\, h_L(2),\ldots,\, h_L(m-1), h_Q(0,0),\, h_Q(0,1),\ldots,\, h_Q(m-1,m-1)]^T.$$

Note that m is the system order and superscript ^{T} denotes the transpose. The total number of independent filter coefficients, N, is equal to $(m^2+3m)/2$ assuming a symmetrical quadratic kernel (i.e., $h_Q(j,k) = h_Q(k,j)$). Similarly, $\hat{u}(n+2), \hat{u}(n+3), ..., \hat{u}(n+M)$ can be represented in the form of (2) and expressed in the matrix form:

$$\mathbf{f} = \mathbf{G}\mathbf{h}, \tag{3}$$

where the vector $\mathbf{f}$ and the matrix $\mathbf{G}$ are defined as

$$\begin{aligned}\mathbf{f} &= [\hat{u}(n+1),\, \hat{u}(n+2),\ldots,\, \hat{u}(n+M)]^T \\ &= [u(n+1),\, u(n+2),\ldots,\, u(n+M)]^T\end{aligned}$$

and

$$\mathbf{G} = [\mathbf{u}(n),\, \mathbf{u}(n+1),\ldots,\, \mathbf{u}(n+M-1)]^T,$$

where M is the number of linear equations. Note that the linear and quadratic kernels can be estimated by solving (3). Well-known solutions to (3) are the least squares (LS) solution for the overdetermined case and the minimum norm (MN) solution in the underdetermined case. A MNLS solution can be obtained by

$$\mathbf{h}_{MNLS} = \mathbf{G}^{\dagger}\mathbf{f}, \tag{4}$$

where $\mathbf{G}^{\dagger}$ is a generalized inverse [4]. Assuming $\mathbf{G}$ has rank $r \le p$ ($\min\{M,N\}$), the SVD of $\mathbf{G}$ can be expressed as

$$\begin{aligned}\mathbf{G} &= \mathbf{U}\mathbf{\Sigma}\mathbf{V}^T \\ &= \sum_{i=1}^{r} \sigma_i \mathbf{u}_i \mathbf{v}_i^T,\end{aligned} \tag{5}$$

where Σ is a $M \times N$ diagonal matrix with singular values $\sigma_1 \geq \sigma_2 \geq \ldots \geq \sigma_r > \sigma_{r+1} = \ldots = \sigma_p = 0$, $\mathbf{U}$ and $\mathbf{V}$ are unitary matrices, and $\mathbf{u}_i$ and $\mathbf{v}_i$ are the orthogonal eigenvectors of $\mathbf{G}\mathbf{G}^T$ and $\mathbf{G}^T\mathbf{G}$, respectively [4]. The MNLS solution to (4) is then given by

$$\mathbf{h}_{MNLS} = \sum_{i=1}^{r} \frac{\mathbf{u}_i^T \mathbf{f}}{\sigma_i} \mathbf{v}_i. \tag{6}$$

Regularization The SVD of $\mathbf{G}$ forms a basis for regularization by appropriate selection of singular modes that enhance the reconstructed image in some sense. There are a number of approaches for regularization of (6) including single parameter and rank reduction regularization [5]. The latter, sometimes referred to as the truncated singular value decomposition (TSVD), produces a solution by truncating the number of singular modes of $\mathbf{G}$ with the smallest singular values below a certain threshold. The kth order TSVD solution is given by:

$$\mathbf{h}_k = \sum_{i=1}^{k} \frac{\mathbf{u}_i^T \mathbf{f}}{\sigma_i} \mathbf{v}_i, \tag{7}$$

where the truncation parameter $k \leq r$, also known as the rank of the approximation, is the number of singular modes used to compute the estimate. The regularization is guided by the mean square error criterion:

$$\hat{E}(k) = 10 \log_{10} \left(\frac{\| \mathbf{f} - \mathbf{G}\mathbf{h}_k \|_2^2}{M} \right), \tag{8}$$

where $\| \cdot \|_2$ is the l_2 norm. In the context of the linear and quadratic prediction approach taken in this paper, the *MSE* decreases monotonically with k. A criterion for choosing an appropriate value of k is needed. In the context of contrast-agent imaging, an obvious criterion is the contrast-to-tissue ratio (*CTR*)

$$CTR = 10 \log_{10} \left(\frac{\overline{P}_C}{\overline{P}_T} \right), \tag{9}$$

where $\overline{P}_C$ is the average power of signals in a UCA region and $\overline{P}_T$ is the average power of signals in a tissue region. The average power of signals in a given region, $\overline{P}$, can be expressed as:

$$\overline{P} = \frac{1}{MN} \left(\sum_{i=1}^{M} \sum_{j=1}^{N} x_{ij}^2 \right), \tag{10}$$

where x_{ij} is the signal in that region. Note that the CTR used in this algorithm is determined from quadratic components of the SOVF model. The CTR provides a meaningful stopping criterion for TSVD since $E(k)$ is monotonically decreasing or non increasing with k.

III. Materials and Methods

To demonstrate the potential of the approach, we evaluated the new algorithm by collecting image data from flow phantom. Linear and quadratic pseudo-chirp signals were used ($\tilde{6}\mu$s duration, 1.56 - 3.7 MHz). The details of each experiment are given below.

The setup shown in Figure 1 was used in obtaining images of a flow phantom (Model 524; ATS Laboratories, Inc., Bridgeport, CT) containing four flow channels with diameters 2, 4, 6, and 8 mm embedded in rubber-based tissue mimicking material. The flow phantom was connected to a flow system with a roller pump (Model 77200-60; Cole-Parmer Instrument Co., Vernon Hills, IL). Subsequently, the diluted contrast agents and linear scatter were circulated and constantly stirred in beakers using a magnetic plate stirrer (EW-84303-20; Corning Inc., Corning NY). The contrast agent, BR14 (Bracco Research S.A., Geneva, Switzerland), was used. BR14 is a new experimental agent that consists of high molecular weight gas bubbles encapsulated by a flexible phospholipid shell. Cellulose particles (Sigmacell Type 20, Sigma Chemical Co., Milwaukee, MI) was used as contrast linear scatters.

RF data were recorded and saved for off-line processing by the Technos MPX ultrasound system (ESAOTE S.p.A, Genoa, Italy) with a convex array probe with the center frequency 3.2 MHz (CA421; ESAOTE S.p.A, Genoa, Italy) located perpendicularly to the flow channels. In addition, the probe position was slightly tilted to avoid strong specular reflections. RF data were acquired with 16-bit resolution at 20-MHz sampling frequency without time gain control (TGC) compensation. A

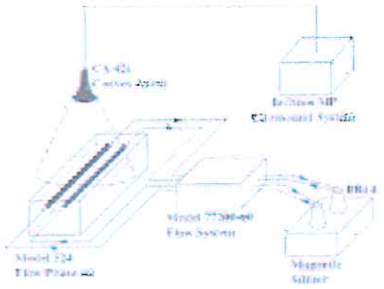

Figure 1: The imaging setup for the flow phantom

1-cycle pulse (0.7 MI) at 3.2 MHz was transmitted to form standard B-mode images. A 15-cycle 6.08 μs length linear chirp with frequency range from 1.56 MHz to 3.7 MHz and a 15-cycle 6.43 μs length quadratic chirp with frequency range from 1.69 MHz to 4.17 MHz were transmitted to form coded-excitation images with different transmit signal levels (MI values of $\tilde{0}$.02, 0.04, 0.07 and 0.1). Eighteen frames of RF data were collected (at $\tilde{1}$ fps) for all modes. The first 10 seconds data were collected with flow rate 0.04 m/s, for the last 10 seconds the flow was stopped. Echoes from the UCA channel were examined for evidence of bubble destruction. The lowest MI ($\tilde{0}$.02, which is well below the reporting limit of the Technos MPX) data was determined to have practically no bubble destruction.

For comparison of contrast enhancement between images from different techniques, we determine CTRs from data in the RF domain before scan conversion using (9). Three regions from the UCA channel, tissue-mimicking phantom, and the cellulose channel are used for CTR and LSTR calculations (LSTR is computed in an identical manner to CTR, but using RF data from cellulose channel). All regions consisted of 3-mm axial segments of connected A-lines. In addition, CTR values representing contrast enhancement of each flow channel are reported using a specific frame and average value computed over 18 frames of data. The tissue region is located at the same depth as the UCA and LS regions.

The imaging target used to evaluate spatial resolution of the QB-mode image is a quality assurance (model 40; CIRS, Norfork, VA). The quality assurance phantom contains known test objects, i.e., wire resolution targets, cystic targets, high contrast targets, and high density targets, embedded in liver mimicking material. Coded excitation image data was acquired and processed in precisely the same manner as used for the flow phantom data. A lower MI (0.13) was used for B-mode data as there was no need to excite the UCA with a single cycle pulse centered at 3.2 MHz as in the flow phantom experiment.

IV. Results

A. UCA CTR Enhancement in Flow Phantom

The imaging probe was positioned so that the 6-mm and the 4-mm channels are within the field of view (FOV) of a $\pm 22.5°$ sector. Two flow configurations were used:

- A baseline configuration where water was circulated through both flow channels.
- UCA (1:100000 dilution) was circulated through the 6-mm channel and cellulose (1 gram/500 ml saline) was circulated through the 4-mm channel during the first 10 seconds.

For each configuration, we collected 18 frames of RF data. Figure 2(a) shows the standard B-mode image (MI=0.7) with a dynamic range of 50 dB. At this MI, both the UCA and cellulose channels appear filled and are on the same order of the surrounding "tissue" region. Figure 2(b) shows the coded excitation from the lowest MI linear chip with a dynamic range of 40 dB. A simple matched filter compression was applied to the beamformed data and the resulting image is shown in Figure 2(c) with a dynamic range of 40 dB. A quadratic filter was derived from the contrast region and in the compressed

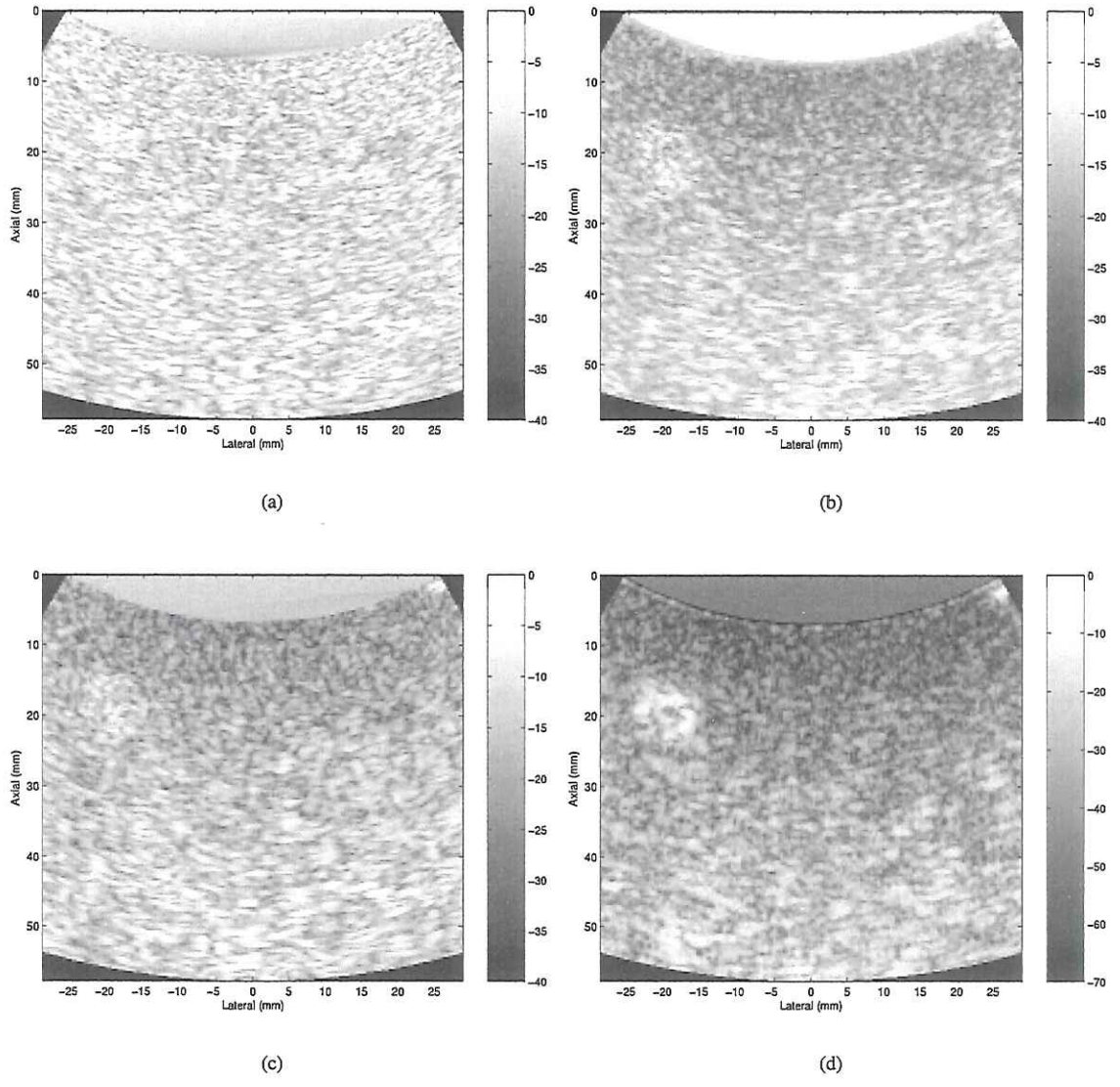

Figure 2: B-mode image (40 dB) of the flow phantom is shown in (a), coded excitation with 2 Volt linear chirp image (40 dB)is shown in (b), the compression (40 dB) of image (b) is shown in (c),QB mode (70 dB) of image (c) is shown in (d).

linear chirp. A typical QB-mode image processed from compressed linear chirp is shown in Figure 2(d) with a dynamic range of 70 dB.

The results shown in Figure 2 demonstrate the increased sensitivity of the compressed chirp data compared with the conventional B-mode and uncompressed chirp data. A slight but measurable increase in CTR can be observed in the compressed chirp image compared to the B-mode and uncompressed chirp data. The CTR values are 5.6, 1.85, and 4.8 for the compressed chirp, B-mode, and uncompressed chirp data, respectively. The average values for the 18 frames are consistent with this result and have the values 5.35, 3.77, and 3.15. These results are tabulated in Table I. The QB-mode image in Figure 2(d), on the other hand, shows a significant increase in specificity for the UCA channel (reflected by a CTR values of 13.1 for the shown frame and 14.2 on average).

TABLE I

CTR AND LSTR VALUES FOR THE B-MODE (MI=0.7) AND LINEAR CHIRP (MI=0.02). UCA AND LS ARE THE VALUES FROM THE UCA AND CELLULOSE CHANNELS FOR THE DISPLAYED FRAME, RESPECTIVELY. UCA_{Ave} AND LS_{Ave} ARE THE AVERAGE VALUES FOR ALL 18 FRAMES.

	UCA	LS	UCA_{Ave}	LS_{Ave}
B mode	4.78	0.30	3.77	0.35
Linear chirp	1.85	-1.35	3.15	-1.2
Comp	5.60	-2.81	5.35	-2.80
QB Comp	13.10	-5.16	14.33	-4.73

TABLE II

RESOLUTION CALCULATED FROM WIRE TARGET NEAR MECHANICAL FOCUS (6-dB CRITERION).

Mode	Axial (mm)	Lateral (mm)
B mode	0.46	1.64
Linear chirp	2.06	1.64
Comp	0.75	1.69
QB Comp	0.79	1.68

V. CHARACTERIZATION OF SPATIAL RESOLUTION

We acquired RF data from the ultrasound quality assurance phantom with the same imaging setup as the flow phantom case to evaluate resolution of images. Figure 3(a) shows the B-mode (MI=0.13) image of the quality assurance phantom, which is used as a baseline for comparison. Please note that the Low-MI B-mode image has very low contrast such that the $\pm$15 dB targets in the image would be practically invisible. Figure 3(b) and (c) show the coded excitation with linear chirp and the compressed chirp image, respectively. A simple matched filter was used for compression and no attempt was made to optimize the compression filter. Nevertheless, the effects of compression can be clearly observed at the wire targets. In particular, the axial extent of the -6 dB level from the wire target near the mechanical focus of the probe (axial distance of 70 mm) was compressed from 2.06 mm to 0.75 mm. Furthermore, SNR improvement after compression is visible at depth.

Figure 3(d) shows the QB-mode image obtained after applying the quadratic kernel to the compressed chirp data. One can see that the resolution targets remain visible after quadratic filtering without apparent loss of spatial resolution. In addition, some level of tissue contrast is retained thanks to the high dynamic range of 100 dB in this case. The axial extent of the wire target at 70 mm axial distance is 0.79 mm, which is practically the same as in the compressed chirp case. Table II summarizes the resolution measurements at axial distance 70 mm for all imaging modes considered in this paper. While the lateral resolution is practically the same for all modes at mid range and for deeper targets, it is interesting to note that the quadratic filtered data demonstrates improved lateral resolution at shallow targets.

VI. DISCUSSION AND CONCLUSIONS

The results shown in the above section demonstrate some of the important advantages of nonlinear filtering of beamformed RF echo data from elongated coded waveforms. Flow phantom QB-mode images with UCA and linear scatterers show significant increase in CTR from the UCA channel with excellent localization. The latter point is fully supported by the imaging results from a tissue-mimicking resolution wire phantom.

B-mode images of the same phantoms at the same drive pulse amplitude did not show any enhancement due to the UCA. At medium MI values, the B-mode images (as seen in Figure 2(a)) show some sensitivity, but minimum specificity to contrast. Chirp waveforms at very low MI, on the other hand, offer the same level of sensitivity as medium MI B-mode. Quadratic filtering of compressed chirp data demonstrates significant increase in specificity rendering the UCA channel clearly visible above the surrounding tissue with an average 9 dB increase in CTR above the compressed chirp data.

It is worth emphasizing that the results acquired here with UCA dilution levels consistent with clinical practice and at operating signal levels resulting in minimum bubble destruction. Therefore, the results shown herein strongly support the feasibility of UCA imaging at very low MI and with excellent levels of sensitivity and specificity without loss of spatial resolution. In addition, the high dynamic range of quadratic images allows for visualization of tissue and UCA on the same image. This may allow for further quantitative imaging of nonlinear tissue activity in the future.

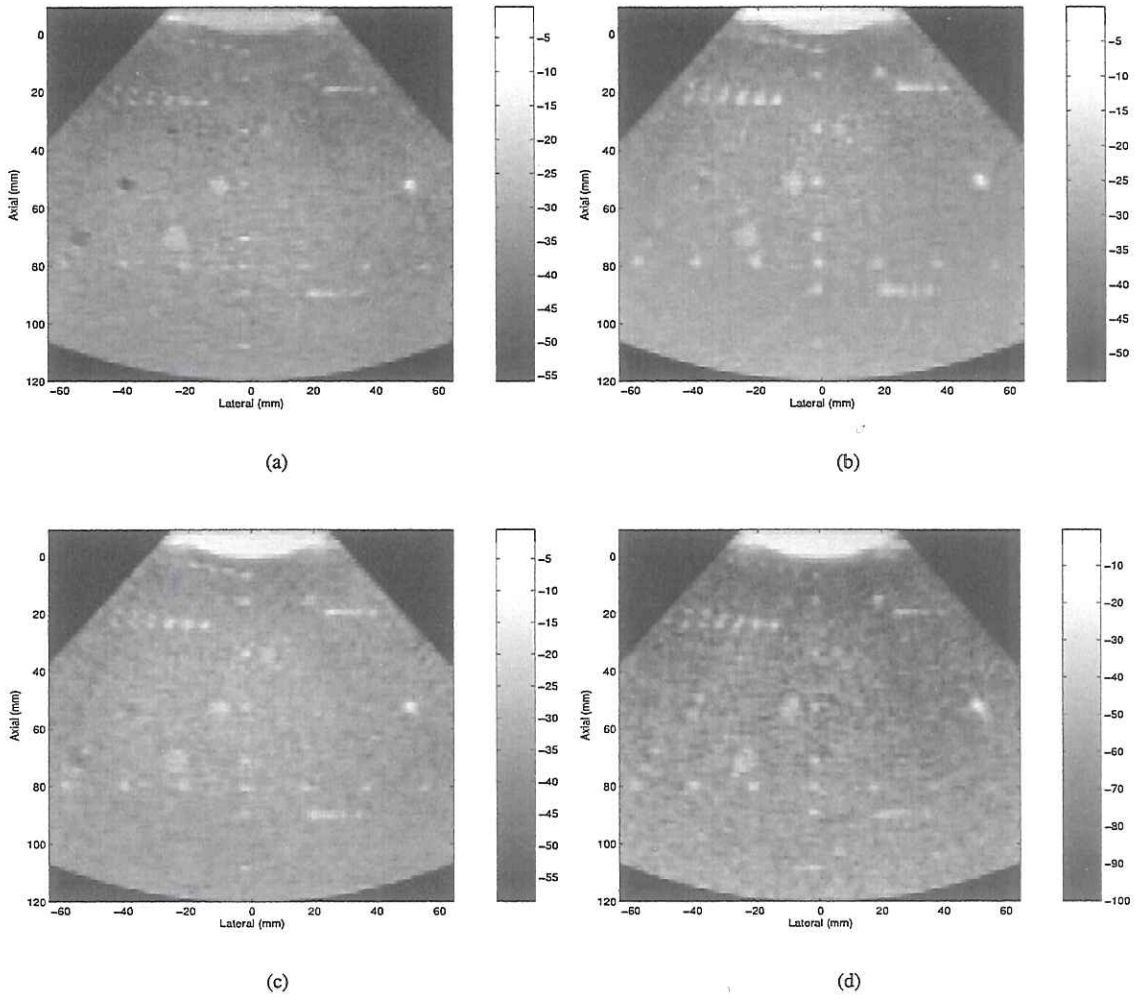

Figure 3: B-mode image (MI=0.13) of the wire phantom shown in (a), coded excitation linear chirp image (MI=0.02) is shown in (b), the compression of image (b) is shown in (c),QB mode of image (c) is shown in (d).

ACKNOWLEDGMENTS

We are grateful to Prof. Franco Bertora and Dr. Paolo Pellegretti from Esaote for their help, support, and valuable suggestions on all aspects of this work.

VII. REFERENCES

[1] B. Haidar and R. Chiao, "Higher order nonlinear ultrasonic imaging," in *1999 IEEE International Ultrasonics Symposium*, 1999, vol. 2, pp. 1527–1531.

[2] J. Borsboom, C.T. Chin, A. Bouakaz, and N. de Jong, "Non-linear coded excitation method for contrast imaging," in *2001 Ultrasonics Symposium*, 2001, vol. 2, pp. 1729–1732.

[3] P. Phukpattaranont and E. S. Ebbini, "Post-beamforming second-order volterra filter for pulse-echo ultrasonic imaging," *IEEE Trans. Ultrason., Ferroelect., Freq. Contr.*, vol. 50, no. 8, pp. 987–1001, Aug. 2003.

[4] G. H. Golub and C.F. Van Loan, *Matrix Computations*, Johns Hopkins University Press, Baltimore, MD, 2nd edition, 1989.

[5] J. Shen and E. S. Ebbini, "A new coded excitation ultrasound imaging system: Part I–Basic principles," *IEEE Trans. Ultrason., Ferroelect., Freq. Contr.*, vol. 43, no. 2, pp. 131–140, 1996.

INTRAVASCULAR CONTRAST ULTRASOUND: A POTENTIAL TOOL FOR VASA VASORUM IMAGING

DE Goertz[1,2], ME Frijlink[1], LCA van Damme[1], R Krams[1,2], JA Schaar[1,2], FJ ten Cate[1], N de Jong[1,2,3], AFW van der Steen[1,2]

1- Erasmus MC, Rotterdam the Netherlands, 2- Interuniversity Cardiology Institute of the Netherlands, 3- Physics of Fluids, Twente University

Background: The identification of vulnerable atherosclerotic plaques is a central issue in cardiac imaging. Plaque vulnerability is known to be related to its composition, degree of inflammation, and strain distribution. It is increasingly recognized that the development of neovascular vasa vasorum is necessary for plaque progression, is linked to the inflammatory response, and may promote lesion instability. At present, there are no clinical tools capable of performing high resolution imaging of coronary artery vasa vasorum. The objective of this work is to develop and investigate intravascular ultrasound (IVUS) contrast agent techniques for assessing the microvascular status of atherosclerotic lesions. In this presentation, a nonlinear IVUS system is described and evaluated, and the feasibility of performing nonlinear contrast imaging of adventitial microvessels is evaluated.

Methods

Instrumentation:

A prototype nonlinear IVUS system was developed for *in vivo* tissue harmonic [1] and contrast imaging [2]. The approaches investigated to date have utilized the second harmonic of a 20 MHz transmit pulse and subharmonic of a 40 MHz transmit pulse. The detection of these signals is facilitated by the use of specialized single element mechanically scanned IVUS transducers developed to have a frequency response with peaks at 20 and 40 MHz [3].

Agent Characterization:

Previous optical and acoustic characterization work [4] has indicated that nonlinear scattering from conventional agents at high frequencies (20 to 30 MHz) is associated with subpopulations of small bubbles (micron and submicron sized bubbles). In this study, both decanted Sonovue™ and an experimental submicron agent (BG2423, Bracco Research, Geneva) were employed. Characterization experiments assessed the ability to initiate and detect nonlinear signals under conditions relevant to IVUS, as well as to isolate bubble signals from tissue signals during scanning.

In vivo Experiments:

Initial *in vivo* studies have been conducted in normal and atherosclerotic rabbit aortas. The IVUS catheter is situated in a region of interest in the aorta and agent is released proximally in the form of a bolus through a second catheter. Imaging data is acquired and processed off–line to track the agent dynamics following the bolus. Tissue is then excised for histology.

Results

In vitro characterization experiments indicated the ability to perform both subharmonic and second harmonic IVUS imaging of the submicron agent. Second harmonic imaging was found to improve the contrast to tissue ratio for decanted Sonovue™. Pulse-inversion approaches were feasible to apply during scanning to achieve improved tissue signal suppression.

In vivo second harmonic experiments indicated the detection of agent within microvessels in the adventitia following the injection of contrast. Agent is first detected within the main lumen, followed by its presence in adventitial vessels, and finally within the vena cava. These results suggest the potential for contrast IVUS as a technique for imaging vasa vasorum.

Acknowledgements: This work was funded by STW and ICIN. The experimental agent BG2423 was provided by Bracco Research, Geneva.

References

[1] Frijlink ME, Goertz DE, van Damme LD, Krams R and van der Steen AFW, "Intravascular ultrasound tissue harmonic imaging in vivo", Proc. IEEE Ultrasonics Symp., 2004.

[2] Goertz DE, Frijlink ME, de Jong N, and AFW van der Steen, "High frequency nonlinear scattering and imaging of a submicron contrast agent", Proc. IEEE Ultrasonics Symp. 2004

[3] Vos HJ, Frijlink ME, Droog E, Goertz DE, Blacquire G, Gisolf GA, De Jong N, and van der Steen AFW, "A 20-40 MHz Ultrasound Transducer for Intravascular Harmonic Imaging", Proc. IEEE Ultrasonics Symp., 2004.

[4] Goertz DE, Frijlink ME, Bouakaz A, Chin CT, de Jong N and van der Steen AWF, "The effect of bubble size on nonlinear scattering at high frequencies", Proc. IEEE UFFC Symp., 2003.

THE RESONANCE FREQUENCY OF INDIVIDUAL BUBBLES OF BR-14

S.M. van der Meer[1], C.T. Chin[2], A. Bouakaz[2], M. Versluis[1], N. de Jong[1,2], D. Lohse[1]

[1] *Physics of Fluids, University of Twente, Enschede, The Netherlands*
[2] *Erasmus Medical Center, Rotterdam, The Netherlands*

Introduction:
An ultrasound contrast agent (UCA) is a liquid containing small, encapsulated microbubbles. A general property is the size distribution as measured e.g. with a coulter counter, resulting in its mean size and the range. For BR-14, e.g. the mean size is 3 micrometer, while 95 % of the bubbles are smaller than 10 micrometer. Acoustic characterization is done on a representative sample of the UCA, containing many microbubbles, resulting in scattering and attenuation properties as function of the frequency [1,2]. From this data the resonance behavior of the sample can be deduced. Since the sample contains many microbubbles no direct conclusion can be drawn for individual bubbles.

Here we develop a method to study the dynamics of individual bubbles in an UCA. In more detail: to develop a method to measure the resonance frequency of individual bubbles. The resonance frequency is an important property, from which shell properties of bubbles can be determined.

Methods:
The experimental setup is schematically drawn in Fig. 1. BR-14 contrast bubbles, supplied by Bracco Research SA, Geneva, Switzerland, were led through a capillary inside a small water-filled container. On one side a broadband single element transducer was mounted. An Olympus microscope with a 60x high resolution water-immersed objective and a 2x magnifier produced an image of the contrast bubbles. The high speed camera Brandaris 128 [3], with frame rates up to 25 Mfps, produced recordings of the dynamics of the contrast bubbles during insonification. An arbitrary waveform generator was used to produce waveforms, while an ENI A-500 amplifier was used to amplify the waveforms.

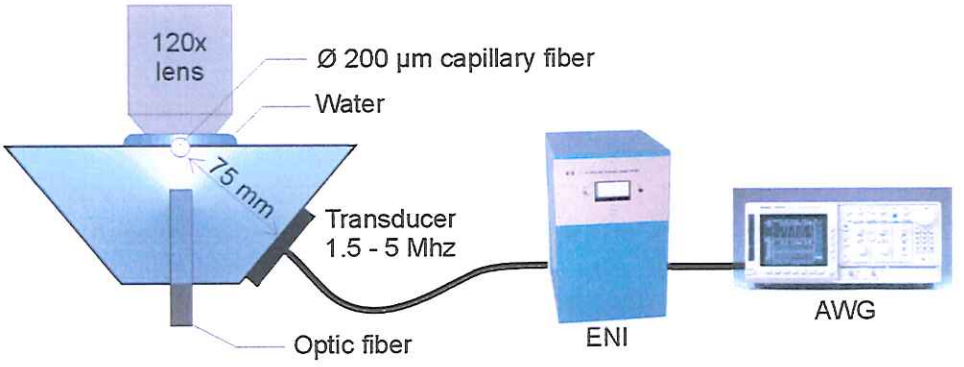

Figure 1: Experimental setup.

Individual bubbles were visualized under the microscope and insonified with ultrasound generated with the broadband single element transducer. The individual bubbles were insonified with sequential bursts of 8 cycles, with increasing center frequency. In this study the start frequency was 1.5 MHz and the final frequency 5 MHz, with a step size of 160 kHz. The acoustic pressure was 130 kPa and was programmed to be equal for all frequencies.
The oscillations of the individual bubbles were recorded with a fast framing camera, the Brandaris 128, running at a frame rate of 15 Mfps. The Brandaris 128 was operated in segmented mode, a unique property of the camera, where the 768 frames of the camera are divided into 24 segments of 32 images each, resulting in fully resolved R-t curves per acoustic frequency component. The total procedure took about 1 s. From the segmented sequence the radius- time curves for each individual bubble were measured for each frequency component. An example of this is shown in Fig. 2. The graph consists of 24 R-t curves of one single contrast bubble, put side by side, and separated by dotted lines.

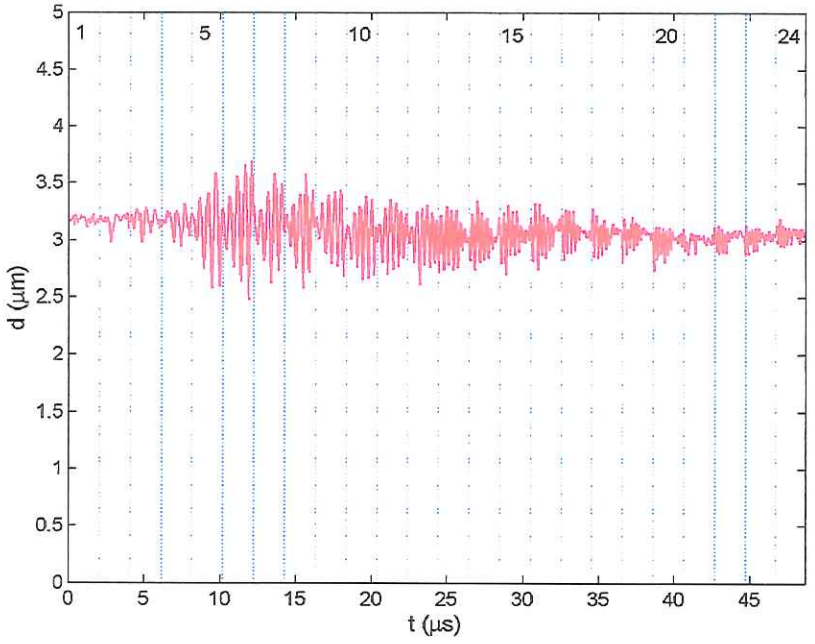

Figure 2: A combined radius-time graph of one single contrast bubble.

From the R-t curves the maximum radius was determined and normalized to the resting radius R_0, resulting in the relative radius excursion R_{max}/R_0.

Results:
R_{max}/R_0 as a function of the frequency was measured for individual bubbles between 1 and 6 micrometer and its resonance behavior was observed. E.g. for a bubble of 4.0, 3.2 and 2.6 micrometer the measured resonance frequency was 1.7, 2.2 and 3.1 MHz, respectively. This is shown in Fig. 3. Theoretical calculations based on free gas bubbles result in similar values, suggesting the shell influence on the resonance frequency to be minimal.

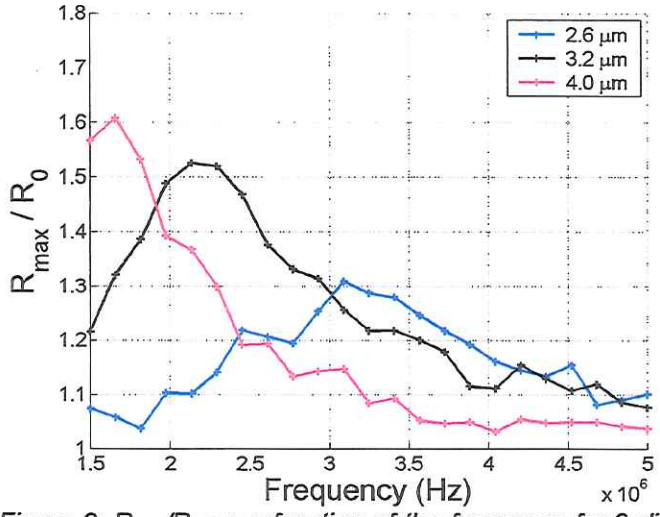

Figure 3: R_{max}/R_0 as a function of the frequency for 3 different bubble sizes. The legend shows the initial bubble diameters.

Conclusion:

We have shown that optical characterizing of individual bubbles is possible, which can have essential influence on new theoretical models, development of new UCA and acoustic detection methods.

[1] P.J.A. Frinking, N. de Jong, "Acoustic modeling of shell-encapsulated gas bubbles", *Ultrasound in Medicine and Biology*, vol. 24, no. 4, pp. 523-533, 1998.

[2] P.J.A. Frinking, N. de Jong, E.I. Céspedes, "Scattering properties of encapsulated gas bubbles at high ultrasound pressures", *J. Acoust. Soc. Am.*, vol. 105, no. 3, pp. 1989-1996, 1999.

[3] C.T. Chin e.a., "Brandaris 128: A digital 25 million frames per second camera with 128 highly sensitive frames", *Rev. Sci. Instrum.*, vol. 74, no. 12, pp. 5026-5034, 2003.

KEYWORDS

ultrasound contrast agent

resonance frequency

COMBINING MULTI-PULSE SEQUENCES WITH CODED EXCITATION FOR ENHANCED SENSITIVITY TO MICROBUBBLES.

Robert J. Eckersley & Kevin Chetty

Ultrasound Group, Imaging Sciences Department, Imperial College, London, U.K.

Multi-pulses sequences such as pulse inversion (PI), amplitude modulation (AM), or a combination consisting of both phase and amplitude modulations (PIAM), have been shown to be essential in imaging microbubble contrast agents. The key to the success of these approaches is their ability to separate the non-linear echoes of the microbubbles from the linear echoes arising from the surrounding tissues. The primary motivation for this is the detection of blood flow in the microvasculature. Although the microvasculature makes up a large part of the overall blood pool the individual vessels are minute and the flow within them is extremely slow. In order to detect these signals using microbubble contrast agents a technique with high sensitivity to non-linear signals is required, furthermore the insonating pressures which the microbubbles are exposed to must be kept as low as possible to prevent the destruction of the agents before they arrive in the region of interest. In previous work the benefits of PIAM have been demonstrated for such applications[1-3]. The advantage of PIAM over PI is due to the preservation of the nonlinearities in the scattered signals over the entire bandwidth of the transducer rather than at specific harmonics.

The use of coded pulses in ultrasound imaging is well established as means of improving the signal-to-noise (SNR) within B-mode imaging. In particular the application of frequency encoded pulses or chirps has been tried, tested and implemented on a number of commercial systems, e.g. [4, 5]. The application of chirps for imaging of microbubbles has also been investigated and the improvement in SNR shown to apply equally well in this case [6]. In this study we have combined the multi-pulse PIAM approach with chirp encoded pulses.

PIAM and chirp encoding are ideally suited for combination as the main benefit of each approach is the ability to fully utilise the available transducer bandwidth.

A series of in-vitro experiments will be presented in which the SNR boost (typically +10 dB) of the chirp encoding is shown to be maintained when combined with multi-pulse PIAM processing. The enhancement of the non-linear microbubble echoes over linear echoes is also maintained; an example is shown in Fig. 1 & 2. Issues concerning axial resolution and non-linear propagation will be discussed.

In conclusion the boost in SNR afforded by the chirp encoding means that PIAM processing can been more successfully applied at lower insonating pressures (less bubbles destruction), the increased sensitivity might also be used to improve penetration depth of microbubble modes.

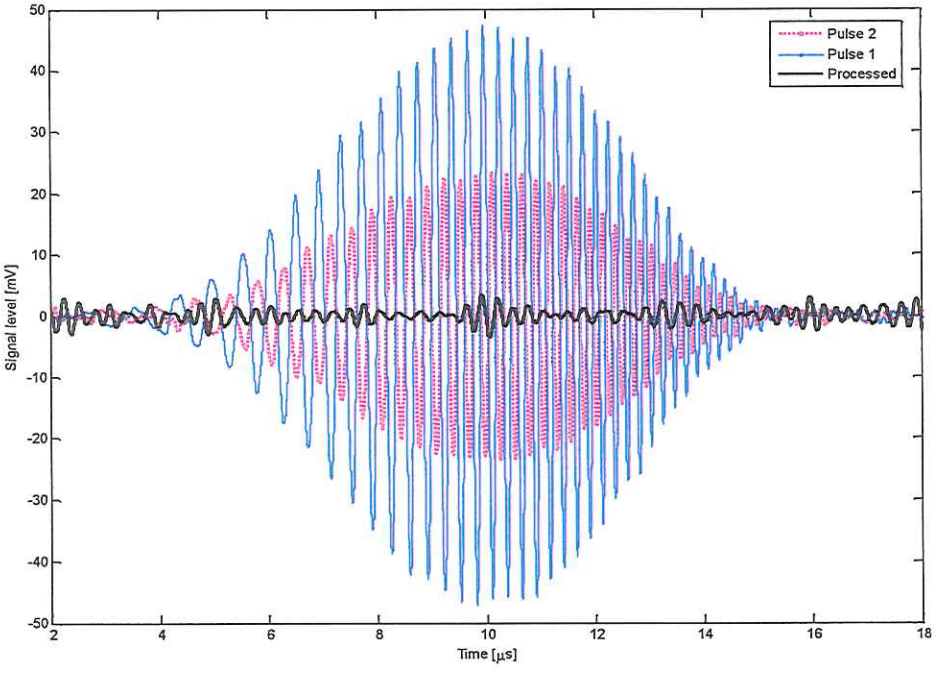

Figure 2: Plot of radio-frequency signal show echo of 2 pulse chirp PIAM sequence from a plane reflector. The processed post compression and combination signal (dark line) shows a complete cancellation of these linear echoes.

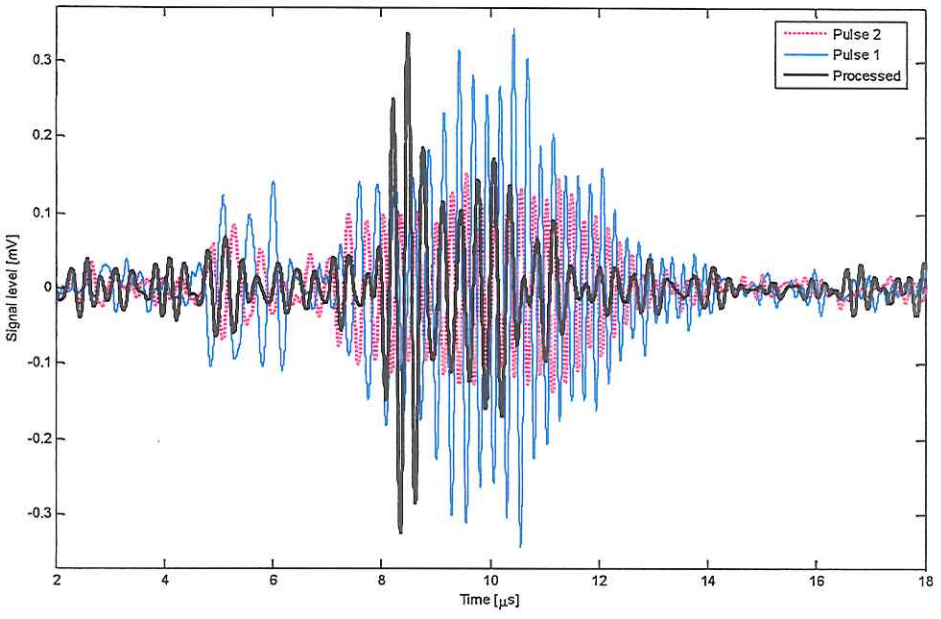

Figure 3: Same as Fig. 1 except echoes arise from scattering by a suspension of Sonovue. In this case the processed signals (dark line) show a strong signal resulting from the non-linear component in the scattered signals. Both experiments performed using 3.5 MHz broadband insonation with peak negative pressure of 53 kPa.

References:

[1] R. J. Eckersley, C. T. Chin, and P. N. Burns, "Optimising multi-pulse imaging schemes for microbubble contrast agents at low-acoustic power," presented at RSNA 2001: *Radiology*, vol. 221, pp. 554-554, 2001.

[2] R. J. Eckersley, C. T. Chin, and P. N. Burns, "Optimising phase and amplitude modulation schemes for imaging microbubble contrast agents at low acoustic power," *Ultrasound In Medicine and Biology*, vol. (in press), 2004.

[3] P. J. Phillips, "Contrast Pulse Sequences (CPS): Imaging nonlinear microbubbles," presented at 2001 IEEE Ultrasonics Symposium, 2001.

[4] T. X. Misaridis, K. Gammelmark, C. H. Jorgensen, N. Lindberg, A. H. Thomsen, M. H. Pedersen, and J. A. Jensen, "Potential of coded excitation in medical ultrasound imaging," *Ultrasonics*, vol. 38, pp. 183-189, 2000.

[5] M. H. Pedersen, T. X. Misaridis, and J. A. Jensen, "Clinical evaluation of chirp-coded excitation in medical ultrasound," *Ultrasound in Medicine and Biology*, vol. 29, pp. 895-905, 2003.

[6] J. Borsboom, C. T. Chin, and N. de Jong, "Experimental evaluation of a non-linear coded excitation method for contrast imaging," *Ultrasonics*, vol. 42, pp. 671-675, 2004.

PULSING SCHEMES FOR HIGH MI CONTRAST IMAGING

Tony Brock-Fisher, Michalakis Averkiou, Matt Bruce, Seth Jensen, Patrick G. Rafter, Jeffry Powers

Philips Electronics, Andover, USA

Contemporary contrast detection modes can be generally classified into two categories; nondestructive low-MI real time methods, and high-MI destructive methods. Many different techniques involving transmit pulsing schemes have been devised for low-MI imaging, including changing amplitude, and/or phase between the multiple pulses of each transmit direction. These methods are typically optimized to maximize contrast to tissue ratio (CTR); that is they attempt to suppress linear tissue response as much as possible while maximizing contrast agent response. At the MI levels used, the second harmonic response from tissue is quite small, so there has been little concern about minimizing the second harmonic tissue response.

For the high MI contrast imaging methods, differing techniques are used to suppress the tissue response. One such technique is Harmonic power Doppler processing which is used to detect high frequency Doppler signals generated by bubble disruption within a sample volume. Ultraharmonics is another high MI technique which utilizes narrow bandwidth transmit pulses to create gaps between the received tissue responses at the fundamental, second harmonic, and third harmonic. Contrast agent destruction results in a broadband acoustic response. Receive filters are tailored to maximize CTR by receiving the broadband bubble response in the areas of low tissue response. In high MI methods, the second harmonic response from tissue can be significant.

This paper describes a pulsing technique for contrast detection which not only reduces the fundamental linear response from tissue, but also suppresses the second harmonic tissue response. Using this technique, the contrast to tissue ratio can be significantly improved in clinical situations where the imaging power levels are high enough to cause a significant second harmonic tissue response.

The suppressed second harmonic contrast imaging technique was implemented on a Philips iU22 (GI) and iE33 (CV) Ultrasound system. RF measurements were made using tissue phantoms to measure the amount of second harmonic suppression that is achievable with the new technique. Additionally, images were acquired and analyzed from a contrast flow phantom, and the resultant contrast to tissue ratio was analyzed.

INVESTIGATING FREQUENCY EFFECT ON MICROBUBBLE ACOUSTICAL BEHAVIOUR AT LOW MECHANICAL INDICES

Sergio Casciaro[1,2], Rosa Palmizio Errico[2,6], Francesco Conversano[2,5], Christian Demitri[4], Alessandro Distante[1,2,3]

(1) IFC-CNR Lecce Section (Nat. Council of Research - Institute of Clinical Physiology), Lecce, Italy
(2) ISBEM (Euro Mediterranean Scientific Biomedical Institute), Brindisi, Italy
(3) Cardio Thoracic Department, Pisa University Medical School, Italy
(4) Innovation Engineering Department, Lecce University, Italy
(5) Bioengineering & Robotics Department, Pisa University, Italy
(6) Material Science Department, Lecce University, Italy

The interaction of gas-filled microbubbles with an ultrasound (US) beam has become, in recent years, a major area of research. This is largely due to the diversity of the reactions between the microbubbles and the US beam and the subsequent implications on the implementation of US diagnostic techniques. Over the past years, in vitro experiments (Frinking PJA and de Jong N, 1998; Frinking PJA, et al. 1999; Sboros V, et al. 2000a; Sboros V, et al. 2000b; Sboros V, et al. 2001; Sboros V, et al. 2002b; Sboros V, et al. 2003; Sboros V, et al. 2004; Porter TR, et al. 2003; Moran KE, et al. 1998) have improved the understanding of the interaction between contrast microbubbles and the US beam, but the effort to accomplish a full understanding of the phenomena is by no means complete. However an experimental setup that can cover a wide range of settings (e.g. flow rate, transmit frequency, mechanical index) similar to that used in diagnostic ultrasound applications is yet to be reported.

An in vitro system will be shown for the investigation of the behaviour of a new phospholipidic microbubble contrast agent supplied by Bracco Research SA (Geneva, Switzerland) flowing in an US field, coupled with an innovative signal acquisition and processing apparatus for the data analysis that provides a full range of settings. The used phantom, with further implementation, can reproduce almost all kind of human tissues, having the ability to easily modulate the vessel sizes and the different spatial and geometrical configurations and then several flow velocities of human blood.

The purpose of this study was to determine differences in contrast enhancement given by the experimental intravenous contrast agent, at constant dilution, employing different transmit frequencies and varying mechanical index (MI).

The considered microbubble dilution (1:80000) was obtained by injecting 0.62 mL of a 1:100 saline-diluted sample of contrast agent into a continuously stirred 500-mL saline beaker.

We chose this dilution value because in a preliminary study it was observed that the highest contrast enhancement among five different dilution values of the considered contrast agent (1:10000, 1:20000, 1:30000, 1:40000, 1:80000) was obtained for dilution 1:80000 at 2.5 MHz and MI = 0.08. In this paper more values of transmit frequency (2.5 MHz, 5 MHz, 7.5 MHz) will be investigated, varying also the mechanical index (0.08, 0.1, 0.2, 0.3) at each frequency.

A linear array probe (LA 532, Esaote, Florence, Italy) was used for the US pulses transmission with the indicated center frequencies. Focal point was set to 2 cm from the transducer surface. The transducer was positioned on the top of the phantom and it was connected to a digital ecograph (Megas GPX, Esaote, Florence, Italy) externally linked to a prototype for radiofrequency (RF) analysis (FEMMINA, developed by Florence University), able to get the full raw signal of the probe with no hardware nor software filtering of the echograph itself (Scabia M, et al 2002). The received signals were digitized at 40 MHz, 16 bits. Each frequency was tested at four MIs and the raw data were acquired in sequences of 100 frames at the highest frame rate possible with our acquisition system (about 5 frame/sec) and they were stored in FEMMINA for further off-line analysis. The number of data points was 3200 for each track and this information was acquired for 180 tracks in each frame.

The phantom was a custom-designed tissue-mimicking phantom (developed in collaboration with the Material Engineering section of the University of Lecce), made of hydrogel with a sound propagation velocity (1559,5 m/s) very close to the human liver value (1560 m/s, Bazzocchi M, 2001). It contained two 1-mm diameter vessels placed at the same stand-off distance within the phantom, both at 2 cm from the upper surface. Phantom vessels were perfused with the microbubble suspension, that was circulated at room temperature (25 °C) by a peristaltic pump (Peri-Star Model 500304, WPI Inc., FL, USA) at a constant flow rate of 8 mL/min.

Stored raw data were used to reconstruct image data through the Fortezza software (supplied by Florence University). This software was also utilized to implement a new algorithm to properly choose the Region Of Interest (ROI) inside the vessel cavity.

The selected ROI included 3 tracks and 25 data points per track, which was approximately equivalent to a square of 0.5 mm in side. In order to evaluate the combined effect of frequency and MI, another Fortezza algorithm was developed to measure backscatter intensity by FFT calculation over the defined ROI (fig. 1).

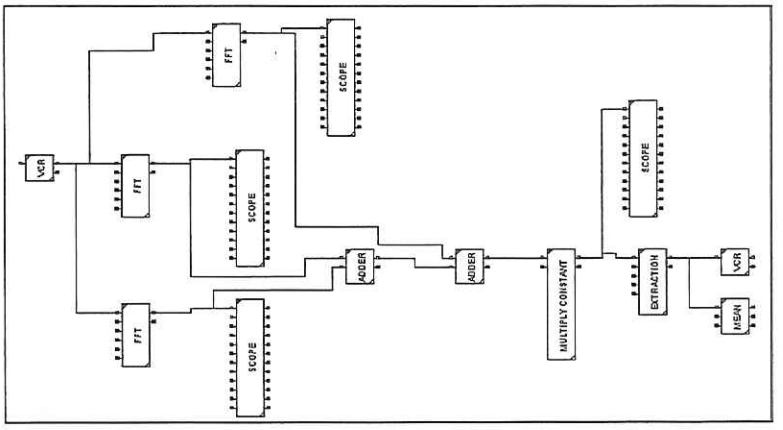

Fig. 1: Fortezza algorithm scheme used to calculate the FFT averaged over the ROI for each acquired frame.

Before FFT calculations were carried out, the raw data corresponding to the defined ROI and selected by means of a 25-point "Rect" window were zero-padded to 4096 points to increase the frequency resolution of the spectra ("FFT" modules, fig. 1). FFT was calculated in this way and visualized ("SCOPE" modules, fig.1) for every track of the ROI and the resulting curves were averaged ("ADDER" modules and "MULTIPLY CONSTANT" module, fig. 1) to obtain and visualize ("SCOPE" module, fig. 1) the FFT averaged over the ROI. This calculation has been repeated three times for every acquired frame sequence, corresponding to a specific combination of frequency and MI values. Each time a different FFT component (subharmonic, fundamental and second harmonic) was extracted ("EXTRACTION" module), visualized ("MEAN" module) and recorded ("VCR" module) in a Fortezza proprietary format file.

The obtained files were then converted in XLS format by an ad hoc implemented MATLAB® program (The Mathworks, Inc., Natick, MA); mean and standard deviation were calculated for each data sequence using the Origin software (OriginLab Corporation, Northampton, MA) and plotted against frequency for each MI (fig. 2).

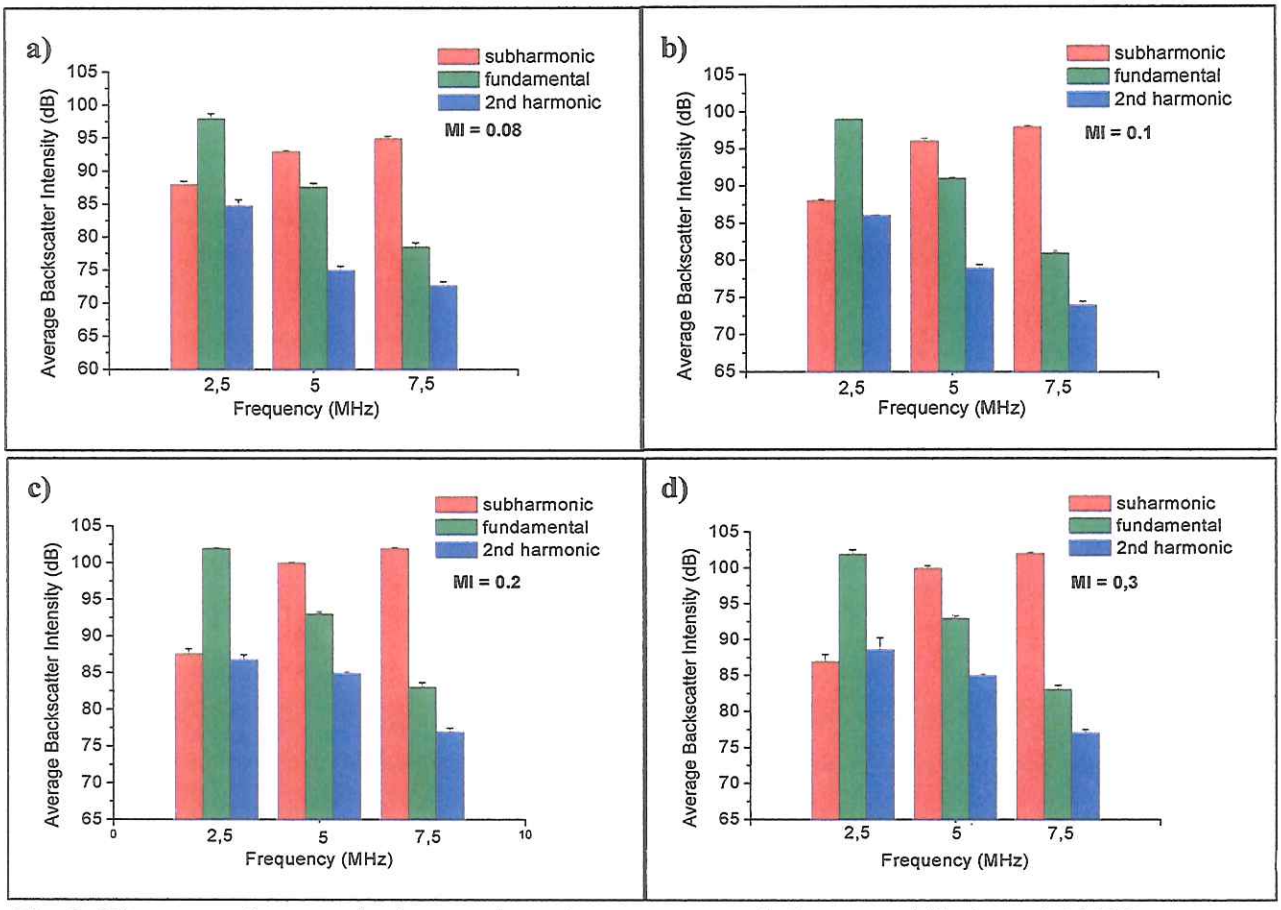

Fig. 2: Histogram of average backscatter intensity versus transmit frequency (dilution = 1:80000, ROI = 3 tracks, 25 points per track; error bars represent standard deviations of measured data): a) MI = 0.08; b) MI = 0.1; c) MI = 0.2; d) MI = 0.3.

Figure 2 displays the relationship between single FFT components and the transmit frequency at the various tested mechanical indices. In every histogram we can see how the fundamental and second harmonic backscatter intensities decrease with increasing frequency, while subharmonic components increase when frequency arises. For every tested MI value the highest intensity is observed at 2.5 MHz FFT component for 2.5 MHz and 5 MHz transmit frequencies, while at 7.5 MHz the highest value is observed at 3.75 MHz FFT component. In fig. 2-a and 2-b fundamental FFT component corresponding to 2.5 MHz transmit frequency is the highest, while, increasing MI, it is gradually overtaken by the subharmonic component corresponding to 7.5 MHz transmit frequency.

In conclusion, the employed phospholipidic contrast agent showed a significant contrast enhancement for each tested combination of transmit frequency and MI at 1:80000 dilution. In particular, at 2.5 MHz transmit frequency this contrast agent gives the best backscatter intensity in the fundamental component and its value doesn't increase in a remarkable way arising MI, so it should be possible to successfully use this microbubble suspension in conventional fundamental B-mode imaging already at the lower MI values. On the other hand, for applications that require 5 MHz or 7.5 MHz transmit frequencies, the best contrast enhancement achievable with the tested contrast agent is observed in correspondence of subharmonic components, for which the values increase arising MI until 0.2 and then remain approximately constant till MI equal to 0.3. Finally we can say that, to effectively employ this contrast agent dilution at 5 MHz or 7.5 MHz transmit frequencies, it should be necessary to work in subharmonic imaging modality with MI lower than 0.3.

REFERENCES

- Bazzocchi M. Ecografia, II edition. Idelson Gnocchi Editor, 2001.
- Frinking PJA and de Jong N. Acoustic modeling of shell-encapsulated gas bubbles. Ultrasound Med. Biol. 1998; 24: 523-33.
- Frinking PJA, de Jong N and Cespedes EI. Scattering properties of encapsulated gas bubbles at high ultrasound pressures. J. Acoust. Soc. Am. 1999 105.
- Moran KE, Anderson T, Sboros V, Sutherland GR, Wright R and MC Dicken WN. Quantification of the enhanced backscatter phenomenon from an intravenous and an intra-arterial contrast agent. Ultrasound Med. Biol. 1998; 24: 871-80.
- Sboros V, Moran CM, Anderson T, Pye SD, Macleod IC, Millar AM and McDicken WN. Evaluation of an experimental system for the in vitro assessment of ultrasonic contrast agents. Ultrasound Med. Biol. 2000a; 26: 105-11.
- Sboros V, Moran CM, Anderson T and Mc Dicken WN. An in vitro comparison of ultrasonic contrast agents in solutions with varying air levels. Ultrasound Med. Biol. 2000b; 26: 807-18.
- Sboros V, Moran CM, Pye SD and Mc Dicken WN. Contrast agent stability: a continuous B-mode imaging approach. Ultrasound Med. Biol. 2001; 27: 1367-77.
- Sboros V, Moran CM, Anderson T, Gatzoulis L, Criton A, Averkiou M, Pye SD and Mc Dicken WN. An in vitro system for the study of ultrasound contrast agents using a commercial imaging system. Phys. Med. Biol. 2001; 46: 3301-3321.
- Sboros V, Ramnarine KV, Moran CM, Pye SD and Mc Dicken WN. Understanding the limitations of ultrasonic backscatter measurements from microbubble populations. Phys. Med. Biol. 2002b; 47: 4287-99.
- Sboros V, Moran CM, Pye SD and Mc Dicken WN. The behaviour of individual contrast agent microbubbles. Ultrasound Med. Biol. 2003; 29: 687-94.
- Porter TR, Oberdorfer J, Rafter P, Lof J and Xie F. Microbubble responses to a similar mechanical index with different real-time perfusion imaging techcniques. Ultrasound Med. Biol. 2003; 29 1187-92.
- Sboros V, Moran CM, Pye SD and Mc Dicken WN. An vitro study of a microbubble contrast agent using a clinical ultrasound imaging system. Phys. Med. Biol. 2004; 49: 154-173.

Investigational Approach to Assessment of Myocardial Perfusion Echocardiograms

Jonathan Goldman MD
VP Medical Affairs
POINT Biomedical Corp.

Objective of myocardial perfusion by echocardiography

- Diagnosis of CAD Yes/No
- Differentiate Fixed vs. reversible perfusion defects
- Location of defect: Coronary Vascular Territory

Rest and stress max flow vs. stenosis severity (animal model)

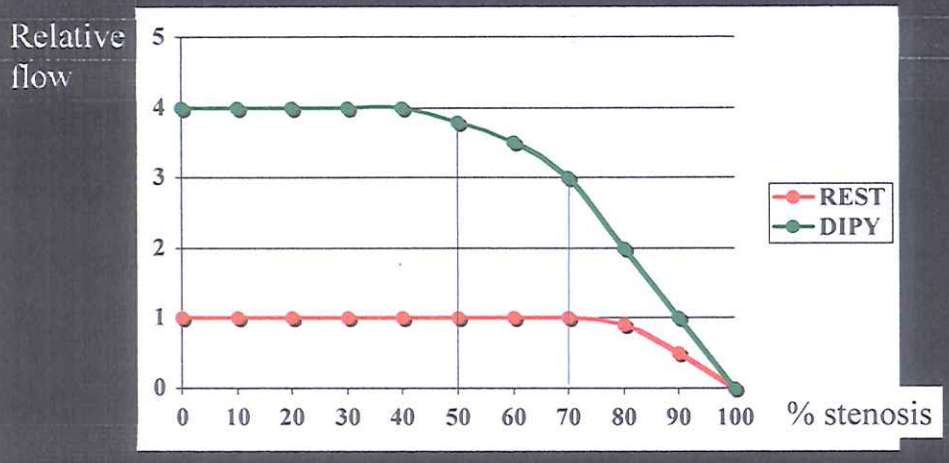

Gould et al. AJC 1974; 34: 50

Effect of single pulse of ultrasound on CARDIOsphere (Nitrogen is black)

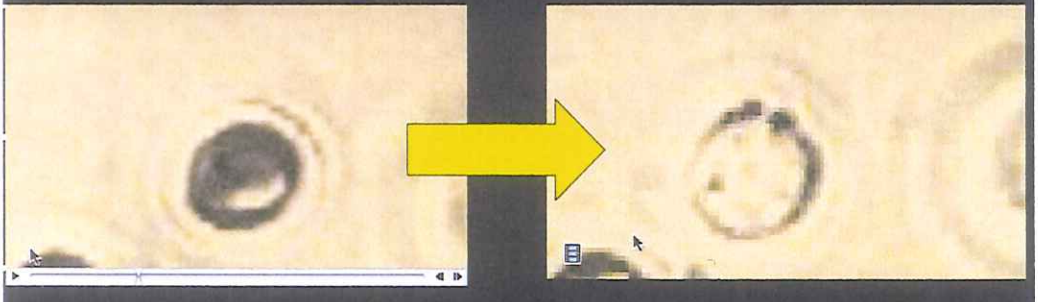

BEFORE (PERFUSION)

AFTER (POST DESTRUCTION)

Leong-Poi et al J Am Coll Cardiol, 2001 37 (2 Suppl A): 407A

Effect of single pulse of ultrasound on PFC gas

Optical recording with high speed camera
(12.500.000 frames/s)

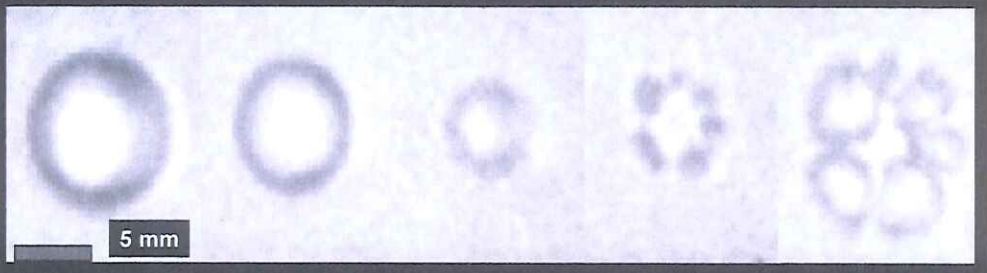

James E. Chomas et al., University of California, Biomedical Engineering Division, Davis CA, USA; Proc. IEEE Ultrasonics Symp., 1999.

PFC = perfluorocarbon

Longer Persistence of PFC bubble versus nitrogen bubble after ultrasound pulse

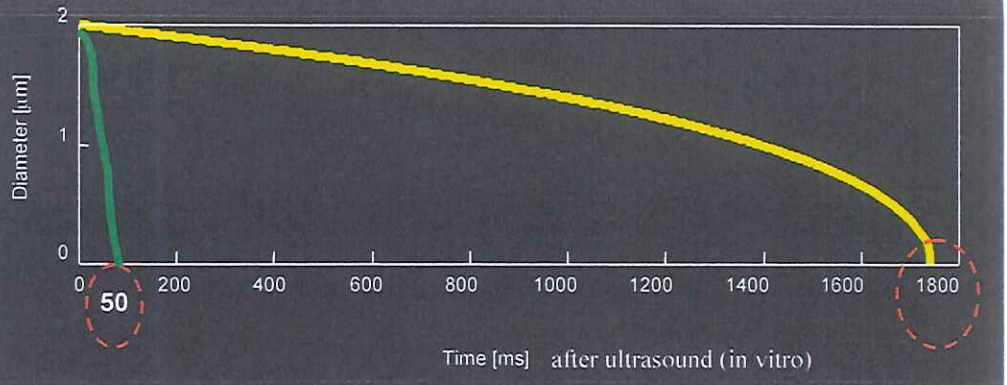

Rapid change in N2 content detected by Power doppler (a "change detector")
Ability to "get zero" critical to assess filling

Radial modulation imaging

Rune Hansen and Bjorn Angelsen and Peter Burns,
Toronto, Canada and Trondheim, Norway

Ayache Bouakaz, Jerome Borsboom, Michel Versluis and Nico de Jong
Erasmus MC Rotterdam, University of Twente and Interuniversity Cardiology Institute, the Netherlands

INTRODUCTION

One weakness of current methods used to image microbubble contrast is that they rely on the same emitted sound both to induce resonant nonlinear response of the bubbles and to form an image. This limitation becomes relevant as one tries to create contrast imaging methods that work well at high frequencies. Whereas ultrasound imaging scales with frequency – so that a 10 MHz ultrasound image looks like a 5 MHz ultrasound image except that the scale is halved – current contrast imaging does not scale comparably. Although in principle one could consider using bubbles of a reduced size, so that their resonant frequency coincides within the imaging frequency, fixed dimensions, such that of the vessel diameter and shell thickness, render this impractical at the moment. A more realistic approach is one which decouples the bubble excitation frequency from the imaging frequency. As with any other bubble imaging method, the goal is to detect the entire energy of the echo from the bubble and reject echoes from all other structures. Radial modulation imaging attempts to achieve this by taking exploiting the steep change in phase response to incident sound of a bubble while it is driven resonantly to above or below its resting radius. Here, we report preliminary investigation of radial modulation imaging using acoustic (Trondheim and Toronto) and optical (Rotterdam) methods.

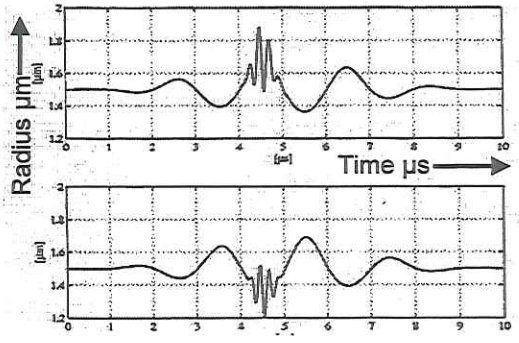

Figure 1: Simulation of bubble driven with a low frequency modulation signal and a high frequency imaging pulse

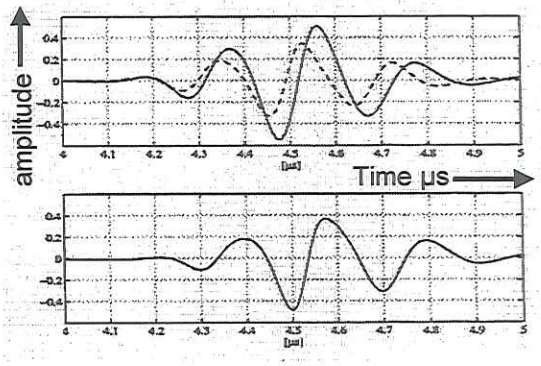

Figure 2: Echoes resulting from pulsing scheme of *Figure 1*. The top panel shows two consecutive echoes; the bottom panel their difference, the imaging signal.

METHOD

Figure 1 illustrates the method: a bubble is driven at its resonant frequency (say, 1 MHz), at a sufficiently low MI that it oscillates without disruption. This is the 'radial modulation' signal. At the peak

of its expansion phase it is insonated with a high frequency imaging pulse (say, 10 MHz). The echo, filtered to exclude the low frequency component, is shown in Figure 2 (top). The bubble is then insonated with a second pulse, this time when it is at the peak of its compression phase (Figure 1 bottom). In the simplest from of processing for this method, the two echoes produced are then subtracted, eliminating those from stationary, linear scatterers. It is noted that the amplitude of the subtracted echo from the bubbles (Figure 2 bottom) is comparable to that of each individual bubble echo, reflecting the fact that all components of the bubble echo contribute to the energy used to form the image. Whereas the bubble properties determine the optimum modulation frequency, the method will be effective for a wide range of imaging frequencies.

ACOUSTIC RESULTS

Doppler radial modulation imaging was implemented by means of a simple *in vitro* experiment. A fibre carrying SonoVue microbubbles was embedded in tissue equivalent gel and exposed to three-cycle ultrasound pulses at 0.7 MHz at an MI of less than 0.04. A modified commercial scanner (GE/Vingmed System 7) was triggered to issue a sequence of imaging pulses, each one alternately at peak positive and peak negative excursions of the modulation waveform. Conventional pulsed and colour Doppler processing was used to process the resulting sequence of echoes. Without the modulation signal, no echo was detected from the microbubbles. With the modulation signal turned on, a strong signal from the agent was detected at one half of the pulse repetition frequency. The signal intensity was independent of the system pulse repetition frequency. Colour and spectral Doppler images were obtained showing high signal-to-clutter ratios.

OPTICAL RESULTS

To evaluate the usefulness and sensitivity of radial modulation imaging in differentiating between gas bubbles and tissue, optical observations were carried out with the Brandaris-128 camera. The Brandaris-128 is a digital camera capable of acquiring in a single run 128 frames at a speed of 25 million-frames per second. To interrogate the bubbles at 2 different frequencies, two different transducers were used. The transducers had center frequencies of 0.5 MHz and 3.5 MHz. The transducers were mounted in a Plexiglas container and positioned such that their focal distances coincide at a depth of 75 mm. The acoustic pressures corresponded to mechanical indices of 0.2 at 0.5 MHz and less than 0.1 at 3.5 MHz. In this experiment, the optical observations were carried out at a frame rate of 14 millions frames per second and 128 successive frames were recorded. SonoVue contrast agent was used in the

experiments. We show in this study an example of a bubble of 4 μm diameter oscillating under the effects of both 0.5 and 3.5 MHz signals.

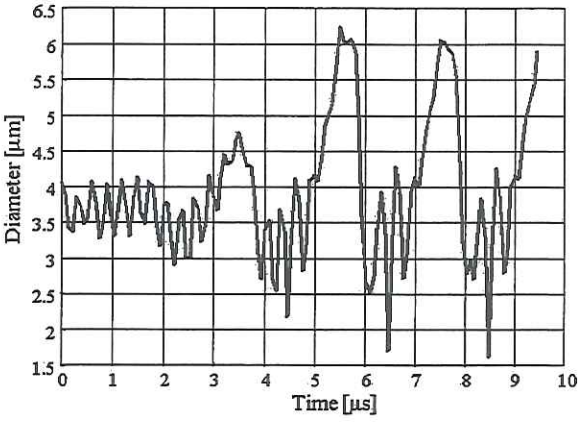

Figure 3:Diameter-time curve of a SonoVue microbubble insonified with a double frequency signal 0.5 MHz-3.5MHz.

Figure 3 shows the results obtained with the high-speed camera. It displays the diameter-time curve of a 4 μm SonoVue microbubble irradiated with the double frequency signal. We can see that the bubble diameter consists of a high frequency signal (3.5 MHz) modulated with a low frequency signal (0.5 MHz). The high frequency signal is mainly apparent during bubble compression while it is hardly seen in the compression phase.

We can observe that up to 3 μs, the 0.5 MHz signal amplitude is low and thus the bubble response at 3.5 MHz is almost constant between compression and expansion phases. After 3 μs, the amplitude of the 0.5 MHz signal increases making the bubble oscillations more evident. The bubble diameter compresses to about 3 μm and expands up to 6 μm. During these oscillations, the 3.5 MHz imaging signal interrogates thus the same bubble but that has a variable size. In this case we clearly appreciate that the response at 3.5 MHz shows clear differences between compression and expansion phases. During compression (smaller bubble), the bubble's response at 3.5 MHz is much larger than its response during expansion phase. During expansion phase, the bubble becomes larger and thus far away from the resonance size, reducing by that its total response. The decorrelation between the compression and expansion phases of the LF signal in the 3.5 MHz bubble response is significantly high to be used as a parameter to detect gas bubbles and discriminate between oscillating structures (contrast bubbles) and non-oscillating structures (tissues).

DISCUSSION

Both the acoustical and optical results suggest that radial modulation imaging might be a feasible imaging and Doppler method for bubble detection at higher frequencies than that of the bubble resonance. Both physical issues and technical challenges need to be tackled for the method to proceed. The optical results suggest, in contrast to theoretical prediction, that the bubbles are refractory to excitation at the high frequency while at their peak expansion phase. The reason for this observation is unclear. Technically, a method of simultaneous transmission of the two required signals needs to be contrived, preferably without the need to create new, specialised array transducers.

OPTISON ENHANCES GENE DELIVERY BY INCREASING THE UPTAKE OF PLASMID DNA BY CELLS

Stefanos Theoharis PhD, Florentia Fostira*, Andrew George PhD+, Martin Blomley MD**

*Imperial College London, *Imaging Sciences Department, +Immunology Department, Hammersmith Campus, Ducane Rd, London W12 0NN*

Introduction: Ultrasound (US)-mediated gene delivery is relatively novel field of increasing popularity. Its efficiency can be greatly enhanced by the use of microbubble US contrast agents. Several of these have been tested and among the commercially available ones, Optison appears to yield the highest transfection efficiency (Li et al., 2003) (Blomley, 2003). Several studies have been performed demonstrating this ability in a variety of settings. Here, we used quantitative (flow cytometry) and qualitative (confocal microscopy) methods, in order to assess the uptake of fluorescently labelled DNA by cells after sonication.

Methods: Gene delivery was optimised on CHO cells in 24-well plates. It was found that 5μg/ml of DNA was optimal along with 5% (v/v) Optison. The cells were insonated as monolayers by holding the plate above an underwater probe in a waterbath. Our experiments showed that 1Mhz, 1W/cm2 US at 20% duty cycle was optimal, with 10 seconds exposure time. Efficiency was analysed in terms of efficiency by β-Gal assay, microscopy after X-Gal staining and toxicity. Plasmid DNA was labelled with 3 molecules of YOYO dye per plasmid and used as in gene transfection experiments in the presence and absence of Optison. Internalisation was assessed by flow cytometry. The cells were visualised by confocal microscopy. It was compared to two commercially available non-viral vectors, Superfect (Qiagen) and Lipofectamine 2000 (Invitrogen).

Results: It was shown that Optison produced a transfection efficiency of 15%, similar to that of Superfect. Lipofectamine 2000 was best with 40%. US without Optison yields efficiencies of 2%. Optison can enhance the internalisation of plasmid DNA by 3-, 6- and 25-fold over no Optison after incubation with the cells over 10 minutes, 3 hours and 24 hours respectably. The internalisation is comparable to that achieved by Superfect at 24 hours. At earlier time-points it is significantly less. Confocal microscopy shows that the DNA is indeed interacellular.

Discussion: It is clear that Optison exerts the observed increases in transfection efficiency by enhancing the uptake of DNA by cells. The specific localisation of DNA within the cells is not clear, what is clear, however, is that it is internal. We tested the ability of the labelled plasmid to be expressed upon internalisation and found that it is not altered by the labelling. It will be important to delineate the mechanism of Optison-mediated gene delivery and design similar US contrast agents with enhanced effects.

Blomley, M. (2003). Which US microbubble contrast agent is best for gene therapy? Radiology *229*, 297-298.

Li, T., Tachibana, K., and Kuroki, M. (2003). Gene transfer with echo-enhanced contrast agents: comparison between Albunex, Optison, and Levovist in mice--initial results. Radiology *229*, 423-428. Epub 2003 Sep 2025.

SPAQ (SENSITIVE PARTICLE ACOUSTIC QUANTIFICATION): A NEW ULTRASOUND-BASED APPROACH FOR IN VIVO QUANTITATIVE MOLECULAR IMAGING

P. Hauff[1], M. Reinhardt[1], M. Mäurer[2], R. Linker[2], A. Briel[1], M. Schirner[1]

[1]*Research Laboratories, Schering AG, Berlin, Germany*
[2]*Clinical Research Group for Multiple Sclerosis, Department of Neurology, Julius Maximilians-Universität Würzburg, Germany*

Molecular imaging requires the identification and spatial localization of a specific marker and its quantitative analysis. Based on the stimulated acoustic emission (SAE) of single air-filled microparticles (MPs) we established sensitive particle acoustical quantification (SPAQ) which is an ultrasound-derived imaging method with spatial resolution in the lower micrometer range. SPAQ enables the quantification of acoustical signals of static MPs with high accuracy.
Specific MPs were created by using streptavidine loaded MPs and a respective biotinylated antibody. We first checked the feasibility of our system in an agar-phantom, followed by ex vivo and in vivo experiments.

In a first set of experiments, we quantified MPs in an agar phantom containing 30000 MPs/mL with SPAQ-resolutions between 10-100µm. We could show that acoustic counts [AC] correspond to the concentration and number of MPs used in the phantom and we demonstrated a linear relationship between SPAQ-resolution (thickness of SAE-imaging slices) and acoustic counts ($r = 0{,}9918$). These findings were corroborated by ex vivo experiments in rat livers, which had received two different doses ($1x10^7$ vs. $1x10^8$ MPs per kg body weight intravenously) 30 min. before sacrifice.

To test the biological and medical potentiality of SPAQ, we performed quantitative molecular imaging in rat experimental autoimmune encephalomyelitis (EAE) which is an established inflammatory disease model of human multiple sclerosis (MS). We targeted the MPs to intercellular adhesion molecule 1 (ICAM-1) expressed on lesion-associated blood vessels. We were able to image and to quantify ICAM-1 targeted MPs *in vivo* with high sensitivity, specificity and resolution at the blood brain barrier during acute EAE in anesthetized rats. Furthermore, after

treatment with methylprednisolone, the measured number of targeted anti-ICAM-1-MPs was significantly less ($P < 0.008$) compared to controls.

The acoustic counts correlated closely with both, the clinical signs of the diseased rats and the inflammatory lesions as revealed by microscopic histopathology of brain tissue sections which validates our technique.

The results demonstrate that SPAQ of antibody-MP conjugates enables depiction of molecular events at the blood-brain barrier (BBB) and provides monitoring of treatment effects at the molecular level with high sensitivity and specificity in vivo.

ULTRASOUND GENE DELIVERY TO SAPHENOUS VEIN GRAFTS

E. Akowuah, T. Bettinger[1], A. Brisken, C. Gray, C. Su, A. Lawrie, S. Francis, J. Gunn, D. Crossman, C. Newman

Cardiovascular Research Unit, University of Sheffield, Sheffield, UK, [1]Bracco Research, Geneva. AFB is an independent consultant in ultrasonics

Background - Saphenous vein graft (SVG) failure remains a major clinical problem and is an important target for gene therapy. *Ex vivo* adenoviral gene transfer of tissue inhibitor of metalloproteinase 3 (TIMP-3) reduces neointima formation in experimental SVG, but concerns remain over the use of viral vectors in patients. Ultrasound exposure (USE) in the presence of echocontrast microbubbles (ECM) substantially enhances non-viral gene delivery. We investigated the effects of ultrasound-enhanced gene delivery (UEGD) of TIMP-3 plasmid on vascular remodelling in porcine SVG.

Methods and Results – Maximal luciferase activity (3000-fold *vs* naked plasmid alone) and TIMP-3 transgene expression in porcine vascular smooth muscle cells (VSMC) *in vitro* was achieved using USE at 1MHz, 1.8 mechanical index (MI), 6% duty cycle (DC) in the presence of 50% (v/v) BR14 ECM (Bracco). Yorkshire White pigs received carotid interposition SVG that were untransfected or had undergone *ex vivo* UEGD of lacZ (control) or TIMP-3 plasmids using these optimised USE parameters. 28d post-grafting, lumen and total vessel area were significantly greater in the TIMP-3 group (10.1±1.2 and 25.5±2.2 mm^2, respectively) compared to untransfected (6.34±0.5 and 20.8±1.9 mm^2) or lacZ transfected (6.1±0.7 and 19.7±1.2 mm^2) controls ($p<0.01$).

Conclusions - Non-viral TIMP-3 plasmid delivery by USE achieves therapeutic gain in a clinically relevant model of SVG failure, and is the first study to show the therapeutic potential of UEGD in this condition. Further developments to improve UEGD to SVG are warranted.

FOCAL LIVER LESIONS: WHAT WE KNOW, WHAT WE DON'T KNOW, WHAT WE WANT FOR THE FUTURE

Thomas Albrecht

Klinik und Poliklinik für Radiologie und Nuklearmedizin
Campus Benjamin Franklin Charité - Universitätsmedizin Berlin
Freie Universität Berlin und Humboldt-Universität zu Berlin Hindenburgdamm Germany

The most important application of ultrasound contrast agents (USCA) in Radiology is imaging of focal liver lesions. The recent technological improvements of non-linear imaging modes and the advent of low solubility gas agents such as SonoVue (Bracco SPA, Milan) have lead to significant progress in this field in the last few years.

A number of recent studies on several hundred patients have demonstrated that contrast enhanced ultrasound (CEUS) of the liver is a clinical useful tool and it has become clinical routine clinical practice in many European centres. It performs extremely well in characterising focal liver lesions. The rate of correctly diagnosed lesions is in the order of 85 - 90% and differentiation between benign and malignant is possible in approximately 95% of cases. CEUS is thus superior to CT and about as good as MRI in this application. Detection of metastases is also substantially improved by the use of microbubbles when compared to unenhanced US. The sensitivity of CEUS in the detection of hepatic metastases is approximately 80% and thus very similar to that of contrast enhnanced single slice spiral CT. However, with sensititvities of approximately 90%, state-of.the-art 16 detector row multislice CT and especially SPIO-enhanced MRI are more sensitive.

The recently published EFSUMB guidelines on the use of contrast agents for liver ultrasound (1) reflect the progress made in recent years by recommending the use of USCA both for lesion characterisation and detection of focal liver lesions. According to the guidelines, every cancer patient undergoing liver US as part of the staging process should have a contrast enhanced examination.

Liver specific agents have some important advantages over non-specific agents such as SonoVue, especially with regards to detection of HCC and metastases. Levovist (Schering AG, Berlin) is the only liver-specific agent currently available. Due to its poor stability and the necessity to use high MI it is no longer used on a large scale.

The ideal contrast agent for liver imaging would be a liver-specific perfluor agent, which combines the advantages of liver-specificity with the ability to perform low MI real time imaging. Two such agnts have entered clinical development (Sonazoid, Amersham Medical and BR14, Bracco). Our limited experience with these agents has been very encouraging. These agents would likely make the biggest difference in detection of HCC, which is currently a substantial limitation of CEUS and a clinical problem of ever increasing importance. Unfortunately, both these agents are currently not being developed ion Eurpope or North America, clinical studies with Sonazoid continue in Japan.

Another established and widely used application of USCA is the work-up vesico-ureteric reflux in children. The adoption of this highly accurate technique has greatly reduced the number of X-ray MCU-examination in these young children.

An interesting experimental application of contrast agents in the liver is transit time analysis. It is currently used as a research tool and has provided some encouraging results with regards to detecting the on-set of liver cirrhosis in patients with chronic hepatitis and to detecting "occult" metastases. This could become an important clinical tool for much earlier detection of metastases, potentially at a microscopic level, in the future.

Abdominal applications used in clinical practise in a relatively small number of patients include blunt abdominal trauma (especially splenic but also hepatic and renal), focal splenic lesions, focal renal lesions and pancreatic masses. This may be very useful in selected cases, large studies on the clinical benefit of these applications are however so far not available. It is for the future to decide if and which non-hepatic abdominal applications of USCA will prevail.

1. EFSUMB Study Group. Guideline for the use of contrast agents in ultrasound. Ultraschall in Med 2004, 25:249-256

ULTRASOUND PARAMETRIC PERFUSION IMAGING PREDICTS THE AREA OF INFARCTION IN ACUTE ISCHEMIC STROKE

Günter Seidel, MD [1]; Hakan Cangür MD [1]; Karsten Meyer-Wiethe, MD [1]; Gilles Renault [2]; Alain Herment [2]; Angela Schindler [1]; Christian Kier [3]; Til Aach [3]

[1] Department of Neurology, University Hospital Schleswig-Holstein, Campus Lübeck, Germany; [2] U.494 INSERM, CHU Pitié, Paris, France; [3] Institute for Signal Processing, University of Lübeck, Germany

Background and Purpose. Cerebral perfusion deficits in acute ischemic stroke can be detected by means of transcranial harmonic imaging after ultrasound contrast agent bolus injection. We evaluated five different parameters of the bolus kinetics as parametric images and correlated areas of disturbed perfusion with the area of definite infarction.

Methods. 22 patients suffering from acute internal carotid artery infarction were investigated with perfusion harmonic imaging after SonoVue® bolus injection (BHI). For each subject, we calculated five different images based on the following parameters from the time-intensity curve in each pixel: pixelwise peak intensity (PPI), area under the curve (AUC), positive gradient (PG), time to peak (TTP) and a three factor image from the factor analysis of medical image sequences (FAMIS). The findings in the diencephalic imaging plane were compared with the definite area of infarction as diagnosed by cranial computed tomography (CCT).

Results. We found the following sensitivities and positive predictive values (PPV) for parametric images to predict the definite area of infarction in follow-up CCT: PPI (100% / 95%), AUC (100% / 90%), FAMIS (89% / 89%), PG (84% / 94%) and TTP (47% / 100%). The areas of disturbed perfusion in all five types of parametric images correlated significantly with the area of infarction in CCT. Images from the FAMIS algorithm and PPI images showed the highest Spearman rank correlation with the area of definite infarction as displayed in CCT (both $r = 0.76$, $P < .001$). Images from the other parameters correlated as follows: PG: $r = 0.62$ ($P = .003$), AUC: $r = 0.53$ ($P = .014$), TTP: $r = 0.50$ ($P = .021$).

Conclusions. BHI can detect disturbed perfusion in acute hemispheric stroke. Intensity-based parameters and FAMIS have a high sensitivity, the TTP a high PPV and specificity, respectively to predict the development of infarction.

Acknowledgments: This study was supported by a grant from the European Union (UMEDS - QLG1-CT-2002-01518).

Thursday, January 20, 2005

Social Event

Historical Radar Steamship "De Majesteit"
Maasboulevard, Rotterdam

Boarding: 18.30
Buffet Indonesia: 19.30
Dessert: 21.30
Back at the Maasboulevard: 23.00

Coaches will be leaving from the Hilton at 18:00 and will be back there around 23:30

The 10th ESUCI is sponsored by:

GE Medical Systems
Mr. Al Lojewski
4855 W. Electric Avenue
WI 53219-1628 Milwaukee
USA

BRACCO International BV
Dr. Stefano Nervetti
Centro Galleria 3 - Via Cantonale
CH-6928 Manno
Switzerland

SIEMENS Medical Solutions
Mr. Richard Kirby
Ultrasound Division
European Business Centre
126-135 Staines Road
HONSLOW, Middlesex TW3 3JF - UK

PHILIPS Internationaal BV
Mr. F. Schuling
P.O. Box 10.000
5680 DA BEST
The Netherlands

Bristol-Myers Squibb Pharmaceuticals
Dr Michael Thompson, International
Medical Director - Medical Imaging &
Dr John Beets, European Marketing
Director - Medical Imaging
141-149 Staines Road
Hounslow Middlesex TW3 3JA-UK

POINT Biomedical Corp.
Mrs. M. Kayan
887 L Industrial Road
SAN CARLOS, CA 94070
USA

TOSHIBA Medical Systems
Mrs. G. Mulders
Zilverstraat 1
2718 RP ZOETERMEER
The Netherlands

OLDELFT B.V.
Ing. R. 't Hoen
Postbus 5082
2600 GB DELFT
The Netherlands

ICIN
Mrs. M. Helmers-Kersten
P.O. Box 19258
3501 DG UTRECHT
The Netherlands

SUGB
Prof.dr.ir. A.F.W. van der Steen
Thorax - Biomedical Engineering
ErasmusMC
P.O. Box 1738
3000 DR ROTTERDAM
The Netherlands

FIRST ANNOUNCEMENT 2006

11th EUROPEAN SYMPOSIUM ON ULTRASOUND CONTRAST IMAGING 26-27 JANUARY 2006, ROTTERDAM, THE NETHERLANDS

Course Directors: Folkert ten Cate
Nico de Jong
David Cosgrove (Hammersmith – London)

Information on the
11th EUROPEAN SYMPOSIUM ON
ULTRASOUND CONTRAST IMAGING:
Mrs. Mieke Pruijsten
m.pruijsten@erasmusmc.nl

Erasmus MC
Universitair Medisch Centrum Rotterdam

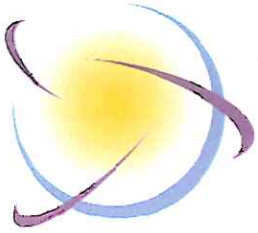

Bristol-Myers Squibb
Medical Imaging

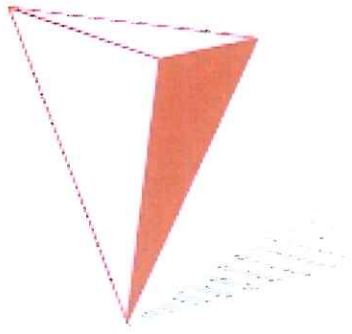

POINT BIOMEDICAL

TOSHIBA

Oldelft
Ultrasound

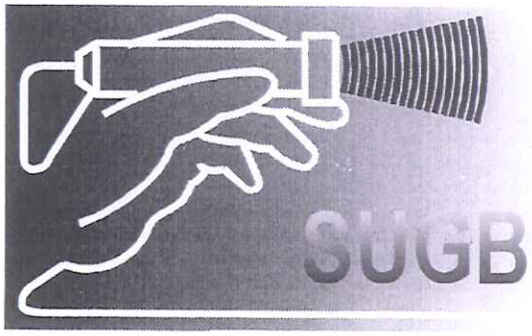

GE Healthcare

PHILIPS

THE IMAGE OF INNOVATION

SIEMENS

medical